

ZnO NANOTIP-BASED ACOUSTIC WAVE SENSORS

by

ZHENG ZHANG

A Dissertation submitted to the

Graduate School-New Brunswick

Rutgers, The State University of New Jersey

in partial fulfillment of the requirements

for the degree of

Doctor of Philosophy

Graduate Program in Electrical and Computer Engineering

written under the direction of

Professor Yicheng Lu

and approved by

New Brunswick, New Jersey

January, 2008

ABSTRACT OF THE DISSERTATION

ZnO Nanotip-based Acoustic Wave Sensors

by ZHENG ZHANG

Dissertation Director:

Dr. Yicheng Lu

ZnO nanostructures possess unique advantages for the biosensor applications, such as giant surface areas, high sensitivity, biological compatibility, and integratability with Si-based electronics.

This dissertation addresses the development of ZnO nanotip-based acoustic wave sensors, and their biological applications. ZnO nanostructures are grown on the surfaces of various sensors, including surface acoustic wave (SAW) sensors and quartz crystal microbalance (QCM) sensors, by metalorganic chemical vapor deposition (MOCVD). The single crystalline ZnO nanotips are well aligned along the substrate normal direction, confirmed by scanning electron microscope (SEM) and X-ray diffraction (XRD) measurements, respectively. The photoluminescence (PL) measurements show the free exciton emission at room temperature, indicating superior optical property of the ZnO nanotips.

The surface wetting properties of the ZnO nanostructured sensing surfaces are studied. It is demonstrated that the contact angles on ZnO nanotips can be changed between 0 and 130 degrees. The repeatable and reversible transitions between hydrophobic and superhydrophilic status of ZnO nanostructured surfaces have been achieved by UV illumination and low temperature oxygen annealing. The transition rate has been increased by 10-times in comparison with the published results. The immobilizations of DNA oligonucleotides to ZnO nanostructures have been conducted. DNA hybridization with complementary and non-complementary second strand DNA oligonucleotide is used to study the selectivity of the SAW sensor. The radioactive labeling tests and SAW sensor responses demonstrate that by using ZnO nanotips the DNA immobilization is enhanced by a factor of 200 in comparison with using the ZnO films. A ZnO nanotip-based QCM sensor is developed. The ZnO nanotip coated QCM sensor shows a 10-times larger frequency shift than that of regular QCM sensors, when measuring the same DNA oligonucleotide solution. In addition, the superhydrophilic behaviors of the nanotip array significantly reduce the required liquid volume for effective detection and only 3% solution is required to cover the same sensing surface compared to the traditional QCM sensor. The superhydrophilic sensing surface boosts the solution taking ability; therefore, enhances the sensitivity of the QCM sensor. The functionalization of ZnO nanotips with a series of mono- or bi-functional linkers have been achieved, which makes the selective biological sensing possible on the ZnO nanotip based QCM. ZnO nanotip-based SAW and QCM sensors possess the advantages of both traditional acoustic wave sensors and ZnO nanostructures, including high efficiency, good selectivity, low cost and broad biological applications.

DEDICATION

To my parents

Hao Zhang and Hong Song,
my husband Fan and my son Franklin

ACKNOWLEDGEMENTS

I would like to express my sincere gratitude to my dissertation advisor, Professor Yicheng Lu. With patient critique and insightful encouragement, Prof. Lu guided me through the hardest time of my research life. His words and action set a role model for me, from which I learned essential characters of a successful scientist, such as integrity, vision and paying attention to details. I am a better person because of him.

I would like to thank my dissertation committee members, Prof. Kuang Sheng, Prof. Wei Jiang, and Prof. Elena Galoppini for the time and effort they have spent to review this work.

I would like to thank my fellow co-workers in Prof. Lu's research group, who have provided technical assistances throughout my work. In particular, I would like to thank Mr. Hanghong Chen, Dr. Yimin Chen, Dr. Sriram Muthukumar, Mr. Gauraf Saraf, Dr. Jian Zhong, Dr. Nuri. W. Emanetoglu, Dr. Pan Wu, Ms. Ying Chen, Mr. Pavel Reyes, Mr. Ziqing Duan and Mr. Jun Zhu for their assistances in material growth and characterization, device processing and test.

Ms. Olena Taratula, Mr. Andreas Johannes Nuber, Prof. Theodore Madey, Dr. Sandrine Rivillon, Prof. Yves Chabal, Ms. Jingqiu Chen, Prof. O. Mirochnitchenko and Prof M. Inouye all deserve my special thanks for their collaboration and insightful discussion in support of this work.

I would like to thank my family for their endless support and love to me. I could not have achieved a single thing without them standing behind me, no matter how far they are away from me. Finally, I would like to thank my husband, Fan, who has lived this dissertation every day with me and provided the love and support required seeing it to its completion.

This work has been supported by NSF through the grant CCR-0103096 and ECS-0088549, Rutgers AEF and TCF.

TABLE OF CONTENTS

Abstract	ii
Dedication	iv
Acknowledgement	v
Table of Contents	vi
List of Tables	ix
List of Figures	x
Chapter 1. Introduction	1-3
1.1. Motivation	1
1.2. Scope of Work	3
1.3. Organization of the Dissertation	3
Chapter 2. Technical Background	4-41
2.1. Classification of Sensors	4
2.2. Chemical and Biological Sensors	6
2.3. Acoustic Wave Sensors	23
2.3.1. Introduction	23
2.3.2. Piezoelectricity	24
2.3.3. Bulk Acoustic Wave Devices	28
2.3.4. Surface Acoustic Wave Devices	30
2.4. ZnO Material for Biosensors	37
2.4.1. ZnO Acoustic Wave Sensors	37
2.4.2. ZnO Nanostructures	37
2.4.3. ZnO Electrochemical Sensors and Optical Sensors	39

2.5. Summary	41
Chapter 3. Properties of ZnO Nanotips Grown on Various Substrates	42-59
3.1. MOCVD Growth	42
3.2. Characterizations of ZnO Nanotips and Films	44
3.2.1. Structural Characterizations	44
3.2.2. Optical Characterizations	48
3.3. Growth Integration of ZnO Nanotips with SAW and QCM	50
Sensors	
3.5. Summary	58
Chapter 4. Surface Properties of ZnO Nanostructures	60-90
4.1. Wettability	60
4.2. Wettability Control on ZnO Nanostructures	63
4.3. Feasibility Study of Surface Functionalization on ZnO	76
Nanostructures	
4.4. Summary	90
Chapter 5. ZnO Nanotip-based SAW Sensors	91-111
5.1. Device Design and Fabrication	92
5.2. DNA Immobilization and Hybridization	98
5.3. Sensors Testing	103
5.4. Summary	111
Chapter 6. ZnO Nanotip-based QCM Sensors	112-143
6.1. Device Analysis	112
6.2. Selective DNA Immobilization	129

6.3. Sensor Testing	134
6.4. Summary	140
Chapter 7. Conclusion and Future Work	144-149
7.1. Conclusion	144
7.2. Suggestions for Future Work	147
References	150-157
Curriculum Vitae	158

LIST OF TABLES

2.1	Measurands of Sensors	5
2.2	Physical Parameters of More Commonly Used Piezoelectric Materials	26
2.3	Applications Summary of Three Major Piezo-films: ZnO, AlN and PZT	26
2.4	Comparison of Acoustic Sensors	32
4.1	Compounds Bound (b), Physisorbed (p), or Nonbound (nb) to ZnO	81
5.1	Design Parameters of the SAW Sensors	95
6.1	Liquid Consumption on the 0.2047 cm² Sensing Area of QCM Sensors with Different Wetting Properties	135
6.2	Frequency Shift of Different Harmonics between the Tradition, Hydrophobic and Hydrophilic ZnO QCM Sensors	138

LIST OF FIGURES

2.1	The schematic of human olfactory system	7
2.2	ZnO semiconducting gas sensor	12
2.3	ZnO conductive gas sensor for different gas sensing	14
2.4	Four types of optical imaging for biosensing	22
3.1	A diagram of the MOCVD system used for ZnO film and nanostructure growth.	44
3.2	The θ -2 θ scan of x-ray diffraction pattern of MOCVD grown ZnO nanotips on (a) SiO ₂ /Quartz substrate, and (b) glass substrate	45
3.3	The field enhanced SEM image of the MOCVD grown ZnO nanotips on (a) SiO ₂ /Quartz substrate, and (b) glass substrate	46
3.4	A field enhanced SEM image of ZnO film on r-sapphire	47
3.5	The θ -2 θ scan X-ray diffraction grown ZnO film on r-sapphire	47
3.6	The transmission of ZnO film on r-sapphire	48
3.7	Photoluminescence spectrum of ZnO nanotips on glass; the inset shows transmission of ZnO nanotips on glass	49
3.8	FESEM images of (a) ZnO nanotips, and (b) ZnO film grown on SiO ₂ /LiNbO ₃ . The well-aligned nanotips have an average diameter of 75nm and height of 500nm.	54
3.9	X-ray coupled θ -2 θ scans of (a) LiNbO ₃ substrate; (b) ZnO nanotips on SiO ₂ /LiNbO ₃ substrate; (c) low angle X-ray scan of the ZnO nanotips, where only the (002) ZnO peak is observed, confirming the preferred c-axis orientation of the ZnO nanotips.	55, 56

3.10	Room temperature PL spectrum of ZnO nanotips grown on a SiO ₂ /LiNbO ₃ substrate. A strong near bandedge peak at 3.29 eV is observed, confirming good optical property of the ZnO nanotips.	59
3.11	(a) SEM of ZnO nanotips on gold; (b) Selected area electron diffraction pattern from a single ZnO nanotip	59
4.1	Schematic of a droplet on a homogeneous, flat surface. The arrows indicate the forces caused by the surface tensions σ_{ij} along the interfaces. The indices stand for the different interfaces solid-vapor (sv), solid-liquid (sl) and liquid-vapor (lv). θ is the contact angle between the surface of the solid and the liquid.	61
4.2	The actual and projected (geometric) area of a rough surface	62
4.3	View through the telescope of a contact angle goniometer. The drop is aligned with the baseline and the intersection point of the movable scale and the baseline. For CA measurement, the movable scale is rotated until it matches the tangent to the drop and thus indicates the CA on the fixed scale.	65
4.4	Setup for computer-aided CA measurements. The sample with the drop on it is highlighted by a back-light to provide a good image quality and contrast. The CCD-camera captures a picture from the side view and sends it to the connected PC with installed CA measurement software which processes the image and determines the contact angle. (Model 500 Advanced Goniometer from ramé-hart instrument co.)	65
4.5	Surface morphologies of ZnO a) nanotips on c-sapphire, b) nanotips on	67

	Si, and c) film on r-sapphire, taken by field-emission scanning electron microscope (SEM)	
4.6	(a) Theta-2theta x-ray scans for ZnO nanotips grown on c-sapphire, Si and glass substrates. (b) A comparative on-axis ω -rocking curve of ZnO nanotips grown on c-sapphire, Si and glass substrates.	68
4.7	(a) Hydrophobic surface of ZnO film with contact angle (CA) $\sim 95^\circ$. (b) Hydrophilic surface of ZnO film with CA $\sim 37^\circ$. (c) Hydrophobic surface of ZnO nanotips with CA $\sim 130^\circ$. (d) Super hydrophilic surface of ZnO nanotips with CA $\sim 0^\circ$.	69
4.8	CAs at corresponding sample treatment steps in the growth \rightarrow low CA \rightarrow dark storage \rightarrow high CA \rightarrow UV irradiation \rightarrow low CA \rightarrow dark storage \rightarrow high CA...	72
4.9	(a) Contact angle change under UV light as a function of time. The substrates are ZnO nanotips and film, respectively. b) Contact angle change under O ₂ annealing at 50 °C as functions of time. The substrates are ZnO nanotips and film, respectively	77
4.10	Compounds employed in the binding study. The compounds that did bind to the ZnO nanotips are shown in red.	78
4.11	The schematic of the functionalization of ZnO nanotip using bifunctional linker.	78
4.12	The three main binding modes between a COOH group and a metal oxide surface.	80
4.13	ATR spectrum of isophthalic acid 1 free (top, red line) and bound to ZnO	83

	nanotips (bottom, black line).	
4.14	ATR spectra of free heptanoic acid 6 (top, red line) and 6 bound to ZnO nanotips (bottom, black line).	83
4.15	(a) IR spectrum of 3-mercaptopropionic acid (8). (b) ATR spectrum of 11 bound to ZnO-N showing the carbonyl region.	85
4.16	ATR spectrum of 8 bound to MgZnO nanotip. This spectrum is identical that of 8/ZnO nanotip shown in Figure 4.15(b).	89
5.1	Schematic of the ZnO nanotip-based SAW biosensor structures: (a) cross-section, (b) top view	94
5.2	Schematic of the ZnO nanotip-based SAW biosensor structures with design parameters as shown in Table 5.1	95
5.3	The simulated results of transmission spectra for the SAW delay line based on the Design parameters shown in Table 5.1, fabricated on (a) 128° Y-cut LiNbO ₃ and (b) ST cut Quartz.	96
5.4	Schematic representation of the DNA immobilization process. (a) Before immobilization; (b) After immobilization	99
5.5	Immobilization of DNA oligonucleotide on different surfaces. (1) LiNbO ₃ ; (2) ZnO flat film; (3) ZnO nanotip array. The oligonucleotide immobilization on the ZnO nanotip arrays is approximately 200 times larger than the flat ZnO film surface and approximately 600 times larger than the LiNbO ₃ substrate	100
5.6	Schematic representation of the DNA hybridization process: (a) Applying Avidin (protein immobilization); (b) Applying Biotin-DNA primary	102

strand; (c) Applying DNA complementary secondary strand (or non-complementary secondary strand APE, the control solution); (d) After DNA hybridization.

5.7	The N-SAW Characterization test setup	103
5.8	S_{21} (transmission) spectra for the SAW sensors fabricated on bare LiNbO_3 , LiNbO_3 with SiO_2 layer, and LiNbO_3 with ZnO nanotip array on SiO_2 layer.	105
5.9	S_{21} (transmission) spectra for the ZnO nanotip SAW sensor, before and after DNA oligonucleotide immobilization. The phase shift at the center frequency of 327.94 MHz is 191°	108
5.10	Measured S_{21} (transmission) spectra for the reference and sensor devices for 100ng protein detection	109
5.11	Phase difference between the reference and sensor devices due to 100 ng protein detection.	110
6.1	Equivalent circuit of a quartz crystal microbalance	115
6.2	Admittance magnitude of a 10MHz gold QCM measured by network analyzer	119
6.3	Admittance phase angle of a 10MHz gold QCM measured by network analyzer	120
6.4	Susceptance and conductance of a 10MHz gold QCM measured by network analyzer.	121
6.5	B-G curve for a 10MHz gold QCM measured by network analyzer.	122
6.6	Equivalent circuit of a mass loaded QCM	122

6.7	The schematic structure of a ZnO nanotips-based QCM	123
6.8	Comparison of the admittance magnitude of a 10MHz gold QCM and ZnO N-QCM measured by network analyzer	125
6.9	Comparison of admittance phase angles of a 10MHz gold QCM and ZnO N-QCM measured by network analyzer	126
6.10	Susceptance and conductance of a 10MHz ZnO nanotip-based quartz crystal microbalance measured by network analyzer	127
6.11	B-G curve for a 10MHz ZnO nanotip-based quartz crystal microbalance measured by network analyzer	128
6.12	Schematic presentation of the ZnO nanotips surface modification: (A) MHDA modified surface (the formation of sulfhydryl surface); (B) an activated sulfhydryl surface with pyridyl groups; (C) an exchange reaction between disulfide surface and sulfhydryl modified DNA (SH-ssDNA)	130
6.13	Schematic presentation of the ZnO nanotips surface modification. (A) Formation of N-CPDS-surface; (B) reaction of amino-modified DNA with NHS-ester.	133
6.14	The N-QCM device characterization test setup	134
6.15	Forward transmission parameter (S_{21}) of the ZnO nanotip-based QCM devices compared to traditional QCM device at the 1 st , 3 rd , 5 th , 7 th harmonics	136
6.16	Forward transmission parameter (S_{21}) of the superhydrophilic ZnO nanotip-based QCM devices in 3-step functionalization	141

6.17	Forward transmission parameter (S_{21}) of the hydrophobic ZnO nanotip-based QCM devices in 3-step functionalization	142
6.18	Forward transmission parameter (S_{21}) of the ZnO nanotip-based QCM devices in 2-step functionalization at 1 st harmonic	143

Chapter I. Introduction

1.1 Motivation

The field of biochemical and biological sensors is one of the fastest growing areas in both research and commercial fields. The \$3 billions biosensor market has an annual growing rate of 10% per year. Most of the research work in this field is directed towards reducing the sensor size and quantitative identifying of multiple species. Also, quick response, minimum hardware requirement, good reversibility, sensitivity, and selectivity are qualities expected of an excellent sensor.

The applications of biochemical sensors include drug development, clinical diagnosis, agricultural, horticultural and veterinary analysis, pollution and contamination analysis, fermentation control and analysis, analysis of flavors and pheromones, quality and process control, industrial gases and liquids, explosives detection and biochemical defense for military.

Meanwhile, recent developments in nanoscale science and engineering show novel, promising nanostructured biosensors with faster response, higher sensitivity, and higher selectivity than the conventional planar sensor configurations, since the nanostructured sensors have small dimensions combined with dramatically increased contact surface and strong binding with biological and chemical reagents. Integrating the nanosensors with the nanofluidics technology makes nanoscale lab-on-chip a hot research topic. The need of simultaneously identifying multi-analytes has led to the development of array-based sensors. The design of cross-reactive array generates a pattern upon exposure to an analyte mixture.

On the other hand, there is an emerging interest in the use of wide bandgap semiconductors as gas and chemical sensors [1-5]. For example, ZnO is a piezoelectric, transparent wide bandgap semiconductor that can be used in surface acoustic wave devices. ZnO has been effectively used as a gas sensing material based on the near-surface modification of charge distribution with certain surface-absorbed species [6]. In addition, alloying ZnO with MgO forms the ternary compound $\text{Mg}_x\text{Zn}_{1-x}\text{O}$, which extends ZnO bandgap. Zn and Mg are both essential elements for neurotransmitter production and enzyme functioning, making MgZnO more attractive for biosensor applications[7, 8]. ZnO nanostructures made by MOCVD are grown at relatively low temperatures (300~500 °C), giving ZnO a unique advantage over other wide bandgap semiconductors, such as GaN and SiC nanowires. Through proper doping, ZnO can be made semiconductive, highly conductive, transparent, piezoelectric, and ferromagnetic. With such properties, ZnO has many applications including optoelectronic devices, acoustic devices, spintronics, MEMS and NEMS, and sensors and by integrating its versatile properties. ZnO nanostructures show their unique advantages as the novel sensing surfaces, such as giant sensing areas, high sensitivity, biological compatibility and integratability.

This work is concerned with the integration of ZnO nanostructures with the surface acoustic wave (SAW) and bulk acoustic wave (BAW) sensor technology, which can be widely used for gas and liquid sensing in many biological and biochemical applications. The goal is to develop low-cost, highly sensitive ZnO nanotip-based biosensor with novel nanostructures.

1.2 Scope of Work

The objective of this research is to design, fabricate and characterize the prototypes of ZnO nanotip-based SAW and QCM sensors for biochemical applications.

The scope of this study covers:

- (1) Characterization of ZnO nanotips grown on piezoelectric substrate using x-ray diffraction (XRD), scanning electron microscopy (SEM) and photoluminescence (PL) spectrum.
- (2) Feasibility study of the surface properties and modifications of ZnO nanotips for sensing.
- (3) Design, fabrication and demonstration of ZnO nanotip-based SAW biosensor and QCM biosensor.

1.3 Organization of the Dissertation

After a brief introduction in Chapter 1, the technique background of sensor technology, SAW sensor and QCM sensor, ZnO nanostructures and biosensors are reviewed in Chapter 2. Chapter 3 concentrates on ZnO nanotip material growth and characterization. The surface properties, especially the wettability control of ZnO nanostructures, are discussed in Chapter 4. Chapter 5 and 6 are concerned with the design and fabrication of the ZnO nanotip-based SAW sensor and QCM sensor, as well as the surface functionalization, DNA immobilizations and sensor testing of ZnO nanotip-based SAW and QCM sensors. Finally, Chapter 7 summarizes the accomplished tasks and proposes further investigations in the field.

Chapter II. Technical Background

2.1 Classification of Sensors

A sensor is a device that responds to a physical (or chemical) stimulus (such as heat, light, sound, pressure, magnetism, or a particular motion) and transmits a resulting impulse (as for measurement or operating a control). Thus, a sensor can detect an input signal (or energy) and convert it to an appropriate output signal (or energy). Since the early 1980s, there has been tremendous growth and progress in the development of a variety of sensors. These sensors, with their ever-improving performance-cost ratio, will be key components in the further penetration of microelectronics into new products and new applications. The key characteristic of a sensor is the conversion of energy from one form to another. It is, therefore, useful to consider the various forms of energy. From a physical point of view, we can distinguish the sensors by the forms of converted energy. Generally, there are six types of sensing signals: 1.Chemical signal; 2.Electrical signal; 3.Magnetic signal; 4.Mechanical signal; 5.Radiant signal; 6.Thermal signal. Considering the real time applications, some sensors in the subcategories are so important that we have to study them individually. Therefore, the sensors can be divided into seven categories: (1) Chemical sensors; (2) Acoustic sensors; (3) Magnetic sensors; (4) Mechanical sensors; (5) Radiation sensors; (6) Thermal sensors; (7) Biosensors [9].

In order to compare sensors and obtain a comprehensive overview of them, a flexible classification scheme has been proposed by White [10]. Table 2.1 lists the measurands, which are defined as the input quantities, properties, or condition that are detected or measured by the sensor.

- | | |
|----------|--|
| 1 | Acoustic |
| | <ul style="list-style-type: none"> • Wave amplitude, Phase, polarization, spectrum • Wave velocity • Other (specify) |
| 2 | Biological |
| | <ul style="list-style-type: none"> • Biomass (identities, concentrations, states) • Other (specify) |
| 3 | Chemical |
| | <ul style="list-style-type: none"> • Components identities, concentrations, states) • Other (specify) |
| 4 | Electric |
| | <ul style="list-style-type: none"> • Charge, current • Potential, potential difference • Electric field (amplitude, phase, polarization, spectrum) • Conductivity • Permittivity • Other (specify) |
| 5 | Magnetic |
| | <ul style="list-style-type: none"> • Magnetic field (amplitude, phase, polarization, spectrum) • Magnetic flux • Permeability • Other (specify) |
| 6 | Mechanical |
| | <ul style="list-style-type: none"> • Position (linear, angular) • Velocity • Acceleration • Force • Stress, pressure • Strain • Mass, density • Moment, torque • Speed of flow, rate of mass transport • Shape, roughness, orientation • Stiffness, compliance • Viscosity • Crystallinity, structural integrity • Other (specify) |
| 7 | Optical |
| | <ul style="list-style-type: none"> • Wave amplitude, phase, polarization, spectrum • Wave velocity • Other (specify) |
| 8 | Radiation |
| | <ul style="list-style-type: none"> • Type • Energy • Intensity • Other (specify) |
| 9 | Thermal |
| | <ul style="list-style-type: none"> • Temperature • Flux • Specific heat • Thermal conductivity |

Table 2.1 Measurands of Sensors [10]

2.2 Chemical and Biological Sensors

This review will mainly focus on the chemical and biological sensors for gas and liquid phase applications. In order to have a vivid picture of biosensor, let us start with a great example of a natural sensor, the human olfactory system. An extensive work has been done in the field of sensors to mimic the function of this ‘natural sensor’ to create an artificial nose that can detect very low concentrations and chemically as diverse as nose. Understanding the function of human olfactory system is therefore necessary before studying manmade sensors. The olfactory system of humans consists of several million olfactory sensory neurons arrayed in a sensory epithelium located inside the nasal cavity. Each of these sensory neurons expresses one of approximately 350 odorant receptor genes, which confers upon that neuron a specific sensitivity to the set of odor molecules that will bind and activate the respective odorant receptor. It is widely believed that only a small region of the odor molecule is recognized by a given odorant receptor. Therefore, unlike hearing or seeing, olfaction is not a spectral sense, but rather consists of a large number of sensors with different specificities and affinities. Any given odor may activate only a single receptor or many different receptors. On the other hand an odorant receptor can be very specific and only be activated by very few odor molecules or be more promiscuous and recognize a variety of odor molecules. The posterior of the nose has a region called epithelium, which plays a major role in odor detection. This region has specialized cells called neurons, which establishes contact between brain and the outer world. The hair like structures called cilia protruding from neuron extends out of each cell and has direct contact with odor. The other end of the cell is a fiber known as axon, which enters the brain. The odor molecule usually comes into contact with cilia that have

a special protein for sensing purposes. This protein builds itself around odor molecule and this sends an electrical signal to the olfactory bulb. The olfactory bulb acts as a relay station and transfers signal to cortex of the brain where the interpretation of odor is done [11, 12].

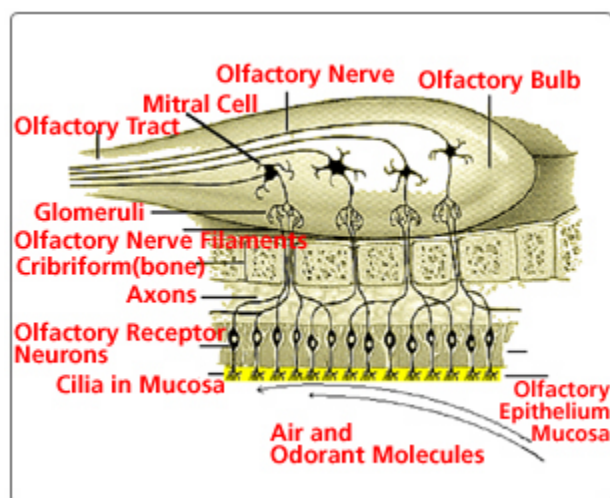


Fig 2.1 The schematic of human olfactory system. (www.leffingwell.com)

A sensor mainly consists of two parts. First, an interactive material which interacts with environment and generates a response. The second part is a device, which reads the response and converts it in to an interpretable and quantifiable term. The interactive material is the sensor's heart and can be considered as the primary part of a sensor. The nature, selectivity and sensitivity of a chemical sensor depend upon these interactive materials used. As material gets complex, the responses to different molecules are possible and hence increase in the sensing capabilities.

This interactive material is an interface between environment and the transducer. Usually the sensing material captures a molecule with a certain selectivity that induces physical changes in material because of captured molecule's chemical interaction with

the material. The physical variations are called as ‘intermediate quantities’. The choice of a particular interactive material is based on the sensitivity, selectivity, reliability and the reversibility of the related sensing mechanisms [13].

Bio-technology has become one of the most rapidly growing technologies in the past 20 years. Biosensors are becoming exciting and promising as a strong tool in bioanalytical research. With many distinct advantages, biosensors are finding increased usage and applications in the fields of biotechnology, physics, chemistry, genomics, medicine, cell-monitoring systems, aviation, oceanography, and environmental control. To recognize a specific analyte, four main groups of biological sensing elements are used: Enzymes, Antibodies, Nucleic Acids and Receptors. Enzymes are natural protein biocatalysts that act specifically on a unique substrate or groups of substrates. An antibody is a molecule produced by animals in response to an antigen and which binds to the antigen specifically. The ability of a single strand nucleic acid molecule to recognize and bind (hybridize) to its complementary partner in a sample can be used in a biosensor. Naturally occurring receptors are non-catalytic proteins that span cell membranes, extending into both the extracellular and intracellular spaces. Within an organism they act as links in cell-cell communication by reversibly binding specific neurotransmitters and hormones liberated from another cell for the purpose of initiating or diminishing its cellular activity. Neurotransmitters and hormonal receptors are the body's own biosensors.

In order for the transducer to accept signals from the biological component properly, the biological component has to be intimately connected to the transducer.

There are a number of immobilization methods which have evolved, such as adsorption, microencapsulation, entrapment, covalent attachment and cross-linking.

There are various technologies based on which sensors are developed. Namely, fiber optic, semiconducting, conducting polymer based, mechanical, electrochemical, calorimetric, colorimetric, piezoelectric (especially, surface acoustic wave) sensors. In this section all these above listed sensor technologies are discussed with respect to their function, advantages, capabilities and requirements.

Fiber Optic Sensors:

It is essential to know the function of an optical fiber before studying its application in sensors. Principle of optical sensing using fibers are delineated by Walt [14] as follows; an optical fiber consists of two types of transparent media. The core, in which optical signal is transmitted and the clad, which is a thin layer of lower refractive index material. The refractive index mismatch enables the core-clad interface to act effectively as a mirror enabling light transmission entering the fiber through total internal reflection.

For using this fiber as a sensor, usually an indicator material is immobilized on the tip of the fiber. The chemical interaction of this material with the analyte of interest includes a physical change in fluorescent intensity, wavelength, spectral shift or it could be any of this, which will be carried to detection system where it is analyzed for the analyte.

Fiber optic sensors can either be based on direct or indirect way of sensing. In direct sensing, intrinsic properties of an analyte are measured. Where as in the indirect sensing, the sensing part of a sensor may be an immobilized dye or a conducting polymer or may be a silicon cantilever. Most of the sensors do use fiber optics technology in some

or the other form and hence can be said that the fiber optic sensor is one of the most important type of sensor technology.

The fiber luminescence could be extended for fiber imaging to study the various analytes. For example, quenching of luminescence is observed in some dyes such as porphyrins upon exposure to very minute concentrations of oxygen. Fiber imaging can be used to study these oxygen concentrations. The presence of oxygen can increase the quantum yield in tetraphenylporphyrins and this can be detected by a dye contained in the clad. This is an example of a fiber optical sensor that detects 100ppm to 1% of oxygen [15].

The fiber optic sensors can be used for different purposes such as for detecting gas vapors, humidity, ions and organic compounds. The humidity sensors were developed based on fiber inclusions that undergo length variations as function of humidity. For the detection of inorganic ions, thin film sol-gels developed with ion responsive lipid bilayers, which were coupled to a bifurcated fiber optic bundle to produce a metal ion probe, ionic and neutral crown ethers were immobilized on anionic polymer membranes to give sensors for determination of Barium and Copper [16].

Similarly it has been reported that, fiber optic based sensors can be used for sensing pollutants, explosives, drugs, pharmaceuticals and miscellaneous organics. The fiber optic sensors can be used for the detection of organic compounds as follows. Chlorinated hydrocarbons can be detected in the gas phase with optical fiber coated with porous silica. Direct spectroscopy via fiber optics also enables detection of aromatic compounds via evanescent wave absorption spectroscopy. Also pollutants such as chlorinated hydrocarbons may be sensed by fiber optic surface plasmon resonance using

alkenethiol coated silver films. Explosive materials may be detected with optical fiber arrays containing different reactive sensor tips. Neural networks are best suited to discriminate between organic volatiles using pattern recognition [16].

Walt reports those essential features of a sensor such as small size, array format and cross reactivity can be incorporated into optical sensor arrays [14]. Optical sensors are information rich. The optical signals can be interrogated and collected at multiple wavelengths with different signal intensities, different phases, polarization and excited state lifetimes. All these factors make optical fiber sensors unique and practical.

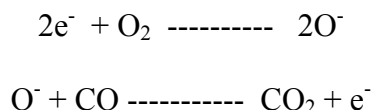
Sensors Based on Conducting Properties:

Though many sensors such as semiconducting sensors, conducting polymer based sensors, silicon carbide based sensors, tin oxide based sensors, zinc oxide based sensors can broadly be classified under one category, in this section all these sensors have been discussed separately as they have different applications and slightly different functioning mode which necessitates separate classification.

- **Semiconductive Gas Sensors:**

Some semiconducting oxides such as tin oxide (SnO_2) and zinc oxide have surface conductance and this is influenced by the composition of gas present in ambience. Tin oxide based semiconductors are widely used in the detection of reducible gases like carbon monoxide, hydrogen and methane at low concentrations. As an active sensing part of this sensor, tin oxide is in non-stoichiometric form and is deficient in oxygen atoms. Charge neutrality is maintained by the presence of Sn^{2+} ions instead of Sn^{4+} ions, and Sn^{2+} donates electrons during the process. Thus, the active material of tin oxide is an n-type semiconductor. At high temperatures oxygen is absorbed on the tin oxide film and

this oxygen accepts electrons donated by Sn^{2+} ions, and thus SnO_2 film becomes ionic. If a reducing gas adsorption follows, the reducing gas may react with the adsorbed oxygen anions and becomes a positively charged species. Alternatively, the reducing gas may react with the adsorbed oxygen atom and release bound electrons. An example of CO reaction with SnO_2 film surface is



where e^- represents a conduction band electron. In the absence of reducing gas, electrons are removed from the conduction band via the reduction of molecular oxygen and an O^- species is formed. Consequently, the SnO_2 film becomes highly resistive. When CO is introduced, it undergoes oxidation to carbon dioxide by surface oxygen anion O^- and electrons are reintroduced into the conductive band, which increases the conductivity of the film. This is the general operation principle of the tin oxide based gas sensors.

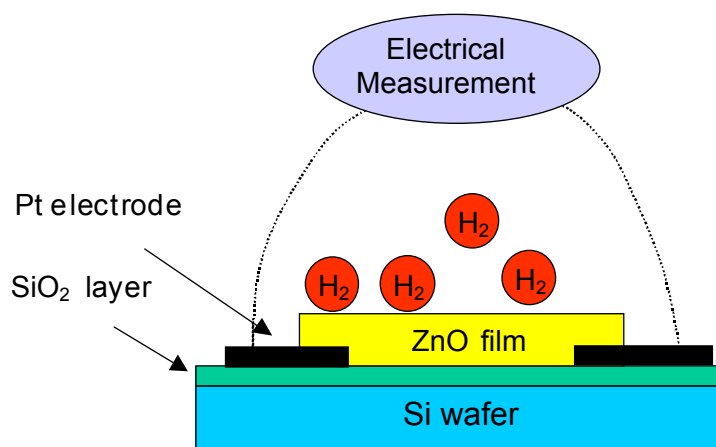


Fig 2.2 ZnO semiconducting gas sensor

Zinc oxide (ZnO) is an important multifunctional material with applications such as varistors, gas sensors, SAW devices, transparent electrodes, catalysts etc. The various applications of ZnO are due to the specific chemical, surface and microstructural properties of this material. The microstructural and physical properties of ZnO can be modified by introducing changes into the procedure of its chemical synthesis. Especially for the application of ZnO as gas sensors porous microstructure of the materials with controlled pore size is preferred. The sensitivity and response time of ZnO based sensors strongly depend on the porosity of the material. The grain size of the polycrystalline zinc oxide material also has noticeable effect on its gas sensing properties. It has been experimentally observed [17] that the gas sensitivity of the ZnO sensors decreases with the increase of its mean grain size. The change in film resistance was noted in different concentrations of the test gas at several temperatures. The sensitivity $[(R_{\text{air}} - R_{\text{gas}})/R_{\text{air}}]$ defined as the percentage change of the film resistance in presence of the test gas was calculated for each temperature and concentration of the test gas. The Interface-Gas adsorption induces space charge barrier, and modulate the surface conduction and grain boundary barrier.

Figure 2.2 is a prototype of ZnO conductive type gas sensor. These sensors usually require a catalyst metal (such as Pt) in order to be sensitive to specific gases (such as hydrogen, oxygen, carbon monoxide, methane, ammonia, Figure 2.3). The operation temperatures are very high, ranging from 300°C to 700°C.

Those sensors have some advantages including high sensitivity, low cost, fast response, and low power consumption. However, factors such as long-term drift, relative

low selectivity and interference of humidity and temperatures make up drawbacks of semi conductive sensors.

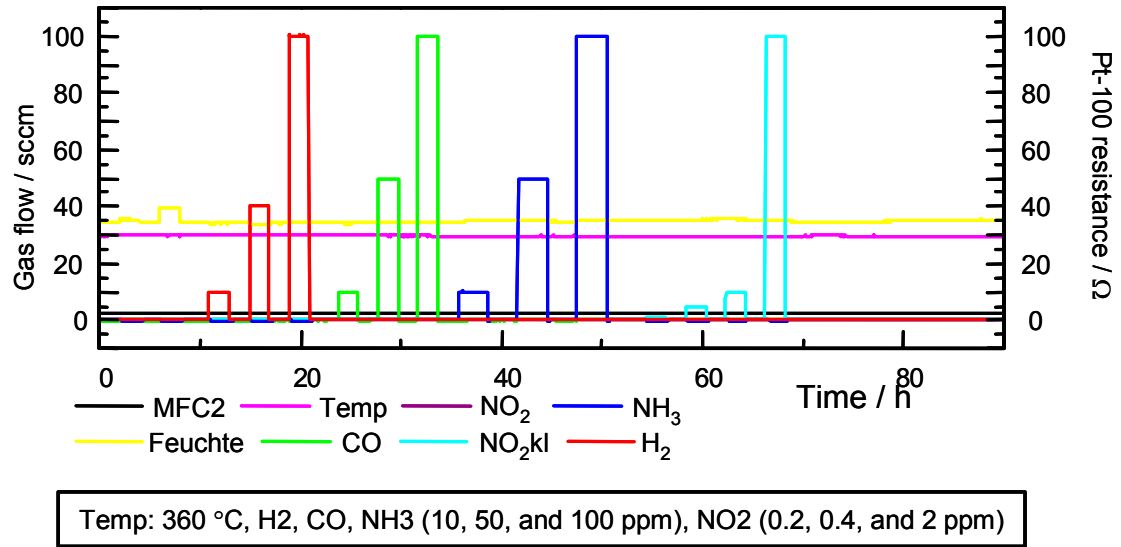


Fig 2.3 ZnO conductive gas sensor for different gas sensing [18]

- **Silicon Carbide (SiC) Based Gas Sensors:**

Chen et al., [19] have exploited the major advantage of silicon carbide, which operates at higher temperatures above 600° C mainly because of wide band gap and low intrinsic carrier concentration. This is the very reason for which silicon carbide semiconductors have been used as schottky diode gas sensors. The gases, which are not detectable at low temperatures such as hydrogen and hydrocarbons, are now detectable by this material. Lundstorm et al., [20] have investigated the metal insulated semiconductor capacitor or metal semiconductor structure with silicon carbide as the

semiconductor. Silicon carbide as semi conducting material has been successful in detecting hydrogen and hydrocarbon as low as 2.5 ppm concentration at temperature as high as 800° C. These sensing capacities have also been reported for hydrocarbons such as methane, ethane and propane. The reported response time is around 100 mili seconds.

In contrast to above work where silicon carbide is used as capacitors, Chen et al. [19] have used it as semiconductor that responds to analyte with large signals for low concentration which increases the sensitivity of the sensor. They have developed a silicon carbide based sensor by depositing palladium on silicon carbide diode. Palladium was used because of its superior ability to absorb hydrogen.

The dissociation of hydrogen on the metal surface leads to the formation of a dipole layer at the interface of the metal and semiconductor. This dipole layer changes the electric properties of the devise in proportion to the hydrogen present in ambience. Silicon carbide based sensors allows the sensor operation in environments and applications where silicone based sensors are inoperative and especially for detecting hydrogen at temperatures beyond the capabilities of silicone sensors.

- **Conducting Polymer Based Sensors:**

The sensor has an array of elements having polymer coating that has conducting properties. The change in electrical resistance upon exposure to various analytes leads to the identification and quantification of gaseous vapors. This devise yields very low power DC signals, which can be used for identification either by software or hardware based neural networks.

The approach aims mainly at controlling the chemical properties of polymer layer to be coated on the sensor. The conducting organic polymer can be plasticized during

deposition providing symmetric control over the binding properties of each chemiresistor element. A thin conducting organic polymer films have been prepared and immobilized on a non-conducting surface, which on exposure to different analytes produce different electrical resistance. An array of such engineered polymer films produces a signal pattern for specific analytes and hence identification is possible. The sensor has been tested with eight vapors: acetone, benzene, chloroform, ethanol, isopropyl alcohol, methanol, tetra hydrofuron and ethyl acetate. These eight vapors were evaluated over a period of five days on a fourteen-element sensor. The results of these tests show that each vapor could be clearly identified from others [21].

This sensor array design has an easy way to construct polymer organic layer, which gives a direct control over the chemical properties. Thinner the polymer film gets lesser the response time becomes.

Mechanical Sensor:

The mechanical sensor is constructed of micro fabricated array of silicon cantilevers. Each individual cantilever in the array is coated with layers of sensing materials such as silicon oxide, platinum, and gold for the detection of analytes. The cantilevers when exposed to analytes respond by bending caused by surface stress induced on the cantilever by chemisorbing or physisorbing of analyte molecule on the coated surface of the cantilever. Ethene and water vapor are detected with the sensor [22].

The compactness of the sensor along with the low quantities it can detect makes it feasible for practical applications. The inclusion of 'reference cantilevers' allows the usage of sensors under disturbing conditions such as turbulent gas flow, mechanical variations, abrupt pressure changes etc. These reference cantilevers basically do not

respond to analyte but do respond to all the above said undesired conditions, which interfere with of sensor's proper function. The difference in bending between reference cantilevers and sensor cantilevers allows to eliminate the errors caused by factors such as turbulent gas flow, vibrations etc.

A modular and expandable unit does optical readout of deflection, data acquisition and processing. The whole process of sensing or analyte detecting can be explained as follows. On exposure to gas, the coated cantilever deflects due to adsorption and this deflection is in response to the chemical and physical reaction of the analyte with the coated material of the cantilever. The position-sensitive deflector is used for converting the nanomechanical response that is 'bending' in to electrical voltage signals. This electrical signal is amplified and fed to an analog to digital converter. All the individual cantilevers have individual light sources and a micro controller board via BUS, which periodically transfers data to a personnel computer, which controls the whole module.

An automated analyte dosing system controlled by a digital mass flow controller used for gas flow adjustments. The eight beam silicon cantilevers naturally coated with native oxide of silicon are used in the experiment having length, breadth and thickness of 500 μm , 100 μm and 1 μm respectively.

The working of sensor is demonstrated by using ethene and water vapor. For the detection of ethene, platinum coating is used on the silicon cantilever, and gold for water vapor detection. For ethene detection, platinum coated surface acts as a sensor layer where as for water vapor detection native silicon oxide acts as sensor layer since gold layer is inert to water vapor.

The working of reference cantilevers can be seen in detection of water vapor. Here four cantilevers are coated with gold only on one side and rest of the four cantilevers are coated with gold layers on both sides. The cantilevers coated on both sides act as reference layers and the difference of deflections between these two can be used for nullifying undesired interfering factors causing deflection.

Colorimetric sensors:

- **Fiber-optic Based Colorimetric Sensor:**

An effort has been made to develop a sensor that imitates the human olfactory system based on the unique 'signature' created by an analyte. The system involves an immobilized polymer on the tip of a fiber optic. The interaction of both polymer and analyte can give different fluorescent response patterns. This response may be in the form of spectral shifts, intensity changes, spectral shape variations or temporal responses. The temporal response is video imaged and the signals are used for training a neural network for vapor recognition. Unlike other sensors, the information about an analyte is captured in a distributed fashion which enables clear discrimination between closely related analytes. The optical techniques when used for observing many parameters makes sensor more powerful and sensitive to multi analytes with less sensor elements.

In this sensor, Nile red polymer dye is immobilized on the tip of the fiber. This Nile red dye of varying polarity, hydrophobicity, pore size, flexibility and swelling tendencies creates unique sensing regions which interact differently with individual vapors for different organic vapors. Individual sensors in the fiber array gave different fluorescent responses to different organic vapors. These different profiles are then tested for reproducibility, which makes analyte recognition possible. The neural networks are

trained with many consecutive trials and tested with another set of data for validation. This neural network gives precise results for different analytes with temporal data [23].

- **Metalloporphyrin Based Colorimetric Sensor:**

The quality of metalloporphyrin's changing color upon ligand binding has been exploited here. An array of metalloporphyrin dyes when exposed to different analytes, change color thereby creating a unique fingerprint for that concentration of analyte. Hence a library of these immobilized chemo selective vapor sensing dyes allows identification of vapor ligating analytes. The major achievement of this technique over other chemical sensors is the 'inertness' of the dye towards water vapor that interferes with the operation of most of the other sensors. The large spectral shifts and open coordinating sites for axial ligation are some of the important qualities of these metalloporphyrins. The correlation between magnitude of spectral shift and polarizability of the ligand provides the electronic base for analyte distinction.

It has been reported that this device has an edge over other sensors in many respects, such as low cost, minimum and less complicated signal transduction hardware requirement. The device can detect concentrations less than 2ppm and 100 ppb, which is close to the capabilities of mammalian olfactory system [24].

The exposure changes the color and hence, the images. These images can be scanned by an ordinary flat bed scanner using a software. The two images can then be subtracted, or difference between first and second image creates a 'signature' of an analyte that enables identification and quantification of vapor.

The dyes used by Rakow and Suslick [24] in their sensor array is a solution of various metallated tetra porphyrins in either methylene chloride or chlorobenzene. The

sensor array was prepared by spotting the above-prepared dye on reverse phase thin layer silica chromatography plate. The RGB values i.e., color change data varies monotonically with the porphyrin concentration. By plotting this data, a single analyte can be quantified and a good linear plot will still be observed until each porphyrin's spot is reached its saturation. The usage of reverse phase silica as a base serves two purposes, firstly it provides a non interacting medium for metalloporphyrin array and secondly it is hydrophobic in nature which makes it insensitive to water vapor making it an excellent materials for using in vapor sensing.

Also, deposition of metalloporphyrin on the surface of teflon has shown improved response time and differentiation between analytes is possible at molecular level by using shape selective distinction.

Calorimetric Sensors:

These sensors are basically high temperature resistance thermometers, which measures the change in the temperature caused by the heat evolution during the catalytic oxidation of combustible gases. Usually encapsulated platinum coil is used as calorimetric sensors since it serves both as heater and resistance thermometer. Though results are not accurate because of heat losses these sensors are used in detecting combustible gases at low concentrations. Other calorimetric sensors use platinum black and palladium. A thin film thermopile sensor based on bismuth- antimony junction consists of alternative junctions of bismuth and antimony with gold contact between on a thick kapton film formed on a glass plate.

Electro-Chemical Sensors:

The development of electrochemical cells is based on basic electro-analytical principles. These sensors are developed from electrochemical cells with two or three electrodes in contact with a solid or a liquid electrolyte. The selectivity and sensitivity differs from analyte to analyte. Each analyte interacts differently with electrochemical cell to produce a different and specific signal. Variation in the cell may be capacitance, resistance, voltage, and current. Each of the above change is measurable. Based on the above factors, electrochemical sensors can be classified as capacitance or conductive sensors, potentiometric sensors and amperometric sensors, respectively.

An electrochemical conductivity sensor measures the change in conductivity in an electrochemical cell. Potentiometric sensors use the effect of the chemical concentration on the equilibrium due to the redox reaction occurring at the electrode-electrolyte interface of the electrochemical cell. A potential may develop at the interface because of redox reactions. Potentiometric sensors can either be an inert electrode or an active electrode sensor. Inert electrode sensor has noble metals such as platinum, gold etc. Active electrode sensors include many of the ion selective electrode sensors. Usually active electrode often incorporates a specific functional membrane, which may have ion selective, ion permeable or ion exchange properties. In both cases irrespective of active or inactive electrode, other half of the cell is reference electrode for completing the potentiometric measurement.

Bio-Optical Sensing

Optical imaging plays a very important roll in biosensing area. There are basically four types of bio-imaging: scatter, absorption, fluorescence and bioluminescence (Figure 2.4). Scatter includes intrinsic scatter of tissues and exogenous scatters of gold and silver

particles; Absorption mainly is intrinsic tissue absorption; Fluorescence covers tissue auto-fluorescence, fluorescent dyes and fluorescent proteins-reporter genes; Bioluminescence basically is from the bioluminescent proteins-reporter genes. Fluorescent dyes are the most widely used in the biochemical and biological area nowadays.

Scatter

Absorption

Fluorescence

Bioluminescence

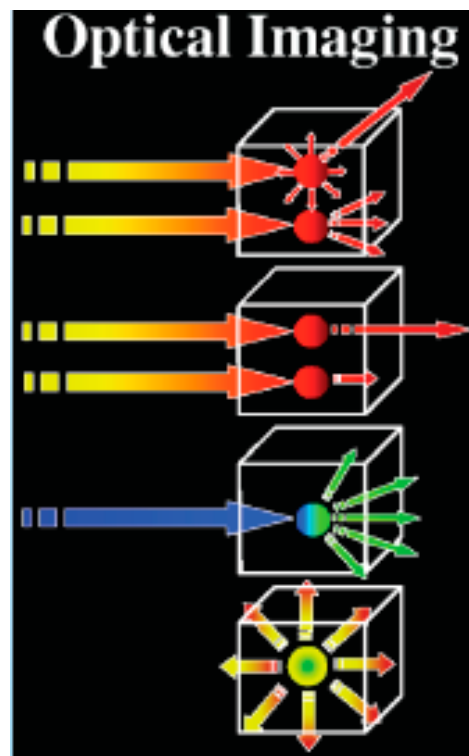


Fig. 2.4 Four types of optical imaging for biosensing [25]

The current bio-optical sensing requires large instrument, such as laser, confocal microscope and detector. Although the optical method is the most accurate way to detect and analysis biological agents, the high instrument requirement makes this technology limited to the laboratory analysis, not for the real in-vivo sensing and detecting. With the development of nanotechnology, it is possible to integrate nano-laser, nanodetector, micro-optics into a single chip, which makes the nanoscale lab-on-chip very promising

for the future. Development of simulation tools is also critical to enable sensor design and evaluation prior to fabrication.

Near IR imaging has recently become a new trend in the bio-imaging research area. Near IR tags can be attached to a molecular marker that is monitoring increased/decreased concentration in tissue of protease enzymes, glucose, and cell surface markers. By near IR imaging, we can monitor cellular events and cell populations including detection of cancer cells, programmed cell death (apoptosis), stem cell development, and influence of target drug treatments. The low autofluorescence from background in near IR imaging technology allows good SNR (signal to noise ratio) in fluorescence sensing. The number of near IR tags for cellular, DNA and protein tagging excited above 650 nm, can be increased a lot. [26]

2.3 Acoustic Wave Sensors

2.3.1. Introduction

Acoustic wave devices have been in commercial use for more than 60 years. The telecommunications industry is the largest consumer, accounting for ~3 billion acoustic wave filters annually, primarily in mobile cell phones and base stations. These are typically surface acoustic wave (SAW) devices, and act as bandpass filters in both the radio frequency and intermediate frequency sections of the transceiver electronics. Several of the emerging applications for acoustic wave devices as sensors may eventually equal the demand of the telecommunications market. These include automotive applications (torque and tire pressure sensors), medical applications (chemical sensors), and industrial and commercial applications (vapor, humidity, temperature, and mass sensors). Acoustic wave sensors are competitively priced, inherently rugged, very

sensitive, and intrinsically reliable. Some are also capable of being passively and wirelessly interrogated (no sensor power source required).

Acoustic Wave Technology Overview

Acoustic wave sensors are so named because they utilize a mechanical, or acoustic, wave as the sensing mechanism. As the acoustic wave propagates through or on the surface of the material, any changes to the characteristics of the propagation path affect the velocity and/or amplitude of the wave. Changes in velocity can be monitored by measuring the frequency or phase characteristics of the sensor and can then be correlated to the corresponding physical quantity being measured.

Virtually all acoustic wave devices and sensors use a piezoelectric material to generate the acoustic wave. Piezoelectricity was discovered by brothers Pierre and Paul-Jacques Curie in 1880, received its name in 1881 from Wilhelm Hankel, and remained largely a curiosity until 1921, when Walter Cady discovered the quartz resonator for stabilizing electronic oscillators [27]. Piezoelectricity refers to the production of electrical charges by the imposition of mechanical stress. The phenomenon is reciprocal. Applying an appropriate electrical field to a piezoelectric material creates a mechanical stress. Piezoelectric acoustic wave sensors apply an oscillating electric field to create a mechanical wave, which propagates through the substrate and is then converted back to an electric field for measurement.

2.3.2. Piezoelectricity

Piezoelectric Materials

Among the piezoelectric substrate materials that can be used for acoustic wave sensors and devices, the most common are quartz (SiO_2), lithium tantalate (LiTaO_3), and,

to a lesser degree, lithium niobate (LiNbO_3). Each has specific advantages and disadvantages, which include cost, temperature dependence, attenuation, and propagation velocity. Table 2.2 lists some relevant specifications for each material, including the most popular cuts and orientations [28]. An interesting property of quartz is that it is possible to select the temperature dependence of the material by the cut angle and the wave propagation direction. With proper selection, the first order temperature effect can be minimized. An acoustic wave temperature sensor may be designed by maximizing this effect. This is not true of lithium niobate or lithium tantalate, where a linear temperature dependence always exists for all material cuts and propagation directions. Other materials with commercial potential include gallium arsenide (GaAs), silicon carbide (SiC), langasite (LGS), zinc oxide (ZnO), aluminum nitride (AlN), lead zirconium titanate (PZT), and polyvinylidene fluoride (PVdF).

Piezoelectric Thin Films

During the past decade, many researchers reported useful characteristics of piezoelectric films for different methods of growth and different applications [29, 30]. There are many piezoelectric films reported. The three films most popular with the sensor industry are ZnO, AlN and PZT. Table 2.3 shows a summary of possible applications and potential use of these films [9].

Table 2.2 Physical Parameters of More Commonly Used Piezoelectric Materials[28]

Material	Orientation	Velocity (m/s)	Temperature Coefficient (ppm/°C)	Attenuation at 1 GHz (dB/μS)	Cost
Quartz	Y, X	3159	-24	2.6	Lowest
Quartz	ST, X	3158	0	3.1	Lowest
Lithium Tantalate	Y, Z	3230	35	1.14	Medium
Lithium Tantalate	167 rotation	3394	64	-	Medium
Lithium Niobate	Y, Z	3488	94	1.07	High
Lithium Niobate	128 rotation	3992	75	-	High

Table 2.3 Applications Summary of Three Major Piezo-films: ZnO, AlN and PZT[9]

Applications	Piezoelectric Materials			
	ZnO	AlN	PZT	Others
Pressure sensors	√			√
Gas sensors	√			√
Bulk acoustic resonators	√	√		
Plate mode sensors	√			√
Accelerometers	√			√
TV VIF filters	√		√	
SAW devices	√	√	√	
Actuator / translator	√		√	

Acoustic Wave Propagation Modes

Acoustic wave devices are described by the mode of wave propagation through or on a piezoelectric substrate. Acoustic waves are distinguished primarily by their velocities and displacement directions; many combinations are possible, depending on the material and boundary conditions. The IDT of each sensor provides the electric field necessary to displace the substrate and thus form an acoustic wave. The wave propagates through the substrate, where it is converted back to an electric field at the IDT on the other side. Transverse, or shear, waves have particle displacements that are normal to the direction of wave propagation and which can be polarized so that the particle displacements are either parallel to or normal to the sensing surface. Shear horizontal wave motion signifies

transverse displacements polarized parallel to the sensing surface; shear vertical motion indicates transverse displacements normal to the surface.

A wave propagating through the substrate is called a bulk wave. The most commonly used bulk acoustic wave (BAW) devices are the thickness shear mode (TSM) resonator and the shear-horizontal acoustic plate mode (SH-APM) sensor.

If the wave propagates on the surface of the substrate, it is known as a surface wave. The most widely used surface wave devices are the surface acoustic wave sensor and the shear-horizontal surface acoustic wave (SH-SAW) sensor, also known as the surface transverse wave (STW) sensor.

All acoustic wave devices are sensors in that they are sensitive to perturbations of many different physical parameters. Any change in the characteristics of the path over which the acoustic wave propagates will result in a change in output. All the sensors will

function in gaseous or vacuum environments, but only a subset of them will operate efficiently when they are in contact with liquids. The TSM, SH-APM, and SH-SAW all generate waves that propagate primarily in the shear horizontal motion. The shear horizontal wave does not radiate appreciable energy into liquids, allowing liquid operation without excessive damping. Conversely, the SAW sensor has a substantial surface-normal displacement that radiates compression waves into the liquid, thus causing excessive damping. An exception to this rule occurs for devices using waves that propagate at a velocity lower than the sound velocity in the liquid. Regardless of the displacement components, such modes do not radiate coherently and are thus relatively undamped by liquids.

Other acoustic waves that are promising for sensors include the flexural plate wave (FPW), Love wave, surface-skimming bulk wave (SSBW), and Lamb wave. Before turning to application examples, it is helpful to briefly review each sensor type.

2.3.3. Bulk Acoustic Wave Devices

Bulk Wave Sensors--Thickness Shear Mode Resonator

The TSM, widely referred to as a quartz crystal microbalance (QCM), is the best-known, oldest, and simplest acoustic wave device. The TSM typically consists of a thin disk of AT-cut quartz with parallel circular electrodes patterned on both sides. The application of a voltage between these electrodes results in a shear deformation of the crystal.

This device is known as a resonator because the crystal resonates as electromechanical standing waves are created. The displacement is maximized at the crystal faces, making the device sensitive to surface interactions. The TSM resonator was

originally used to measure metal deposition rates in vacuum systems where it was commonly used in an oscillator circuit [31]. The oscillation frequency tracks the crystal resonance and indicates mass accumulation on the device surface. In the late 1960s, the TSM resonator was shown to operate as a vapor sensor.

The TSM features simplicity of manufacture, ability to withstand harsh environments, temperature stability, and good sensitivity to additional mass deposited on the crystal surface [32]. Because of its shear wave propagation component, the TSM resonator is also capable of detecting and measuring liquids, making it a good candidate for a biosensor. Unfortunately, these devices have the lowest mass sensitivity of the sensors examined here. Typical TSM resonators operate between 5 and 30 MHz. Making very thin devices that operate at higher frequencies can increase the mass sensitivity, but thinning the sensors beyond the normal range results in fragile devices that are difficult to manufacture and handle. Recent work has been done to form high-frequency TSM resonators using piezoelectric films and bulk silicon micromachining techniques [33].

Bulk Wave Sensors--Shear-Horizontal Acoustic Plate Mode Sensors

These devices use a thin piezoelectric substrate, or plate, functioning as an acoustic waveguide that confines the energy between the upper and lower surfaces of the plate. As a result, both surfaces undergo displacement, so detection can occur on either side. This is an important advantage, as one side contains the interdigital transducers that must be isolated from conducting fluids or gases, while the other side can be used as the sensor.

As with the TSM resonator, the relative absence of a surface-normal component of wave displacement allows the sensor to come into contact with liquid for biosensor

applications. SH-APM sensors have been successfully used to detect microgram-per-liter levels of mercury, which is adequate for Safe Drinking Water Act compliance testing [34]. Although more sensitive to mass loading than the TSM resonator, SH-APM sensors are less sensitive than surface wave sensors. There are two reasons: The first is that the sensitivity to mass loading and other perturbations depends on the thickness of the substrate, with sensitivity increasing as the device is thinned. The minimum thickness is constrained by manufacturing processes. Second, the energy of the wave is not maximized at the surface, which reduces sensitivity.

2.3.4. Surface Acoustic Wave Devices

Surface Wave Sensors-- Surface Acoustic Wave Sensors

In 1887, Lord Rayleigh discovered the surface acoustic wave mode of propagation [35] and in his classic paper predicted the properties of these waves. Named for their discoverer, Rayleigh waves have a longitudinal and a vertical shear component that can couple with a medium in contact with the device's surface. Such coupling strongly affects the amplitude and velocity of the wave. This feature enables SAW sensors to directly sense mass and mechanical properties. The surface motion also allows the devices to be used as microactuators. The wave has a velocity that is ~ 5 orders of magnitude less than the corresponding electromagnetic wave, making Rayleigh surface waves among the slowest to propagate in solids. The wave amplitudes are typically ~ 10 Å and the wavelengths range from 1 to 100 microns [36].

Because Rayleigh waves have virtually all their acoustic energy confined within one wavelength of the surface, SAW sensors have the highest sensitivity of the acoustic sensors reviewed.

Typical SAW sensors operate from 25 to 500 MHz. One disadvantage of these devices is that Rayleigh waves are surface-normal waves, making them poorly suited for liquid sensing. When a SAW sensor is contacted by a liquid, the resulting compressional waves cause an excessive attenuation of the surface wave.

Surface Wave Sensors-- Shear-Horizontal Surface Acoustic Wave Sensors

If the cut of the piezoelectric crystal material is rotated appropriately, the wave propagation mode changes from a vertical shear SAW sensor to a shear-horizontal SAW sensor. This dramatically reduces loss when liquids come into contact with the propagating medium, allowing the SH-SAW sensor to operate as a biosensor.

Comparison of Acoustic Wave Sensors

In general, the sensitivity of the sensor is proportional to the amount of energy in the propagation path being perturbed. Bulk acoustic wave sensors typically disperse the energy from the surface through the bulk material to the other surface. This distribution of energy minimizes the energy density on the surface, which is where the sensing is done. SAW sensors, conversely, focus their energy on the surface, tending to make them more sensitive [36, 37] (see Table 2.4). Other design considerations when selecting acoustic wave sensors include oscillator stability and noise level.

Table 2.4 Comparison of Acoustic Sensors[36, 37]

Sensor Type	Sensitivity $\frac{\Delta f}{f_c}$ $\frac{\Delta M}{Area}$ $\frac{Hz / MHz}{ng / cm^2}$	Factors Determining Sensitivity	Motion at Device Surface	Immersible	Operating Frequency	Mechanical Strength
TSM	Low (0.014)	Plate Thickness	Transverse	Yes	Low (5-20 MHz)	Med
APM	Low-Med (0.019)	Plate Thickness, IDT Finger Spacing	Transverse	Yes	Med-High (25-200 Mhz)	Med
SAW	High (0.20)	IDT Finger Spacing	Normal and Transverse	No	High (30-500 MHz)	High
SH-SAW	Med-High (0.18)	IDT Finger Spacing	Transverse	Yes	High (30-500 MHz)	High

Sensor Applications

All acoustic wave sensors are sensitive, to varying degrees, to perturbations from many different physical parameters. As a matter of fact, all acoustic wave devices manufactured for the telecommunications industry must be hermetically sealed to prevent any disturbances because they will be sensed by the device and cause an unwanted change in output.

The range of phenomena that can be detected by acoustic wave devices can be greatly expanded by coating the devices with materials that undergo changes in their mass, elasticity, or conductivity upon exposure to some physical or chemical stimulus. These sensors become pressure, torque, shock, and force detectors under an applied stress that changes the dynamics of the propagating medium. They become mass, or gravimetric,

sensors when particles are allowed to contact the propagation medium, changing the stress on it. They become vapor sensors when a coating is applied that absorbs only specific chemical vapors. These devices work by effectively measuring the mass of the absorbed vapor. If the coating absorbs specific biological chemicals in liquids, the detector becomes a biosensor. As previously noted, a wireless temperature sensor can be created by selecting the correct orientation of propagation. The propagating medium changes with temperature, affecting the output.

In all those applications, the following sensor applications are more related to our acoustic sensor research sensing for liquid and gas phases.

Mass Sensor. Of all the devices evaluated here, SAW sensors are the most sensitive to mass loads. This opens up several applications including particulate sensors and film thickness sensors. If the sensor is coated with an adhesive substance, it becomes a particulate sensor; any particle landing on the surface will remain there and perturb the wave propagation. A mass resolution of 3 pg for a 200 MHz ST-cut quartz SAW has been reported, which was 1000 times more sensitive than the 10 MHz TSM resonator tested [38]. Particulate sensors are used in cleanrooms, air quality monitors, and atmospheric monitors. Thickness sensors operate on basically the same principle as particulate sensors, except that they are not coated. The measured frequency shift is proportional to the mass of the deposited film, so the sensor provides thickness data by measuring the film density and acoustic impedance. This method is accurate, provided that the film is thin (ideally no more than a few percent of the acoustic wavelength). Most commercially available thickness sensors are based on TSM resonators. Although not so sensitive as SAW sensors, these devices offer ease of use and adequate sensitivity.

Dew Point/Humidity Sensor. If a SAW sensor is temperature controlled and exposed to the ambient atmosphere, water will condense on it at the dew point temperature, making it an effective dew point sensor. Current commercial instruments for high-precision dew point measurements are based on optical techniques, which have cost, contamination, accuracy, sensitivity, and long-term stability issues. A 50 MHz YZ-cut lithium niobate SAW dew point sensor has been developed that is immune to common contaminants, has a resolution of $\pm 0.025^{\circ}\text{C}$ (vs. $\pm 0.2^{\circ}\text{C}$ for an optical sensor), is low cost, and is significantly more stable [39]. Acoustic wave sensors with an elastic hygroscopic polymer coating make excellent humidity detectors. Three operational mechanisms contribute to the sensors' response: mass loading, acoustoelectric effects, and viscoelastic effects, each of which can be effectively controlled to yield an accurate, low-cost, humidity sensor. A 50 MHz YZ-cut lithium niobate SAW sensor coated with polyXIO has been demonstrated as a humidity sensor with a range of 0%–100% RH and a hysteresis on the order of 5% [40]. In addition, a 767 MHz AT-cut quartz SH-SAW sensor coated with a plasma-modified hexamethyldisiloxane (HMDSO) has recently been demonstrated as a humidity sensor, with a sensitivity of 1.4 ppm/% RH and a 5% hysteresis. This was found to be 4×10^3 more sensitive than a 14 MHz TSM resonator coated with the same polymer [41]. In the same category, a 434 MHz YZ-cut lithium niobate SAW sensor has been used as a remote water sensor [42], and an 86 MHz XY-cut quartz Love Wave sensor has been demonstrated as an ice sensor [43].

Vapor Chemical Sensor. Chemical vapor sensors based on SAW devices were first reported in 1979 [44]. Most of them rely on the mass sensitivity of the detector, in conjunction with a chemically selective coating that absorbs the vapors of interest and

results in an increased mass loading of the device. As with the temperature-compensated pressure sensors, one SAW is used as a reference, effectively minimizing the effects of temperature variations.

Several design considerations must be satisfied when selecting and applying the chemically sorptive coating. Ideally, the coating is completely reversible, meaning that it will absorb and then completely desorb the vapor when purged with clean air. The rate at which the coating absorbs and desorbs should be fairly quick, <1 s, for instance. The coating should be robust enough to withstand corrosive vapors. It should be selective, absorbing only very specific vapors while rejecting others. The coating must operate over a realistic temperature range. It should be stable, reproducible, and sensitive. And finally, its thickness and uniformity are very important.

When several SAW sensors, each with a unique chemically specific coating, are configured as an array, each will have a different output when exposed to a given vapor. Pattern recognition software allows a diverse list of volatile organic compounds thus to be detected and identified, yielding a very powerful chemical analyzer.

TSM resonators have also successfully been used for chemical vapor sensing [45] but they are significantly less sensitive than their SAW counterparts. In addition, SAW chemical vapor sensors have been made without coatings. This method uses a gas chromatograph column to separate the chemical vapor components, and a temperature-controlled SAW that condenses the vapor and measures the corresponding mass loading [46].

Biosensor. Similar to chemical vapor sensors, biosensors detect chemicals, but in liquids rather than vapors. As noted earlier, the SAW device is a poor choice for this

application, as the vertical component of the propagating wave will be suppressed by the liquid. Biosensors have been fabricated using the TSM resonator, SH-APM, and SH-SAW sensors. Of all the known acoustic sensors for liquid sensing, the Love wave sensor, a special class of the shear-horizontal SAW, has the highest sensitivity [47]. To make a Love wave sensor, a waveguide coating is placed on a SH-SAW device such that the energy of the shear horizontal waves is focused in that coating. A biorecognition coating is then placed on the waveguide coating, forming the complete biosensor. Successful detection of anti-goat IgG in the concentration range of 3×10^{-8} to 10^{-6} moles using a 110 MHz YZ-cut SH-SAW with a polymer Love wave guide coating has been achieved [48].

Conclusion

Acoustic wave sensors are extremely versatile devices that are just beginning to realize their commercial potential. They are competitively priced, inherently rugged, very sensitive, and intrinsically reliable, and can be interrogated passively and wirelessly. Wireless sensors are beneficial when monitoring parameters on moving objects, such as tire pressure on cars or torque on shafts. Sensors that require no operating power are highly desirable for remote monitoring of chemical vapors, moisture, and temperature. Other applications include measuring force, acceleration, shock, angular rate, viscosity, displacement, and flow, in addition to film characterization. The sensors also have an acoustoelectric sensitivity, allowing the detection of pH levels, ionic contaminants, and electric fields. Surface acoustic wave sensors have proved to be the most sensitive in general as a result of their larger energy density on the surface. For liquid sensing, a special class of shear-horizontal surface acoustic wave sensors called Love wave sensors

proved to be the most sensitive. Much work is continuing in developing these sensors for future applications.

2.4. ZnO Material for Biosensors

2.4.1. ZnO Acoustic Wave Sensors

In conventional biosensors, after analyte-receptor reaction, a complicated radioisotope or fluorescent label procedure and sophisticated detection equipment are used. These disadvantages prevent the biosensor from becoming mobile, cost efficient and mass production as most of the electronics sensors. SAW biosensors have provided certain unique advantages over other biosensor technologies, namely, higher sensitivity than electrical and thermal biosensors [49-51], and being more cost-effective and mobile than optical biosensors [52]. However, at present, SAW devices are not widely used for biological sensing, as such biosensors require highly effective immobilization of different biocomponents [9].

ZnO is a well-known piezoelectric material, which is also a wide bandgap semiconductor. It has been widely used in SAW and BAW devices in communications applications. ZnO SAW sensors have been demonstrated for toxic and combustible gas sensing [53], as well as organic gas molecules [54]. These sensors simultaneously used acoustic and electrical detection mechanisms, resulting in increased accuracy and sensitivity.

2.4.2. ZnO Nanostructures

Nanoscale structures have many unique features for biosensor applications. The emergence of nanoscale science and technology in recent years is making a significant impact on sensors. Novel nanoscale sensors show great promise, as they have faster

response and higher sensitivity than the planar sensor configurations, due to their smaller dimensions combined with dramatically increased sensing surface and strong binding properties. They can greatly enhance the sensitivity of biological sensors because the depletion and accumulation of carriers upon adsorption occurs in the “bulk” of the nano-scale structure, as opposed to the surface of a planar device. Therefore, they greatly increase sensitivity to the point where single-molecule detection becomes possible. A boron-doped silicon nanowire sensor modified by biotin is capable of detecting streptavidin binding at concentrations as low as 10 pM [55]. Nanosensors can therefore monitor the concentration of a target protein in real time, even in the case of reversible binding, thus opening up important applications in biochemical research [55]. Furthermore, the small size of these nanosensors and the recent development in their assembly technology make it possible to generate dense nanosensor arrays for biological analyses [56].

Recently, there have been a number of reports on ZnO nanostructures[57-59]. ZnO nanostructures made by MOCVD are grown at relatively low temperatures, giving ZnO a unique advantage over other wide bandgap semiconductors, such as GaN and SiC nanowires. Catalyst-free growth of ZnO nanotips by MOCVD leads to superior optical properties, as these nanotips exhibit free excitonic emission both at 10K and room temperature [60, 61]. The electrical conductivity of these nanostructures can also be controlled by in-situ doping during growth [61]. MOCVD growth can also provide atomically sharp interface control, and possible end-facet morphology control for various device applications by altering the growth conditions, without the presence of a metal catalyst.

ZnO nanorod growth on c-plane sapphire using the MOCVD growth technique was reported. The distribution of nanorods was found to be dense and uniform as observed from SEM. XRD results suggested that the nanorods had c-axis orientation. The nanorods were reported to be satisfying an epitaxial relationship with c-sapphire [62]. Physical vapor deposition (PVD) growth of ZnO nanowires has also been reported [63]. The nanowires were collected on a copper collector. The average diameter of the nanowires reported to be 60nm with a length of about a few micrometers. The SEM pictures reveal a random distribution of ZnO nanowires. The selected area diffraction shows the single crystal quality. The proposed mechanism for growth was the Vapor-Liquid-Solid (VLS) mechanism.

ZnO nanostructures have been reported to exhibit good optical properties. Photoluminescence measurements reported bound-exciton peaks at 3.359, 3.360, 3.364 eV, and free-exciton peak at 3.376eV at 10K. The full width half maximum reported was very low. The intense and sharp peak confirmed the good optical properties of ZnO nanotips. Very low intensity of deep level emission was reported at 2.28eV. This suggested that ZnO nanotips had less structural defects than films [60]. The transmission spectra showed strong UV absorption edge at ~380-387nm, and the bandgap was reported to be ~3.22eV [64, 65].

2.4.3. ZnO Electrochemical Sensors and Optical Sensors

ZnO nanostructures have been used in some electrochemical based sensors. A glucose biosensor based on glucose oxidase (GOx) immobilized on ZnO nanorod array grown by hydrothermal decomposition has been reported [66]. In a phosphate buffer solution with a pH value of 7.4, negatively charged GOx was immobilized on positively

charged ZnO nanorods through electrostatic interaction. At an applied potential of +0.8 V versus Ag/AgCl reference electrode, ZnO nanorods based biosensor presented a high and reproducible sensitivity of $23.1 \mu\text{A cm}^{-2} \text{ mM}^{-1}$ with a response time of less than 5 s. The biosensor shows a linear range from 0.01 to 3.45 mM and an experiment limit of detection of 0.01 mM. An apparent Michaelis-Menten constant of 2.9 mM shows a high affinity between glucose and GOx immobilized on ZnO nanorods.

A reagentless uric acid (UA) biosensor based on uricase immobilized on ZnO nanorods was developed by F. Zhang [67]. The ZnO nanorods derived electrode retained the enzyme bioactivity and could enhance the electron transfer between the enzyme and the electrode. This sensor showed a high thermal stability up to 85 °C and an electrocatalytic activity to the oxidation of uric acid without the presence of an electron mediator. The electrocatalytic response showed a linear dependence on the uric acid concentration ranging from 5.0×10^{-6} to $1.0 \times 10^{-3} \text{ mol L}^{-1}$ with a detection limit of $2.0 \times 10^{-6} \text{ mol L}^{-1}$ at 3σ . The apparent K_m^{app} value for the uric acid sensor was estimated to be 0.238 mM, showing a high affinity.

ZnO nanostructures have also been reported to be excellent platforms for optical sensing. A. Dorfman has reported that engineered nanoscale zinc oxide structures can significantly enhance the detection capability of biomolecular fluorescence [68]. Without any chemical or biological amplification processes, nanoscale zinc oxide platforms enabled increased fluorescence detection of these biomolecules when compared to other commonly used substrates such as glass, quartz, polymer, and silicon. The use of zinc oxide nanorods as fluorescence enhancing substrates in their biomolecular detection permitted sub-picomolar and attomolar detection sensitivity of

proteins and DNA, respectively, when using a conventional fluorescence microscope. This ultrasensitive detection was due to the presence of ZnO nanomaterials which contributed greatly to the increased signal-to-noise ratio of biomolecular fluorescence. The easy integration potential of zinc oxide nanorods into periodically patterned nanoplateforms promotes the assembly and fabrication of these materials into multiplexed, high-throughput, optical sensor arrays. These zinc oxide nanoplateforms will be extremely beneficial in accomplishing highly sensitive and specific detection of biological samples involving nucleic acids, proteins and cells, particularly under detection environments involving extremely small sample volumes of ultratrace-level concentrations. This interesting property also make multifunctional and multimode ZnO nanostructure based biosensor possible.

2.5. Summary

This chapter reviewed the existing biosensor technology, the principle and applications of SAW sensor and QCM sensor, the basic properties of ZnO nanostructure and its applications. With nanostructure, ZnO shows some exceptional properties, which gives ZnO unique advantages in sensor applications. Unlike some traditional sensing material, the study of ZnO nanostructures for sensing is still at its early stage. Further investigations have been conducted to integrate ZnO nanostructure into the traditional sensor platform, such as SAW and BAW, to create a brand new sensor technology. The following part of this dissertation will focus on achieving high quality ZnO nanostructures, integrating the sensing material with sensor platform and realizing SAW and QCM biosensors based on epitaxial ZnO nanostructures.

Chapter III. Properties of ZnO Nanotips Grown on Various Substrates

3.1 MOCVD Growth

Chemical Vapor Deposition (CVD) is defined as the formation of a nonvolatile solid film on a substrate by the reaction of vapor-phase chemicals (reactants) that contain the required constituents. Most elements can be converted to chemical vapors by reaction with functional groups (CH_3 , C_2H_5 , etc.) that have only one dangling bond. The resulting molecules ($((\text{C}_2\text{H}_5)_2\text{Zn}$, etc.) known as metalorganics, do not chemically bond to each other and hence have a high vapor pressure. In MOCVD, one or more of the reactants is a metalorganic compound. An advantage of using metalorganics instead of metal vapors is that they do not condense on the chamber walls at room temperatures. Moreover, while direct condensation is the growth method when using metal vapors, in MOCVD the reactants adsorb on the substrate surface and chemically react with one another. Thus additional control of the growth process is possible through the chemical interactions amongst the sources as well as due to interaction between the sources and the substrate.

A diagram of the MOCVD system used for ZnO film and nanostructure growth is shown in Figure 3.1. An IBM-compatible PC with data acquisition (DAQ) boards is used to control and monitor the mass flow controllers (MFC) and pneumatic valves, and to maintain temperature and pressure in the reactor and the gas lines. N_2 is used as the carrier gas, which is introduced into the MOCVD reactor from the top. The metalorganic vapors are transported into the reactor using ultrahigh purity argon. High purity O_2 is introduced into a growth chamber through a separate line. The MOCVD chamber is an

axis-symmetric rotating-disk vertical flow reactor. It consists of a horizontally placed wafer susceptor, which is rotated at high speeds and is heated by a resistive heater placed below the susceptor. Gases flow from the top and exit through an exhaust at the bottom.

ZnO nanotips and film growth was carried out in this vertical flow, rotating disk MOCVD reactor. Diethylzinc (DEZn) and ultra high purity (99.999%) oxygen gas were used as the Zn metalorganic source and oxidizer, respectively. Ultra high purity (99.999%) argon was used as the carrier gas. The typical growth temperature of ZnO nanotips was in the range of 400 - 500°C, at a rate of 1-2 $\mu\text{m}/\text{hour}$. Details of the ZnO nanotip growth using MOCVD were described previously [58]. ZnO nanotips with controlled size and shape were grown on various substrates, such as Si, c-sapphire, and glass. For the comparative study, ZnO epitaxial films were also grown on r-sapphire substrates using MOCVD. The thicknesses of all the samples used in this work range from 500 - 1,000 nm.

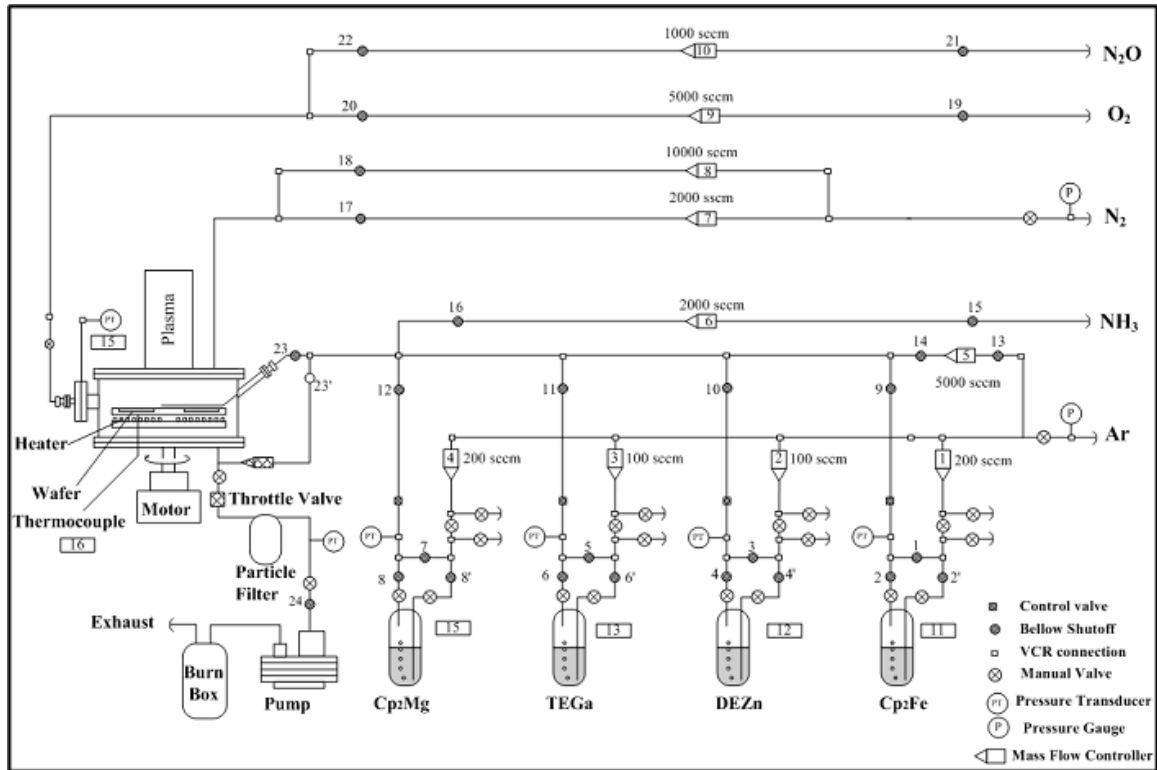


Fig. 3.1 A diagram of the MOCVD system used for ZnO film and nanostructure growth.

3.2 Characterizations of ZnO Nanotips and Films

3.2.1 Structural Characterizations

Instead of growing on a crystalline substrate with epitaxial relationship, ZnO nuclei can also be formed randomly on amorphous substrate such as SiO₂. Structurally, ZnO has three types of fast growth directions: $[2\bar{1}\bar{1}0]$, $[\bar{1}\bar{1}20]$ and $[0001]$, among which $[0001]$ direction has fastest growth rate compared to the lateral direction, ZnO nanostructures can be grown on amorphous substrates with preferred $[0001]$ orientation. The ZnO nanostructures were grown in the similar conditions using the same system. Figure 3.2 shows the θ - 2θ scan of x-ray diffraction pattern of MOCVD grown ZnO

nanotips on (a) SiO_2 /Quartz substrate, and (b) glass substrate. The XRD pattern of the as-grown sample on SiO_2 /Quartz substrate shows strong (002) and (004) ZnO double peaks, and, (101) and (202) peaks from quartz substrate, while on glass substrate only (002) and (004) ZnO double peaks were observed. As shown in the figure, our ZnO nanotips have a preferred c-axis (001) orientation even grown on an amorphous SiO_2 template. Figure 3.3 shows the field enhanced SEM image of the MOCVD grown ZnO nanotips on (a) SiO_2 /Quartz substrate, and (b) glass substrate. The as-grown ZnO nanotips are about 500 nm in height, 40-60 nm in width. The optical properties of as-grown ZnO nanotips will be illustrated in the following sections comparing with as-implanted and as-annealed samples. The results indicate that before doping the ZnO nanostructures have good morphology and crystallinity.

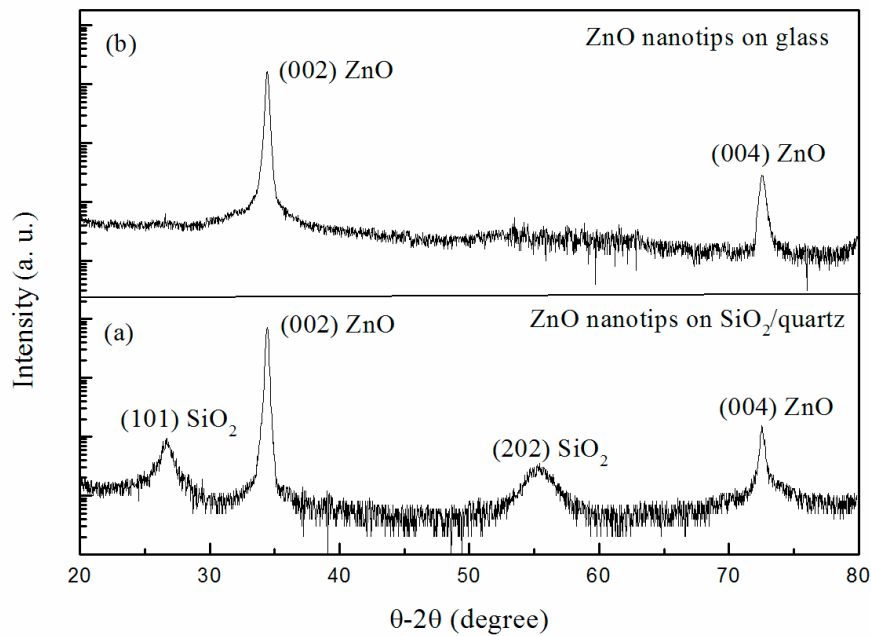


Fig 3.2 The θ - 2θ scan of x-ray diffraction pattern of MOCVD grown ZnO nanotips on (a) SiO_2 /Quartz substrate, and (b) glass substrate.

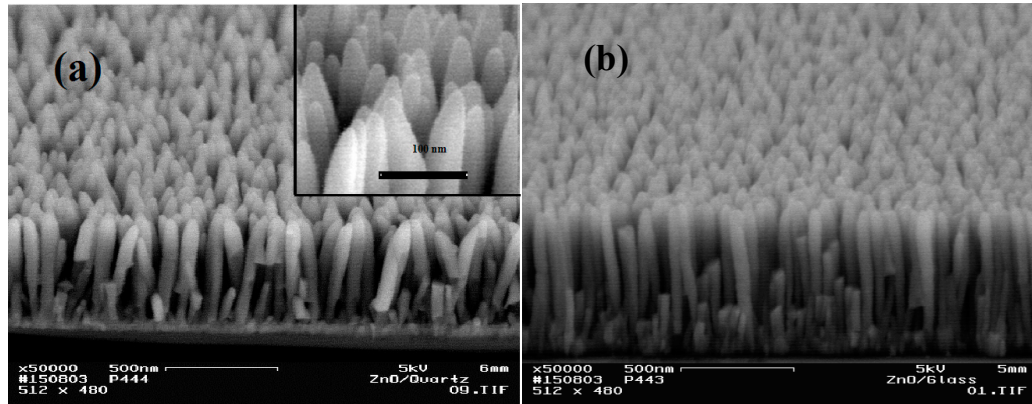


Fig 3.3 The field enhanced SEM image of the MOCVD grown ZnO nanotips on (a) SiO₂/Quartz substrate, and (b) glass substrate.

In order to compare the material properties and device performance, high quality undoped ZnO films are required. ZnO films have been grown on r-sapphire substrates using a rotating disk vertical MOCVD system. The metalorganic source for Zn is Diethyl Zinc (DEZn). The Zn vapor is introduced into the chamber, onto the rotating substrate, using a carrier gas flowing through the bubblers. The oxidizer O₂ is introduced into the chamber through separate line to avoid the gas phase reaction before deposition. Figure 3.4 shows the field enhanced SEM image of the MOCVD grown ZnO film on R-Sapphire, the film show dense and smooth surface. Figure 3.5 shows the θ -2 θ scan of x-ray diffraction pattern of MOCVD grown ZnO film on r-Sapphire with full width half maximum (FWHM) 0.12 degree. The epitaxial relationships between ZnO and r-plane sapphire were determined to be $(11\bar{2}0)$ ZnO \parallel $(01\bar{1}2)$ Al₂O₃, and (0001) ZnO \parallel $(01\bar{1}1)$ Al₂O₃.

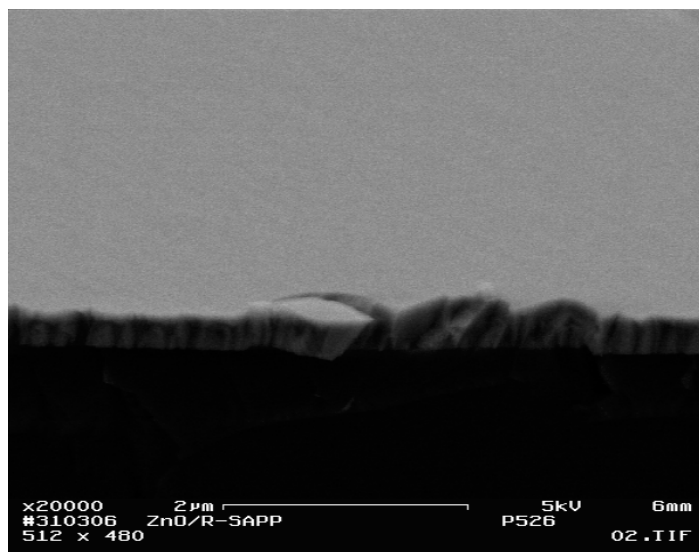


Fig 3.4 A field enhanced SEM image of ZnO film on r-sapphire.

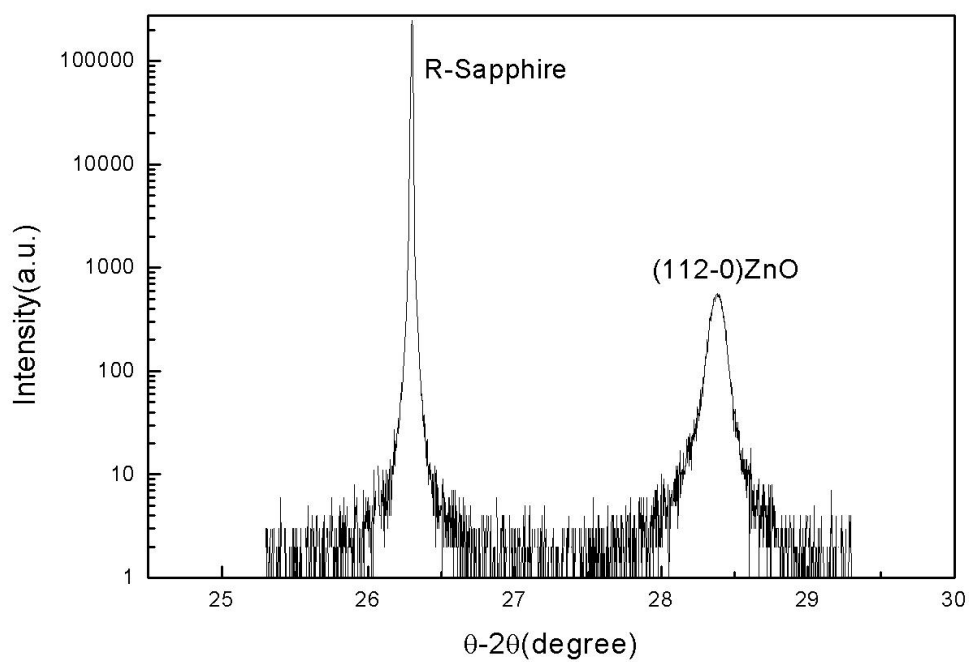


Fig 3.5 The θ -2 θ scan X-ray diffraction grown ZnO film on r-sapphire.

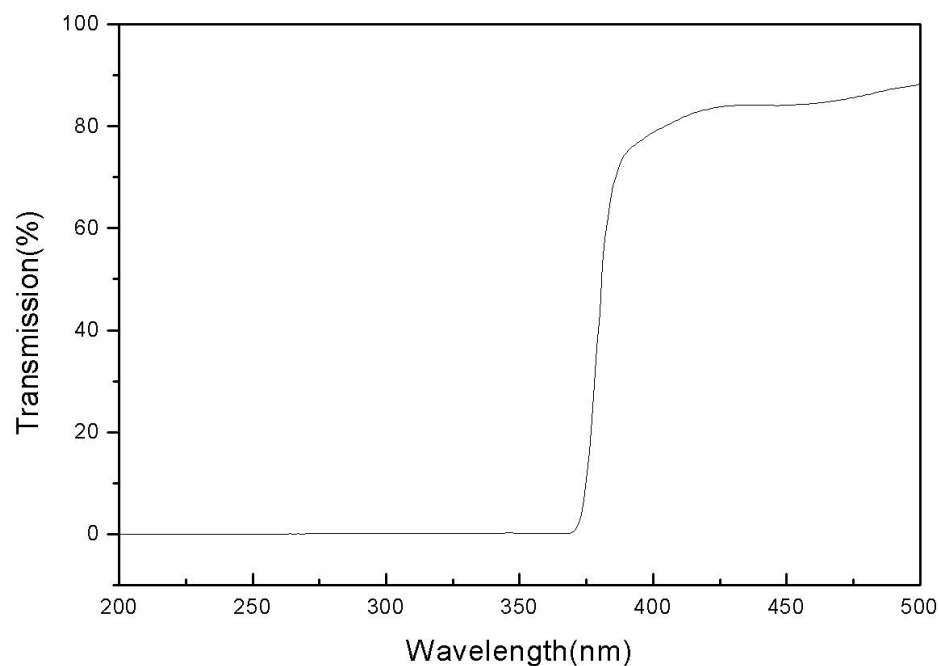


Fig 3.6 The transmission of ZnO film on r-sapphire

3.2.2 Optical Characterizations

Figure 3.6 shows the transmission of the MOCVD grown ZnO film on r-Sapphire, it shows the film has good optical properties with cutoff wavelength at ~ 375 nm. Photoluminescence (PL) spectrum was measured by using the 325nm line of a He-Cd laser of. A very strong PL peak is observed at 3.28eV, with peak intensity tens of times stronger than that obtained from ZnO epi-layers. The intense and sharp (FWHM ~ 120 meV) intrinsic PL emission peak confirms the good optical property of the ZnO nanotips (Figure 3.7). Studies on Ga-doped ZnO nanotips by HRTEM, optical probe (PL) and scanning probe (CT-AFM) show the conductivity tailoring obtained in the single-crystalline nanotips, ranging from semiconductor to semimetal. Figure 3.7 shows the

room temperature PL spectrum of the ZnO nanotips grown on a $\text{SiO}_2/\text{LiNbO}_3$ substrate. A strong near bandedge PL peak at 3.29 eV is observed. This peak results from free-exciton recombination that is prominent in ZnO nanotips. The full width at half maximum (FWHM) of the PL spectrum is measured to be 132 meV for the ZnO nanotips. The intense and sharp peak obtained from PL emission confirms the good optical property of the ZnO nanotips. There was no peak observed at deep level emission. Deep level emission relates to the presence of structural defects and impurities in the nanotips. Thus, PL measurements confirm that the ZnO nanotips are of good structural quality of ZnO nanotips. The sharp excitonic peak and no deep level emission indicate that the ZnO nanotips are of high optical quality. The green band emission is insignificant. The as-grown ZnO nanotips show n-type semiconducting property, with a free carrier concentration of approximately 10^{17} cm^{-3} . These good optical properties enhance the feasibility of multi-functional and multi-mode devices based on ZnO nanostructure.

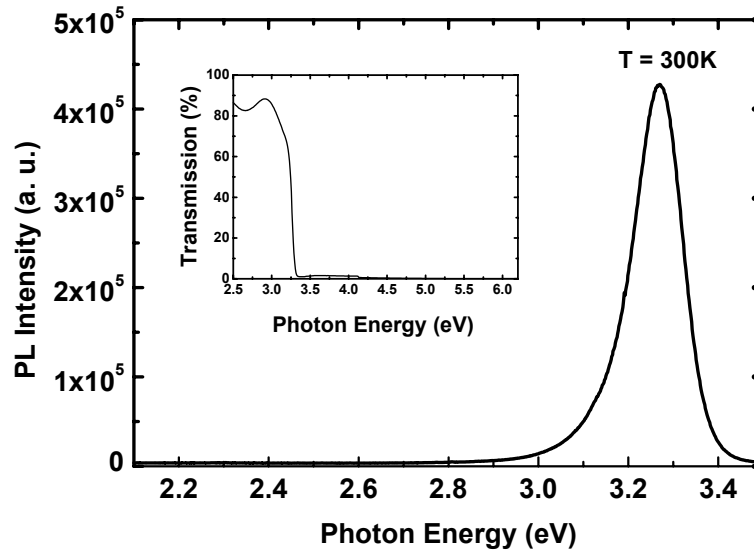


Fig 3.7 Photoluminescence spectrum of ZnO nanotips on glass; the inset shows transmission of ZnO nanotips on glass

3.3 Growth Integration of ZnO Nanotips with SAW and QCM Sensors

Lithium Niobate (LiNbO_3) is a very good candidate for piezoelectric sensor and optical sensor applications. It possesses a combination of unique electro-optical, acoustic, piezoelectric, pyroelectric and non-linear optical properties making it a suitable material for applications in acoustic, electro-optical and non-linear optical devices, high-temperature acoustic transducers, receivers-transmitters of acoustic vibrations, air force acceleration meters, acoustic wave delay lines, deflectors, generators of non-linear distorted waves, acoustic filters, electro-optical Q-modulators (Q-switch), encoders-decoders, filters in television receivers, video-recorders and decoders, converters, frequency doublers and resonators in laser systems, non-linear elements in parametric light generators, etc. An indispensable condition of some of these applications is a high degree of optical uniformity of Lithium Niobate crystals used for fabrication of active elements. Crystal growth technology by low temperature-gradient Czochralsky method allows the growth of large-size high-quality LiNbO_3 (up to 1-1.5 kg) single crystals for such non-conventional applications. It should be noted that the crystal is non-hygroscopic, colourless, water-insoluble and have low transmission losses.

Quartz is another popular piezoelectric material. A quartz crystal unit's high Q and high stiffness (small C_1) make it the primary frequency and frequency-stability determining element in a crystal oscillator. The Q values of crystal units are much higher than those attainable with other circuit elements. In general-purpose crystal units, Qs are generally in the range of 10^4 to 10^6 . A high-stability 5-MHz crystal unit's Q is typically in the range of two to three million. The intrinsic Q, limited by internal losses in the crystal, has been determined experimentally to be inversely proportional to frequency

(i.e., the Q_f product is a constant for a given resonator type). For AT- and SC-cut resonators, the maximum $Q_f = 16$ million when f is in MHz.

Quartz (which is a single-crystal form of SiO_2) has been the material of choice for stable resonators since shortly after piezoelectric crystals were first used in oscillators - in 1918. Although many other materials have been explored, none has been found to be better than quartz. Quartz is the only material known that possesses the following combination of properties:

1. It is piezoelectric and transparent.
2. Zero temperature coefficient resonators can be made when the plates are cut along the proper directions with respect to the crystallographic axes of quartz.
3. Of the zero temperature coefficient cuts, one, the SC-cut, is "stress compensated."
4. It has low intrinsic losses (i.e., quartz resonators can have high Q 's).
5. It is easy to process because it is hard but not brittle, and, under normal conditions, it has low solubility in everything except the fluoride etchants
6. It is abundant in nature.
7. It is easy to grow in large quantities, at low cost, and with relatively high purity and perfection.

A thin wafer of quartz, with electrodes attached to opposing surfaces, vibrates mechanically when voltage is applied to the two electrodes. Frequency of vibration is primarily a function of wafer dimensions. The wafers, called crystal resonators when suitably mounted with electrodes attached, have long been used for controlling frequency of radio transmitters, and it has been an essential component in telecommunication communication equipment where its piezoelectric properties are used in filters, oscillators

and other devices. Meanwhile, it is also widely used in the sensing area as a sensor template.

Although both LiNbO_3 and quartz have their unique advantages as the piezoelectric materials, it is difficult to realize a multifunctional sensor system only with these two materials. However, ZnO material can play an important role in the multifunctional sensing applications.

Hence, we make the novel ZnO nanotip- LiNbO_3 SAW (N-SAW) biosensor and ZnO nanotip-Quartz QCM (N-QCM) biosensor, which integrate ZnO nanostructures with LiNbO_3 SAW delay lines and quartz crystal microbalance, respectively. The ZnO nanotip array is used for surface modification and immobilizing the bio-receptor, while the SAW device fabricated on 128° Y-cut LiNbO_3 or the quartz crystal microbalance are used as the transducer to detect the mass loading effect resulting from the analyte-receptor reaction.

In the growth perspective, we integrate ZnO film and nanostructure with the LiNbO_3 and quartz substrates. For $\text{LiNbO}_3/\text{ZnO}$ system, different crystal lattice structures will lead to lattice mismatch and bad crystal quality. Hence, we should use a growth template, such as SiO_2 , to make it possible to grow the nanostructure and epitaxial film on the 128° Y-cut LiNbO_3 . SiO_2 layer will be grown by Plasma Enhanced Chemical Vapor Deposition (PECVD) or Sputtering. In order to reduce the insertion loss of SAW devices, the thickness of SiO_2 should be relative thin. As a good growth template, we also have the minimum requirement for the thickness of SiO_2 thin film.

The SEM pictures indicate that the nanotips are uniform in size. The bottom diameter of the nanotips range from 50 to 80nm and the height is approximately 500nm,

giving an aspect ratio ranging from 10:1 to 6:1. As seen in Figure 3.8(a), the nanotips are straight, and distributed uniformly and densely over the entire range of the substrate. In addition, these nanotips are connected at their bottom, which can be used to integrate devices with multiple nanotips. As SiO_2 is an amorphous substrate with no orientation relationship with ZnO, there is formation of random oriented nuclei, which grow after they reach a critical size. A columnar structure may then result from either competitive blocking of all crystallites (by other crystallites) whose c-axis is pointing away from the surface normal, or a preferred orientation of the ZnO nuclei on the relatively flat SiO_2 surface. For comparison, Figure 3.8(b) shows a ZnO thin film grown on the $\text{SiO}_2/\text{LiNbO}_3$ under different growth conditions. A uniform smooth film is shown on the whole surface.

X-ray diffraction (XRD) is an important nondestructive, non-contact, and highly quantitative analytical evaluation method. X-ray diffraction analysis was done to characterize the crystalline orientation of ZnO nanotips, using a Siemens D500 Thin Film x-ray diffractometer unit, mono-chromated $\text{Cu } K\alpha_1$ (1.5406\AA) radiation, with a Ni filter, and 0.15 mm slit on the detector arm.

Figure 3.9(a) shows x-ray scan of the LiNbO_3 substrate. Figure 3.9(b) shows x-ray scan of the ZnO nanotips grown on $\text{SiO}_2/\text{LiNbO}_3$ substrate. This scan was done for ZnO nanotips grown within the temperature range of $390^\circ\text{C} - 490^\circ\text{C}$ under optimized growth conditions. The scan shows a strong peak for ZnO (002) at 2θ of 34.5° , which is offset 0.1° due to instrumental error. This indicates that these nanotips are single crystal and have a preferred c-axis [0001] orientation. Figure 3.9(c) shows x-ray low angle scan to exclude the substrate, where only the ZnO (002) peak is observed, confirming the preferred c-axis orientation of the ZnO nanotips.

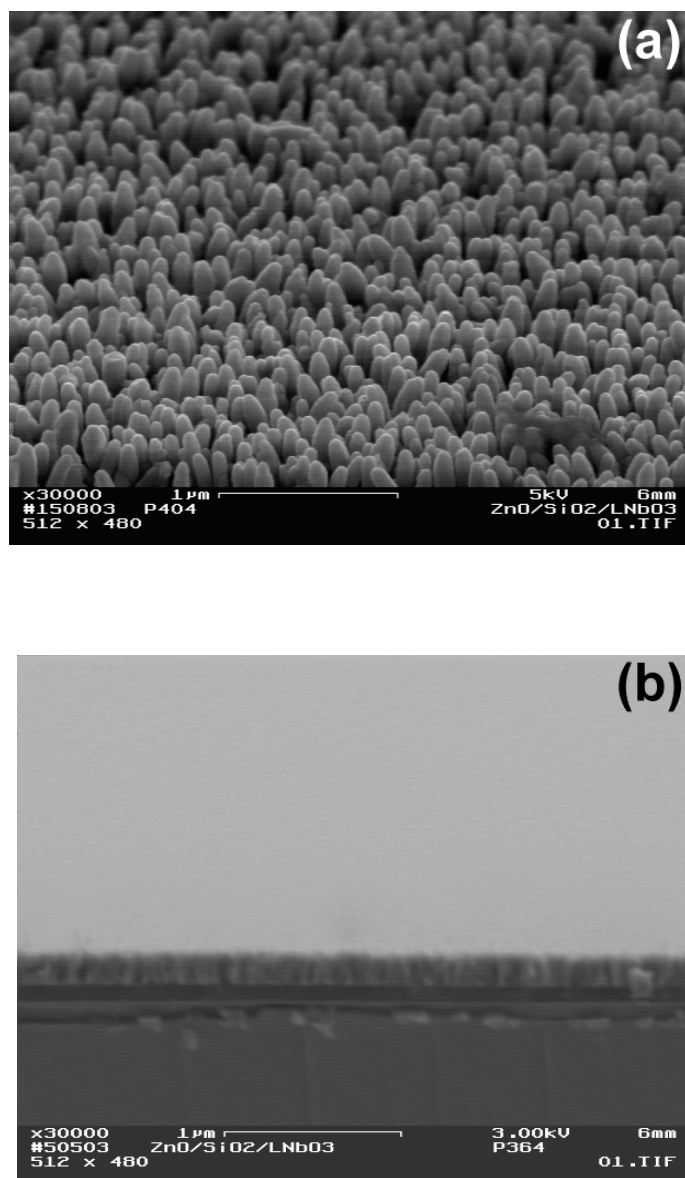
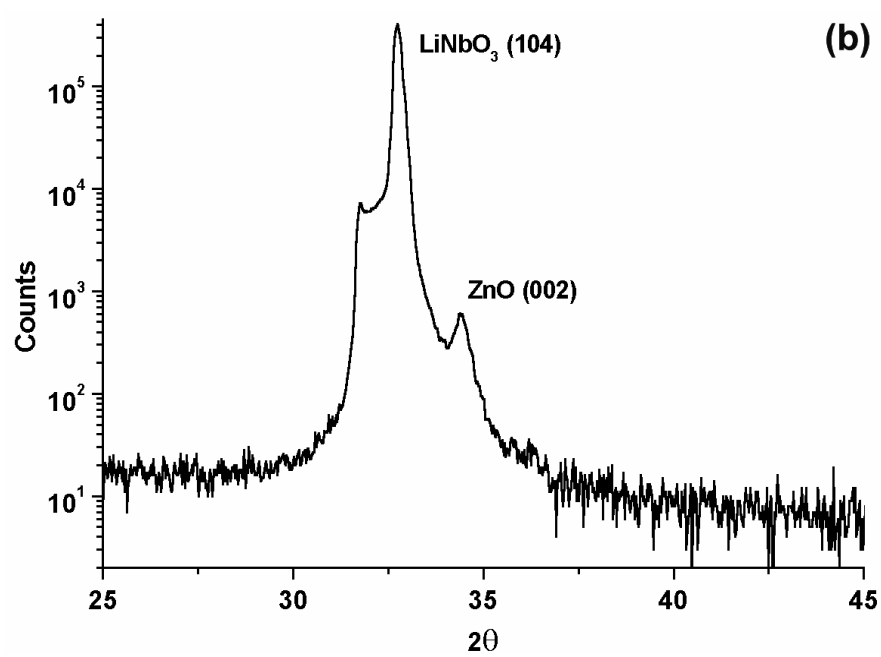
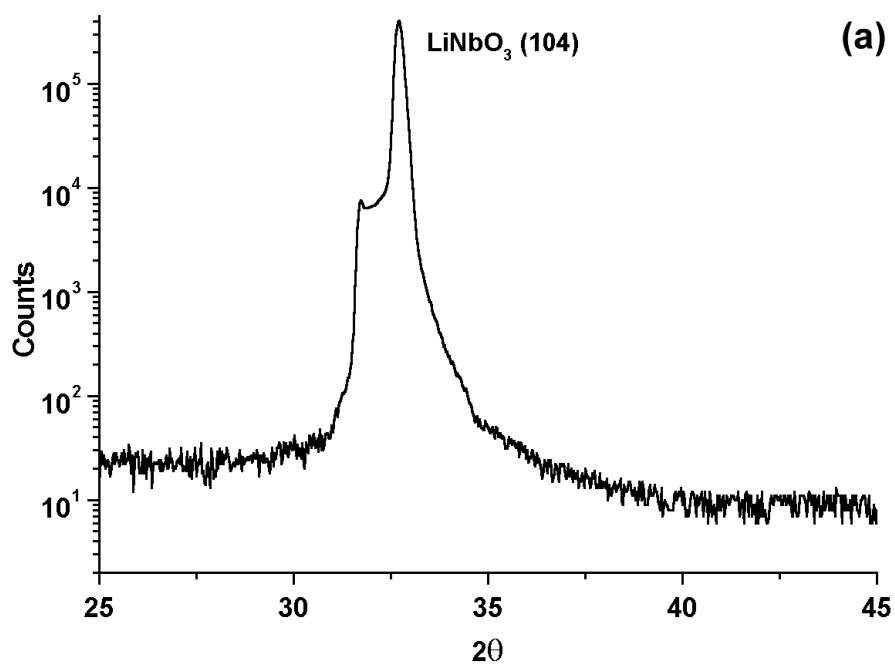


Fig. 3.8 FESEM images of (a) ZnO nanotips, and (b) ZnO film grown on SiO₂/LiNbO₃. The well-aligned nanotips have an average diameter of 75nm and height of 500nm.



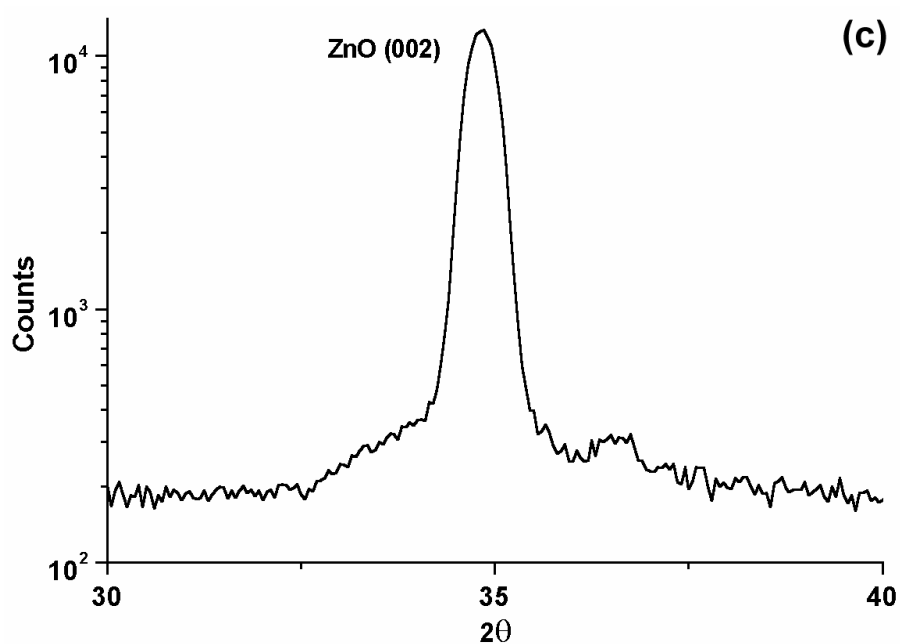


Fig. 3.9 X-ray coupled θ - 2θ scans of (a) LiNbO_3 substrate; (b) ZnO nanotips on $\text{SiO}_2/\text{LiNbO}_3$ substrate; (c) low angle X-ray scan of the ZnO nanotips, where only the (002) ZnO peak is observed, confirming the preferred c-axis orientation of the ZnO nanotips.

Photoluminescence (PL) spectrum was measured by using the 325nm line of a He-Cd laser. Figure 3.10 shows the room temperature PL spectrum of the ZnO nanotips grown on a SiO₂/LiNbO₃ substrate. A strong near bandedge PL peak at 3.29 eV is observed. This peak results from free-exciton recombination that is prominent in ZnO nanotips. The full width at half maximum (FWHM) of the PL spectrum is measured to be 132 meV for the ZnO nanotips. The intense and sharp peak obtained from PL emission confirms the good optical property of the ZnO nanotips. There was no peak observed at deep level emission. Deep level emission relates to the presence of structural defects and impurities in the nanotips. Thus, PL measurements confirm that the ZnO nanotips are of good structural quality. The sharp excitonic peak and no deep level emission indicate that the ZnO nanotips are of high optical quality. The green band emission is insignificant. The as-grown ZnO nanotips show n-type semiconducting property, with a free carrier concentration of approximately 10^{17} cm^{-3} . These good optical properties enhance the feasibility of multi-functional and multi-mode devices based on ZnO nanostructure.

For the quartz/ZnO system, ZnO nanostructure has been successfully grown on the SiO₂ epi-film and substrate (shown in section 3.2). However, according to the structure of QCM devices, the sensing surface should be on the top of the electrodes of QCM. So ZnO nanostructures need to grow on the metal (such as Au, Ti and Al) epitaxial layers. So we focus on selectively growing the ZnO/Au/Quartz system for our N-QCM biosensors using a shadow mask during the MOCVD growth.

The morphology of the ZnO nanotip array was characterized by FESEM. It was found that the nanotips are uniformly distributed and well aligned along the surface

normal to the substrate, as shown in Figure 3.11 (a). ZnO is a polar semiconductor, with (0001) planes being Zn-terminated and $(000\bar{1})$ being O-terminated. These two crystallographic planes have opposite polarity with different surface relaxation energies, resulting in a higher growth rate along the c-axis. The columnar growth of ZnO on the buffer layer composed of smaller ZnO nanocrystals is a result of a high nucleation rate before the columnar growth. The nanotips have a height of about 500 nm with a diameter of 70-80 nm at the base and around 5 nm at the tip. Transmission electron microscopy (TEM) analysis confirms the single crystalline quality of ZnO nanotips grown on various substrates. Detailed characterizations of such nanotip arrays grown on various substrates were reported previously[58].

3.5 Summary

High quality ZnO nanotips and films were grown on various substrates using the MOCVD technique, including Si, glass, quartz, c-sapphire, gold and r-sapphire. The single crystal quality of nanotip was confirmed using X-ray diffraction and scanning electron microscopy. The uniform ZnO nanotip array aligns with their c-axis perpendicular to the substrate surface. The photoluminescence spectrum of the ZnO nanotips shows strong near bandedge transition with insignificant deep level emission, confirming their good optical property. For the ZnO nanotip based SAW sensor, uniform and high quality ZnO nanotip arrays were grown and patterned on the SAW delay line using MOCVD; while for ZnO nanotip based QCM sensor, nanotips were selectively grown on the top of a gold electrode of the QCM as sensing material for biological and environmental applications.

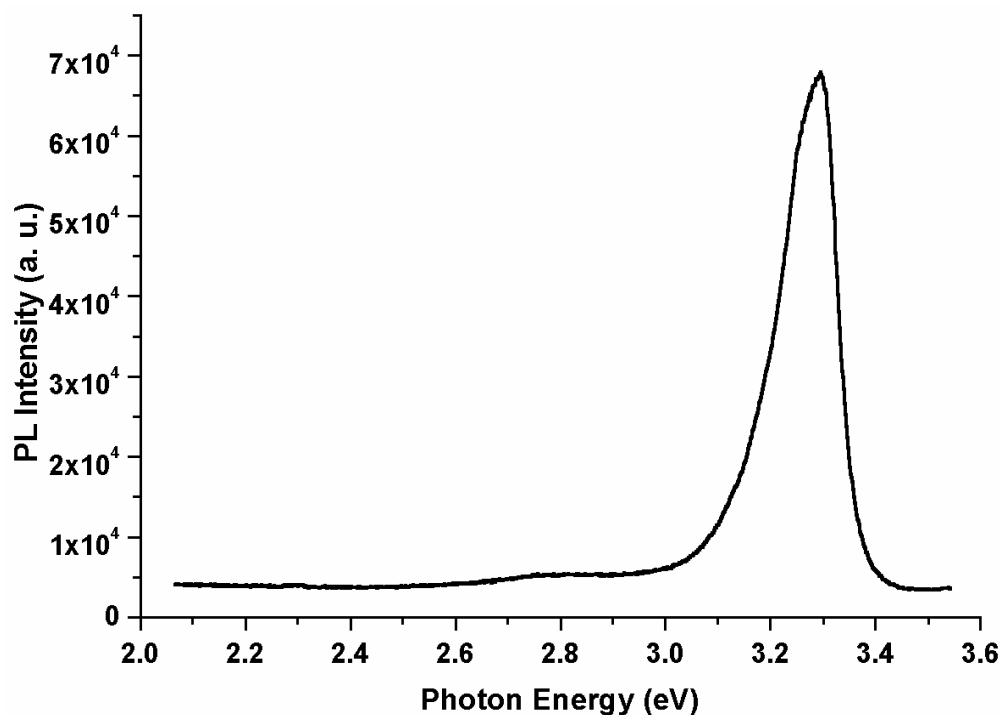


Fig 3.10 Room temperature PL spectrum of ZnO nanotips grown on a $\text{SiO}_2/\text{LiNbO}_3$ substrate. A strong near bandedge peak at 3.29 eV is observed, confirming good optical property of the ZnO nanotips.

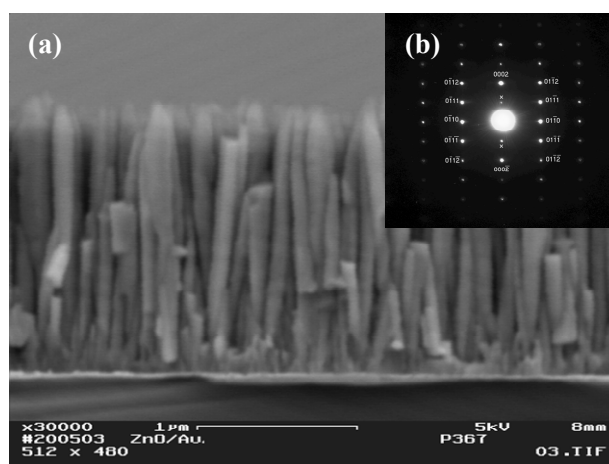


Fig 3.11 (a) SEM of ZnO nanotips on gold; (b) Selected area electron diffraction pattern from a single ZnO nanotip.

Chapter IV Surface Properties of ZnO Nanostructures

4.1. Wettability

The main method to measure wettability is the contact angle (CA). In case of a droplet of liquid on a solid it is defined as the angle θ between the surface of the solid (solid-liquid interface) and the liquid (liquid-vapor interface) (see Figure 4.1). If $\theta < 90^\circ$, a surface is called hydrophilic, if $\theta > 90^\circ$, it is called hydrophobic. To understand how this contact angle forms, let us make an energy consideration. Every surface or interface, respectively, needs a certain amount of energy to be formed. This energy can be understood, for example, by thinking about cleavage of a solid material. The energy for breaking the bonds during the cleavage minus the relaxation energy of the surface atoms is related to the absolute surface energy of the two newly created surfaces. Therefore the energy needed to form one unit area of an interface or surface, respectively, is called surface energy σ [J/m²] or surface tension γ [N/m], which is specific for each interface. σ and γ are equal only if there are no strains. A more general expression, which also considers surface strains, is the surface stress tensor [69].

$$\sigma_{ij} = \gamma \delta_{ij} + \left. \frac{\partial \gamma}{\partial \epsilon_{ij}} \right|_T \quad (4.1)$$

Here σ_{ij} is the component of the surface stress tensor, ϵ_{ij} is the component of the surface strain tensor, γ is the surface tension and T is the temperature. For the further discussion we assume that $\sigma = \gamma$ which is true for liquids and solids with small strains.

An equilibrium state is reached if the energy is minimized. Therefore if the interfacial energy of the solid-liquid interface σ_{sl} is smaller than the interfacial energy of

the solid-vapor interface σ_{sv} a liquid droplet tends to spread out and wet the surface of the solid. The other way around, if $\sigma_{sl} > \sigma_{sv}$ the liquid droplet tends to remain compact, and to form less solid-liquid interface. This can be visualized by surface tension forces that have a fixed value corresponding to the surface energy of the interface and act along the boundaries. The equilibrium state and minimum in surface free energy, respectively, are reached when all three forces caused by the surface tension along the interfaces are in equilibrium. This relation is expressed in Young's equation:

$$\sigma_{sv} = \sigma_{sl} + \sigma_{lv} \cos \theta \quad (4.2)$$

$$\cos \theta = \frac{\sigma_{sv} - \sigma_{sl}}{\sigma_{lv}} \quad (4.3)$$

Where θ is the contact angle, σ_{ij} is the surface tension or surface free energy respectively.

The indices stand for the different interfaces: solid-vapor (sv), solid-liquid (sl) and liquid-vapor (lv).

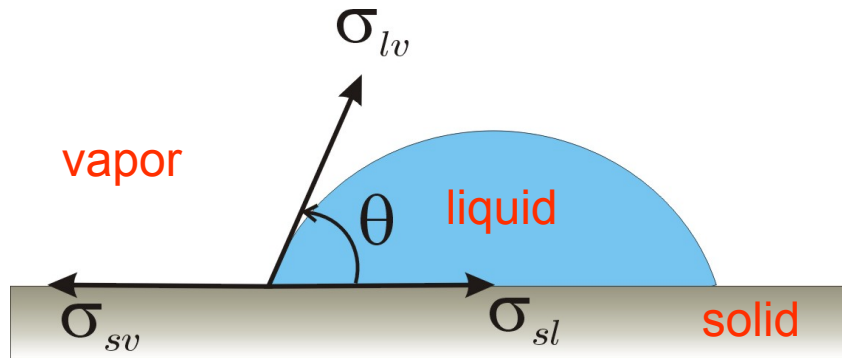


Fig 4.1 Schematic of a droplet on a homogeneous, flat surface. The arrows indicate the forces caused by the surface tensions σ_{ij} along the interfaces. The indices stand for the different interfaces solid-vapor (sv), solid-liquid (sl) and liquid-vapor (lv). θ is the contact angle between the surface of the solid and the liquid.

Young's equation is valid only for flat, smooth and chemical homogeneous surfaces. In reality this is usually not the case, therefore we have to look closer at rough surfaces. The theoretical basic principles of wetting rough surfaces were investigated by R.N. Wenzel [70]. Wenzel made the assumption that the whole surface under the drop is covered with liquid, so with respect to a smooth surface there is more actual area wetted. We can define a roughness factor r as the ratio of the area of the actual and the projected, smooth surface.

With a roughness factor r as the ratio of the actual and the projected areas (Figure 4.2), the Young's equation was modified as,

$$\cos \theta_w = r \frac{\sigma_{sv} - \sigma_{sl}}{\sigma_{lv}} = r \cos \theta_y \quad (4.4)$$

$$r = \frac{A_{true}}{A_{observed}} \quad (4.5)$$

where θ_w is the contact angle predicted by Wenzel's theory and θ_y is the contact angle from Young's equation (4.3).

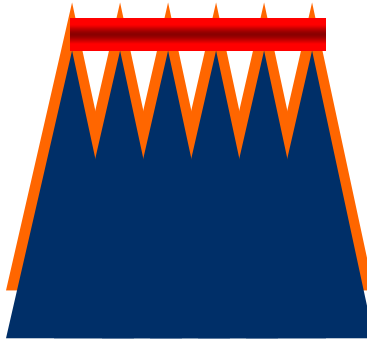


Fig. 4.2 The actual and projected (geometric) area of a rough surface

The wetting properties of the nanotips should follow the Wenzel equation (4.4), while the wetting properties of ZnO films should follow the Young's equations (4.2, 4.3).

4.2. Wettability Control on ZnO Nanostructures

Contact angle measurement

There are several ways of measuring contact angles. The most common one for measuring contact angles on flat surfaces is the sessile drop method. It is very straightforward since a drop of water or another liquid is put onto the surface to measure. Then the drop sitting on the surface is viewed from the side and the contact angle is read off either directly with the eye and a goniometer (telescope with an angular scale) or an image is captured electronically by a CCD camera and processed by image software to determine the contact angle with the aid of a computer. Figure 4.3 shows a view through the telescope of a setup for determining the CA with the eye. In order to get good contrast, to be able to clearly determine the boundaries of the drop, it is highlighted from the backside by a back-light. The indicators in the telescope are a fixed angular scale, a movable scale and a baseline. For a measurement, the base line is aligned with the intersection line of the drop and the sample in the way, that the intersection point of the drop and the sample is placed in the middle of the baseline where the movable scale intersects the baseline. To determine the CA, the movable scale is rotated until it matches the tangent of the drop and thus indicates the contact angle on the angular scale.

The setup for the computer-aided CA measurement is exactly the same but with the telescope replaced by a CCD-camera which is connected to a PC with the CA measurement software installed (see Figure 4.4). For this thesis we used a computer-

aided system. It is the Model 500 Advanced Goniometer from ram'e-hart instrument co.. The software we used is the "DROPimage Advanced Software; a program system for interfacial tension and contact angle measurement by image analysis; Advanced Edition" by Finn Knut Hansen, which was delivered with the goniometer. The program has several routines implemented for measuring contact angles, from fitting a theoretical drop profile as part of a interfacial tension calculation to pure numerical methods. The method we used is a numerical method in which a horizontal line on the screen is aligned with the solid surface of the sample. A properly aligned drop profile is then given by a filter routine. The contact angle is simply calculated by numerical derivation of the profile at the contact point of water and solid. The software always calculates the contact angles on both sides of the drop on the image and shows both values as well as the average value of them.

To study the wettability transition of ZnO materials, contact angles between the ZnO surfaces and the water droplet were measured. The following ZnO surfaces have been studied: ZnO nanotips grown on c-sapphire substrate, ZnO nanotip grown on (100) Si substrate and ZnO epitaxial film grown on r-sapphire.

Figure 4.5 (a) shows the FESEM image of ZnO nanotips grown on c-sapphire. ZnO nanotips are predominantly oriented along the c-axis with uniform size and terminated with sharp tips. The diameter at the bottom of nanotips is in the range of 40-80nm and the tip length is 500 – 1000nm, giving an aspect ratio of ~10:1. Shown in Figure 4.5 (b) is the FESEM picture of ZnO nanotips grown on (100) Si substrate. The ZnO nanotips are found to be preferably c-oriented and terminated with round tips. In

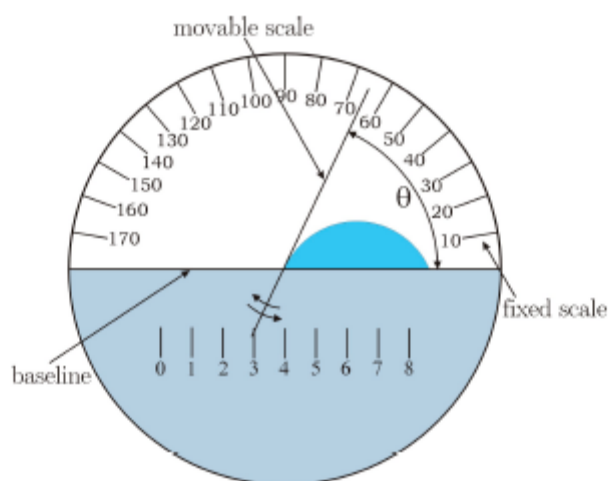


Fig 4.3: View through the telescope of a contact angle goniometer. The drop is aligned with the baseline and the intersection point of the movable scale and the baseline. For CA measurement, the movable scale is rotated until it matches the tangent to the drop and thus indicates the CA on the fixed scale.

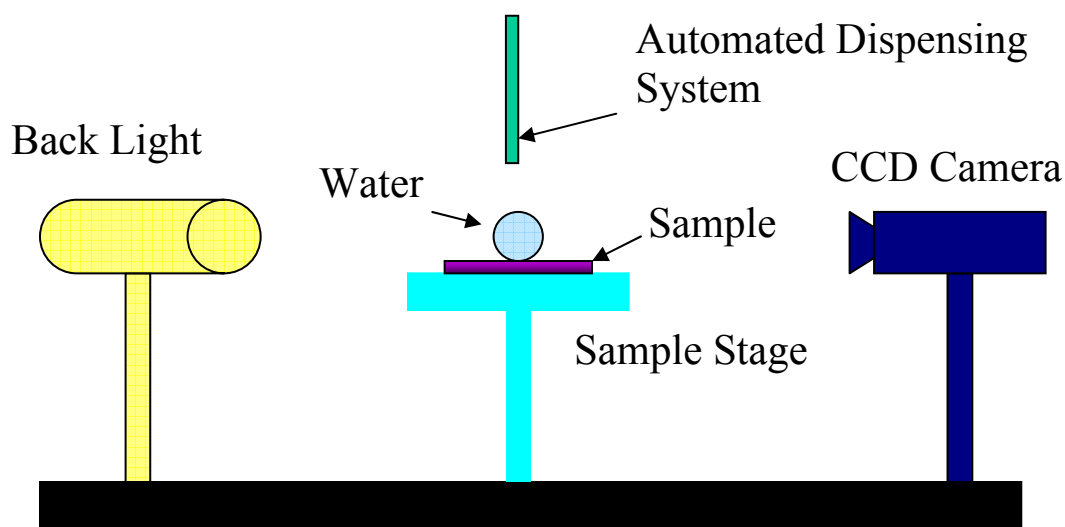


Fig 4.4 Setup for computer-aided CA measurements. The sample with the drop on it is highlighted by a back-light to provide a good image quality and contrast. The CCD-camera captures a picture from the side view and sends it to the connected PC with installed CA measurement software which processes the image and determines the contact angle. (Model 500 Advanced Goniometer from ramé-hart instrument co.)

comparison, the dense ZnO nanotip-based film has a much larger surface area than the flat ZnO film grown on $(01\bar{1}2)$ r-sapphire (Figure 4.5 (c)).

Figure 4.6 (a) shows a comparison of theta-2theta x-ray scans for ZnO nanotips grown on c-sapphire, Si and glass substrates. Absence of any other ZnO reflection apart from ZnO (0002) reflection indicates preferred c-axis orientation of the nanotips. It is found from the scans that the intensity of the (0002) ZnO reflection for nanotips grown on c-sapphire substrate is much higher compared to Si or glass substrates, while the intensities of ZnO nanotips grown on Si and glass are observed to be of the same order. Figure 4.6 (b) shows a comparative on-axis ω -rocking curve of ZnO nanotips grown on c-sapphire, Si and glass substrates. It can be seen that the full width at half maximum (FWHM) of the ZnO nanotips on c-sapphire is much smaller than that on Si or glass substrates, while FWHM for nanotips grown on Si and glass substrates are observed to be similar. ZnO and c-sapphire have the same Wurtzite crystal structures. ZnO nanotips grown on c-sapphire have in-plane registry with the substrate. In contrast, there is no such in-plane registry for ZnO nanotips grown on Si (due to presence of a thin SiO₂ interfacial layer) or on glass (amorphous) substrate. Thus, ZnO nanotips grown on c-sapphire are expected to be much better in c-axis alignment. The differences in X-ray diffraction intensity and in FWHM indicate a much better orientation of the nanotips grown on c-sapphire in comparison to Si or glass substrates. This has also been observed by FESEM images.

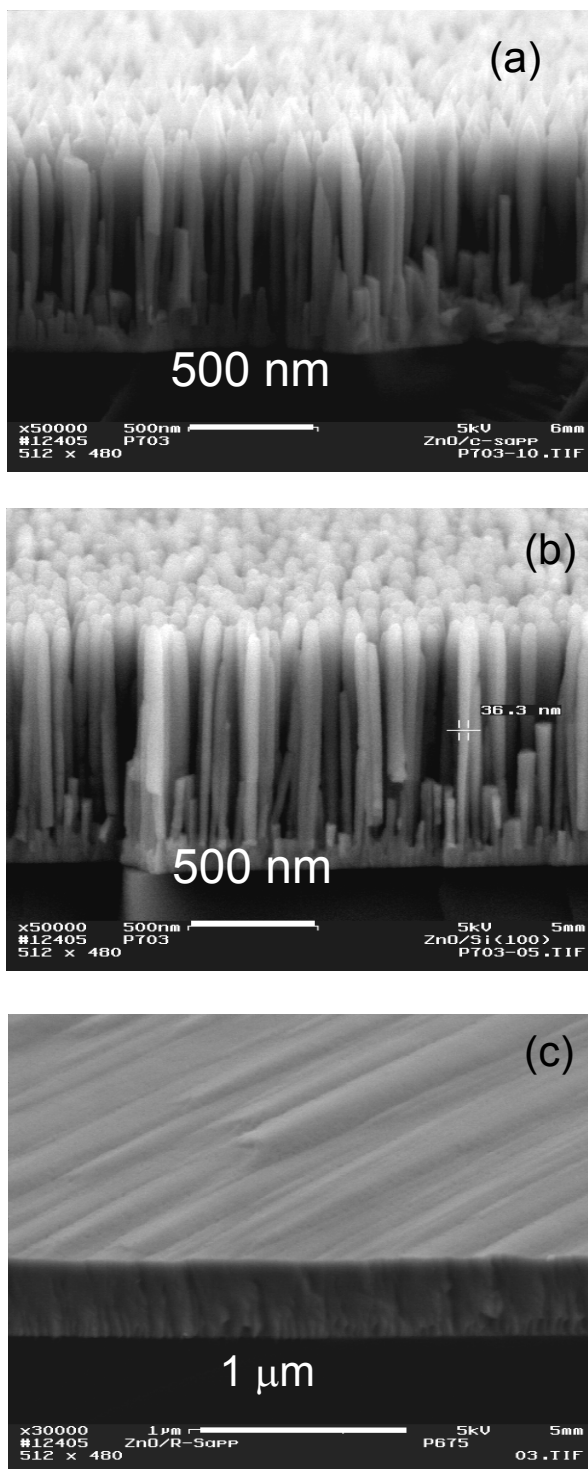


Fig 4.5 Surface morphologies of ZnO a) nanotips on c-sapphire, b) nanotips on Si, and c) film on r-sapphire, taken by field-emission scanning electron microscope (SEM)

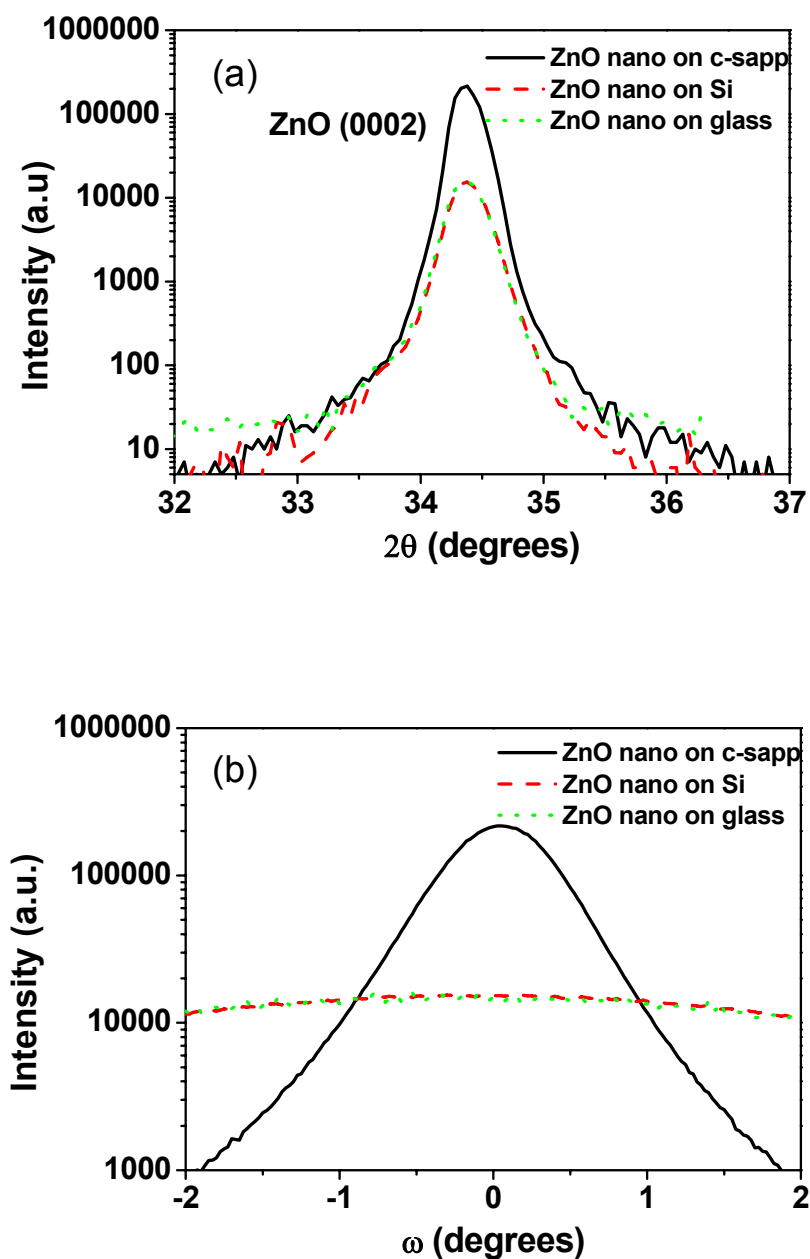


Fig 4.6 (a) Theta-2theta x-ray scans for ZnO nanotips grown on c-sapphire, Si and glass substrates. (b) A comparative on-axis ω -rocking curve of ZnO nanotips grown on c-sapphire, Si and glass substrates.

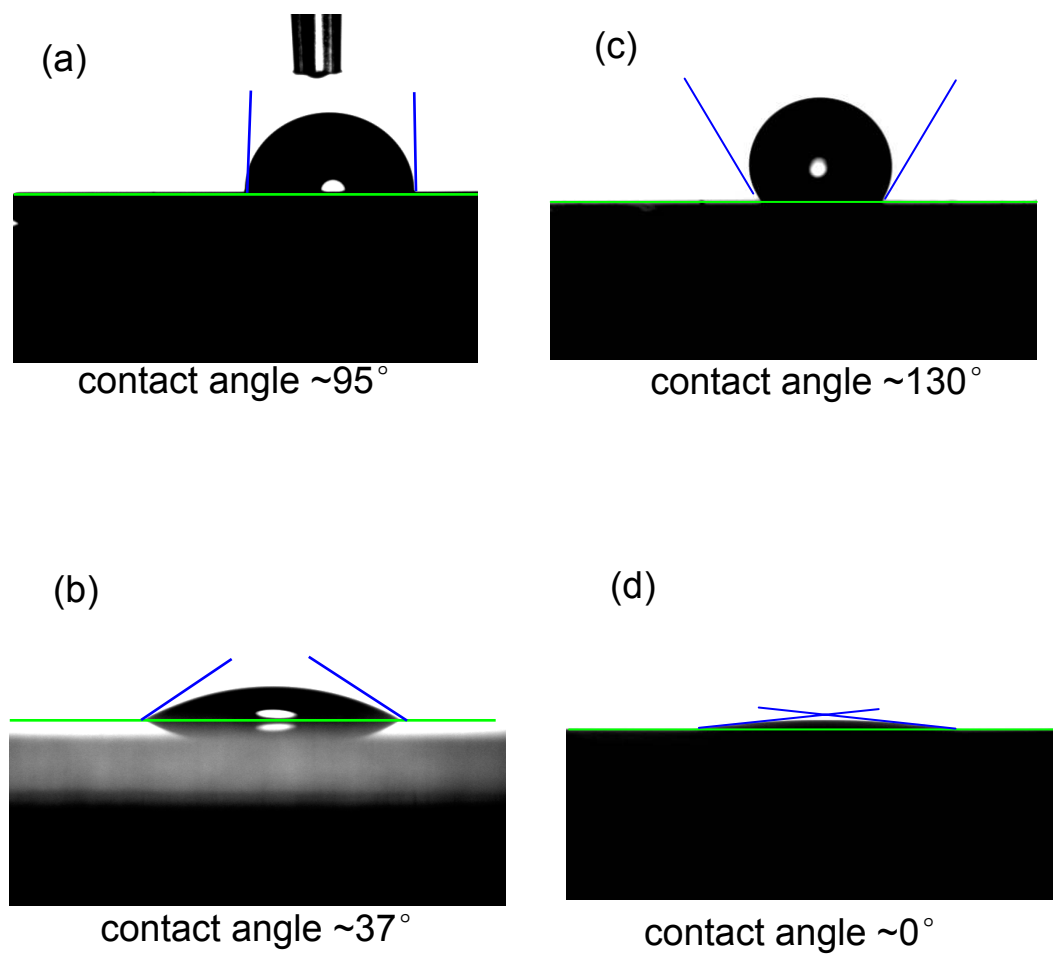


Fig 4.7 (a) Hydrophobic surface of ZnO film with contact angle (CA) $\sim 95^\circ$. (b) Hydrophilic surface of ZnO film with CA $\sim 37^\circ$. (c) Hydrophobic surface of ZnO nanotips with CA $\sim 130^\circ$. (d) Super hydrophilic surface of ZnO nanotips with CA $\sim 0^\circ$.

As described before, the contact angle measurement was conducted by means of the computer aided CA measurement system Model 500 Advanced Goniometer from ram'e-hart instrument company. For a CA measurement a small drop of DI water is put onto the sample surface via the automated dispenser system from ram'e-hart. Then an image is captured from the side view with a CCD camera and processed by an image analysis software which calculates the contact angle. The automated dispenser system is a software driven dispenser tool with which the drop volume can be precisely controlled. The usual drop volume we used was 5 μ l. The procedure for placing the drop is to approach the surface of the sample with the tip of the syringe, which is connected to the automated dispenser system. Then a drop of a defined volume (e.g. 5 μ l) is formed at the tip of the syringe by the dispenser. The syringe with the drop on its tip is now approached to the surface until the water touches it. When the contact is established, the syringe is drawn back and the drop stays on the surface, relaxing to its equilibrium shape and position. Ideally this equilibrium shape is symmetric and the CA is the same all along the contact line. In reality this is not always the case. Due to inhomogeneities of the surface the CA can vary around the contact line of the drop with the surface. To minimize the uncertainties in the CA measurements and to improve the reproducibility of the CA results, we took data only from drops of a symmetric shape and took the average value between left and right contact angle on the captured image. The values between left and right CA could still differ by about two to three degrees. Hence, although the measurement and the calculation itself is accurate to about 0.1°, the CA for a given surface can be determined only by an accuracy of $\pm 2^\circ$. Figure 4.7 shows typical images taken during CA measurements. Since these images, taken by the CCD camera of the CA

goniometer, were actually used by the software to determine the CA, the contrast is very high so that only the shape is visible and the drops are not distinguishable from the surface material.

To study the transition of ZnO nanotips from hydrophobic to superhydrophilic status, an Osram XBO 150W/4 Xe UV short arc lamp was used. Xe short arc lamp emits a spectrum close to the daylight spectrum. A bandpass filter that transmits in the wavelength range from 250 nm to 390 nm was used in order to get mostly UV radiation for the studying of wettability transition.

Directly after the growth, the fresh ZnO nanotips surface is hydrophilic with a low CA of about 10° . If stored in the dark in a nitrogen box at room temperature the CA rises slowly until it reaches a maximum value of 120° . This transition to the hydrophobic state takes one to two months to reach the maximum CA value if no special treatment is applied. If this hydrophobic ZnO nanotip surface is irradiated with UV light, the CA decreases quickly to very low values of down to under 5° , depending on the sample, irradiation time and power output of the UV lamp. This cycle: growth \rightarrow low CA \rightarrow dark storage \rightarrow high CA \rightarrow UV irradiation \rightarrow low CA \rightarrow dark storage \rightarrow high CA... is repeatable (see also Figure 4.8).

From the CA measurement results, it is found that shining the epitaxial ZnO film grown on r-sapphire shown in Figure 4.5 (c) with UV light changes the CA from 95° , corresponding to hydrophobicity (Figure 4.7 (a)) to around 37° , corresponding to hydrophilicity (Figure 4.7 (b)). In comparison, the similar UV treatment on ZnO nanotips (Figure 4.5 (a)) causes a more pronounced change: the CA decreases from 130° (Figure 4.7 (c)) to around 0° (Figure 4.7 (d)). In addition, the change in CA is reversible with

low temperature O₂ annealing. A five-cycle variation of CA on ZnO nanotips has been achieved with alternative UV illumination and O₂ annealing. The hydrophobic status of the ZnO nanotips, where CA > 120 °, and the superhydrophilic status where CA is close to 0 °, are highly repeatable after the five cycles, implying a stable change of the surface status. The ZnO nanotip morphology also changes the CA. Sharp tips in Figure 4.5 (a) give a CA variation between ~0 ° and 130 °; whereas for the nanotips with round top end in Figure 4.5 (b) only give a CA range between 10 ° to 124 °.

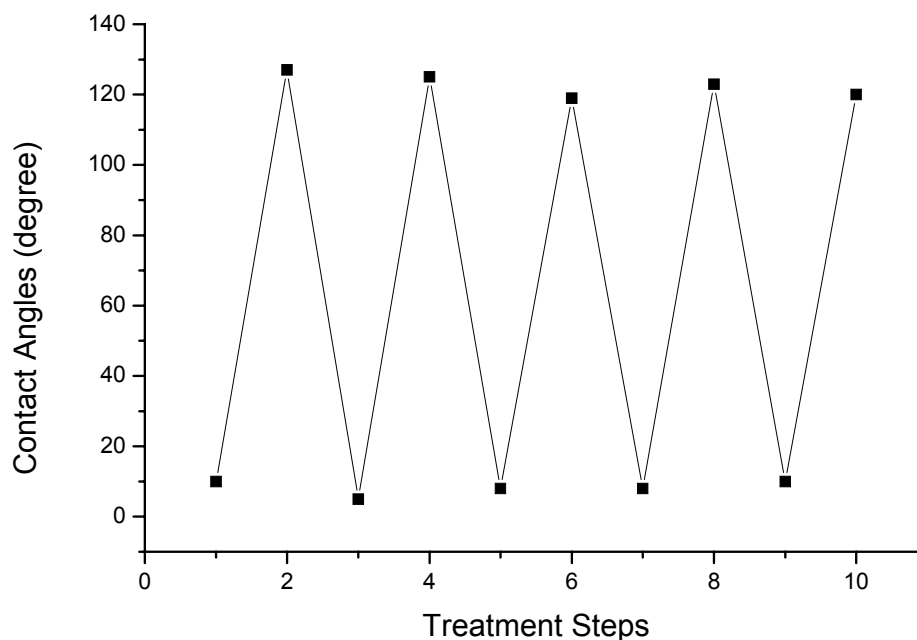


Fig 4.8 CAs at corresponding sample treatment steps in the growth → low CA → dark storage → high CA → UV irradiation → low CA → dark storage → high CA...

The larger CA range on ZnO nanotips comes from the increased surface area of the nanostructure. For a flat smooth and chemically homogeneous solid surface (ZnO film), the contact angle of a liquid droplet is defined by Young's Equation (4.3). In case of the rough surface such as ZnO nanostructured one (shown in Figure 4.5 (a)), the Young's equation is modified by R.N. Wenzel with the assumption that the whole surface under the drop is covered with liquid (4.4). r is much larger than one. Thus, the increasing in surface roughness due to the nanostructure results in a much larger CA transition range compared to the flat surface. The high hydrophilicity and high hydrophobicity of ZnO nanostructures are important in the chemical and biochemical sensor areas. For example, we have found that superhydrophilic sensing surface results in a dramatic decrease of liquid consumption on the sensing area, as well as a significant improvement of sensitivity.

We have also studied the CA transition rate, which is crucial for real device applications, particularly, for the effective control of the micro- or nano- fluid motion. The time taken for the changing from hydrophobic to hydrophilic status under UV light is measured on both ZnO nanotips and epitaxial films samples. As shown in Figure 4.9 (a), the transition time for CA to drop from 130° to 8° on ZnO nanotips (Figure 4.5(a)) only takes 4 minutes. Similarly, the UV shining takes 6 minutes to decrease CA for the nanotips with a rounded top end shown in Figure 4.5(b). The transition rates measured here is ~ 30 times faster than previously reported, where it took ~ 2 hours for the sample to change from hydrophobic to hydrophilic status¹⁴. The CA recovering rates are also plotted in Figure 4.9 (b), as measured on the same sample with O_2 annealing at $50^\circ C$.

The time takes for full CA recovery is around 17 hours on ZnO nanotips, 10 times shorter than the reported CA recovery time[71, 72].

The process can be described by equation UV irradiation generates electron-hole pairs in the ZnO surface, and some of the holes can react with lattice oxygen to form surface oxygen vacancies. Meanwhile, water and oxygen may compete to dissociatively adsorb on them. The defective sites are kinetically more favorable for hydroxyl adsorption than oxygen adsorption. Similar as TiO₂ [73, 74], the process can be described in equations (Eq. 4.6-4.8):



Hence, the surface hydrophilicity is improved, and the water CA of a relative flat ZnO surface changes from 95° to 37°. For a rough surface like nanotips, water will enter and fill the grooves of the nanostructures, leaving only the up part of the nanotips not in contact with the liquid, which is the three-dimensional capillary effect of a rough surface. This effect results in a water CA of about 0°. Namely, combining with the rough structure, the UV irradiation causes the surface wettability of aligned ZnO nanotips to change from hydrophobic status to superhydrophilic status.

It has been demonstrated that the surface becomes energetically unstable after the hydroxyl adsorption. While the oxygen adsorption is thermodynamically favored, and it is more strongly bonded on the defect sites than the hydroxyl group [73]. Therefore, the hydroxyl groups adsorbed on the defective sites can be replaced gradually by oxygen atoms when the UV-irradiated samples were placed in the oxygen ambient. Subsequently,

the surface evolves back to its state before UV illumination, and the wettability is reconverted from superhydrophilic status to hydrophobic status.

It can be concluded that the surface chemical composition provides a photosensitive surface, which can be switched between hydrophilicity and hydrophobicity, and the nanostructure further enhances these properties due to the roughness effect. Furthermore, the reversible transitions of the surface wettability of ZnO is proceeded only by the adsorption and desorption of surface hydroxyl groups at the outmost layer of oxide films [75]. The structure below the outmost layer remains stable, free from changes in chemical conditions.

Compared to other published ZnO surface stated previously, our ZnO nanotips have a much faster transition rate due to their high crystal quality, such as single crystallinity, low defects density and few surface traps.

It took about one month to change the ZnO superhydrophilic surface to the hydrophobic surface if the samples were stored in the nitrogen box. In order to reduce the transition time from low CA to high CA, we annealed the superhydrophilic samples in the controlled environmental chamber. The samples were annealed at 50 °C in three ambients: O₂, N₂ and vacuum. For the sample annealed in O₂, the CA was fully recovered to 130 ° in less than 17 hours. Increasing the temperature does not further shorten the recovery time. The samples annealed in N₂ and vacuum did not have the CA changes at all after 24 hours annealing. This result implies the oxygen adsorption is thermodynamically favored, and it is more strongly bonded on the defect sites than the hydroxyl group. The hydroxyl groups adsorbed on the defective sites can be replaced gradually by oxygen atoms when the hydrophilic samples are annealed in oxygen

ambient at low temperature. Subsequently, the surface evolves back to its original state (before UV irradiation), and the wettability is reconverted from superhydrophilicity to hydrophobicity. It was reported that at least 7 days dark storage was required for this transition on ZnO films as well as on ZnO nanostructures[71, 72]. In comparison, our results in the transition rate of ZnO nanotips show significant improvement.

4.3. Feasibility Study of Surface Functionalization on ZnO Nanostructures

In order to realize selective sensing in our biosensors, we explored the functionalization of single-crystalline ZnO nanotips through the collaboration with Prof. Galoppini's group at Chemistry Department at Newark Campus of Rutgers University. In this section, we mainly focus on the feasibility study of small molecules with functional groups that are known to form covalent bonds with metal oxides nanoparticles:[76] COOH, SH, SiOMe₃, SiCl₃, and PO(OH)₂. The structures of the compounds are shown in Figure 4.10[77] and they are all commercially available. The main objective of this work was to use simple molecules as models to determine which functional groups would bind to ZnO nanotips. In particular, we were interested in employing *bifunctional linkers*, preferably rigid, having one group that attaches to the surface while leaving a second one available for further functionalization of the nanotips. Alternatively, the surface functionalization could be done in one step by using a functionalized linker, as represented in Figure 4.11[77]. The ability to functionalize the nanotips would lead to numerous applications, for instance, new ZnO-based integrated, multimode and multifunctional sensor technology to achieve higher accuracy and selectivity than existing sensors.

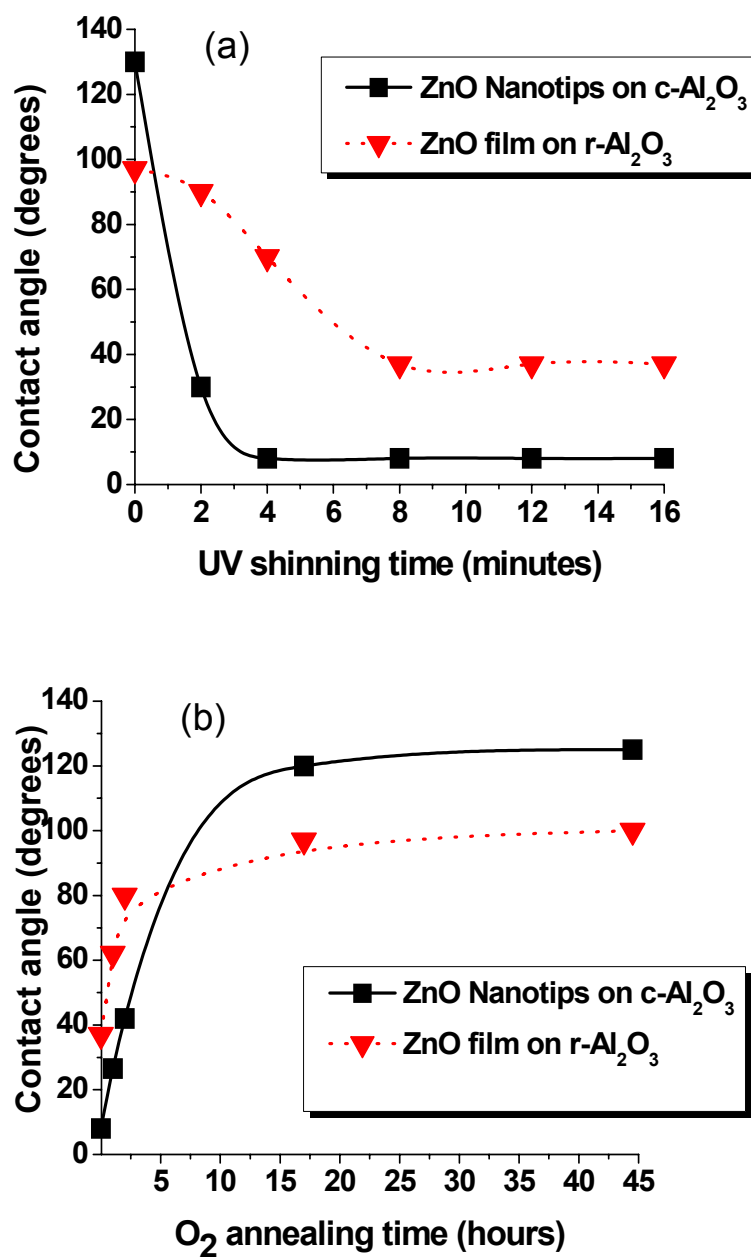


Fig 4.9 (a) Contact angle change under UV light as a function of time. The substrates are ZnO nanotips and film, respectively. b) Contact angle change under O₂ annealing at 50 °C as functions of time. The substrates are ZnO nanotips and film, respectively.

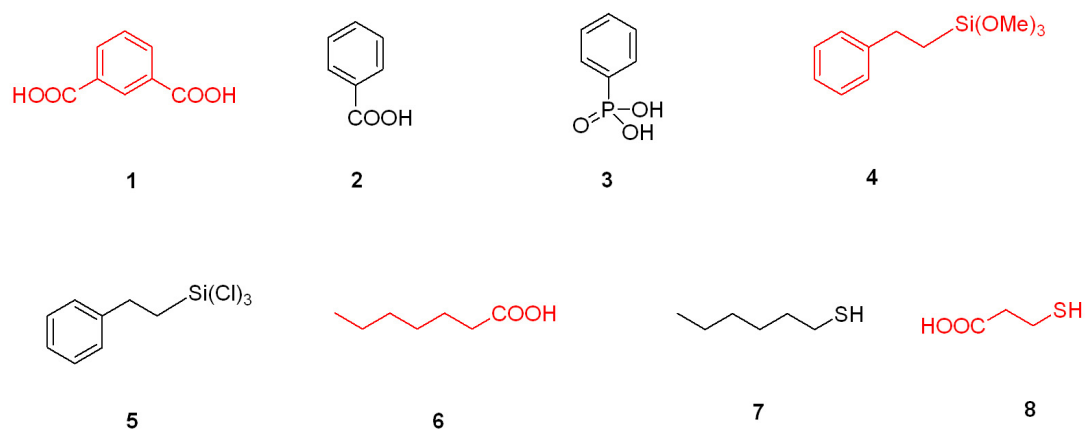


Fig 4.10 Compounds employed in the binding study. The compounds that did bind to the ZnO nanotips are shown in red.[77]

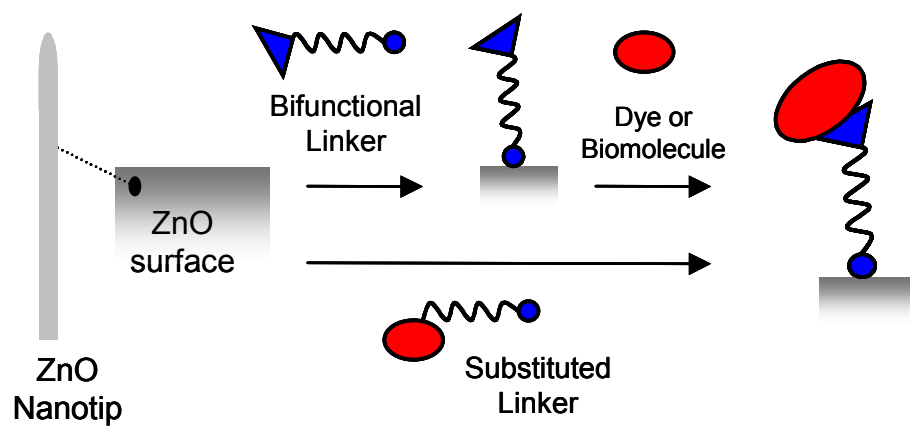


Fig 4.11 The schematic of the functionalization of ZnO nanotip using bifunctional linker.[77]

For comparison, the binding study was also performed on the epitaxial ZnO films. Typical binding procedures for the ZnO film and ZnO nanotips involved placing the samples in a solution in a suitable solvent (CH_3CN , THF, EtOH, or water, depending on the solubility of the compounds) overnight. Various concentrations, between 2 and 25 mM, were used for most compounds. Typical concentrations were 2 mM. The pH of the solutions was measured in each case. The samples were thoroughly rinsed and then immersed in pure solvent for 1 h. This was repeated several times until desorption of weakly bound or physisorbed molecules was no longer detected by UV-Vis or IR. Both ZnO films and nanotips samples, prior to and after binding, were stored in small containers placed in a desiccator and in the dark. No changes in the IR, UV, and fluorescence spectra were observed in bound films that were over 1 year old.

We employed Fourier transform infrared attenuated total reflectance (FT-IR-ATR) to probe the binding of nonchromophoric molecules. Single attenuated FT-IR-ATR spectra were performed on a Thermo Electron Corporation Nicolet 6700 FT-IR.

Table 4.1 summarizes the results for the binding of **1-8**. To study the binding we have taken into consideration (1) the anchoring groups, (2) the ZnO material, specifically ZnO nanotips and ZnO films, and (3) pH effects. These three factors are addressed in the following sections.

Anchoring Groups. *Carboxylic Acids and Derivatives.* Carboxylic acids and their derivatives (COOMe , COONa , COCl) form stable covalent bonds with metal oxide nanoparticles such as TiO_2 , SnO_2 , and ZrO_2 , mainly through carboxylate bidentate bonds

(II and III in Figure 4.12)[78-81]. On the basis of these results we investigated the binding of 1, 2, 6 and 8, to ZnO nanotips through COOH groups (Table 4.1).

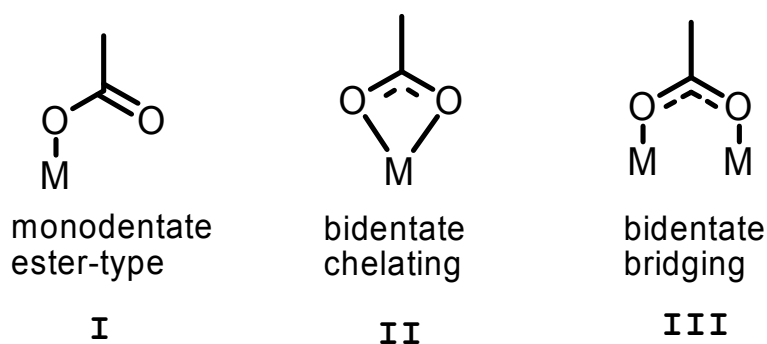


Fig 4.12 The three main binding modes between a COOH group and a metal oxide surface.[77]

In general, the FT-IRATR spectra of the bound nanotips were considerably weaker than those of the pure compounds, because a relatively small amount of compound binds.

Isophthalic acid **1** was bound to ZnO nanotip from an 18 mM THF solution, although the sample afforded a weak FT-IR-ATR spectrum (Figure 4.13). Benzoic acid **2** did not bind or physisorb to ZnO nanotip in a variety of binding conditions (Table 4.1). The binding of heptanoic acid **6** was then studied, because aliphatic carboxylic acids with chains of variable length and substituted with a number of different groups ($X-(CH_2)_n-COOH$, $X = NH_2, SH$, etc.) are commercially available. These could be versatile and readily accessible bifunctional linkers for the ZnO nanotips. However, we did not know whether both functional groups in the bifunctional linkers can be bonded to ZnO nanotips.

Table 4.1 Compounds Bound^f (b), Physisorbed^g (p), or Nonbound (nb) to ZnO [77]

compound	anchoring group	concentrations	ZnO material	result	detection methods
1	COOH	18mM	Nanotip	b	FT-IR-ATR
2^a	COOH	2-100mM	Nanotip	nb ^e	IR
3^c	P(O)(OH) ₂	10-20mM	Nanotip	p ^e	IR
		10-20mM	Film	nb ^e	
4	Si(OMe) ₃	2mM	Nanotip	b	FT-IR-ATR
5^d	SiCl ₃	2-25mM	Nanotip	nb ^e	IR
6	COOH	25mM	Nanotip	b	FT-IR-ATR
7^{b,d}	SH	2-25mM	Nanotip	nb	IR
		2-25mM	Film	nb	
8^b	COOH and SH	2mM	Nanotip	b	FT-IR-ATR
		2-25mM	Film	nb	

^a solution prepared from EtOH.

^b solution prepared from CH₃CN.

^c solution prepared from H₂O.

^d solution prepared from CH₂Cl₂.

^e sample etched by the acidic solution.

^f compounds can be detected by FT-IR-ATR and can not be rinsed off

^g compound can be easily rinsed off during the wash.

FT-IR-ATR spectra of the samples immersed in a 25 mM solution of **6** in CH₃CN clearly indicated that **6** binds to the samples (Figure 4.14). After the ZnO nanotip binding, the C-H stretch bands below 3000 cm⁻¹ due to the aliphatic chain did not shift, but the $\nu(\text{C=O})$ at 1708 cm⁻¹ disappeared with the appearance of a strong new band at 1534 cm⁻¹ and a very weak band at 1588 cm⁻¹ (the carboxylate asymmetric stretch, Figure 4.14). In addition, binding resulted in changes in the region of the C-O-H bonds (the 1417 cm⁻¹ C-O-H in-plane bending band) and in the disappearance of the $\nu(\text{C-O})$ bands at ~1250 cm⁻¹. The 935 cm⁻¹ band, due to the out-of-plane $\delta(\text{O-H})$, was absent in the spectrum of **6**/ZnO nanotip. Finally, the broad O-H stretch at 3300-2500 cm⁻¹ in the spectrum of **6** was not observed in the spectrum of **6**/ZnO nanotip. These changes clearly indicate that COOH group has formed a bond with ZnO nanotip, probably through carboxylate type bonds, given the disappearance of the $\nu(\text{C=O})$ and the appearance of the asymmetrical stretching bands at ~1500 cm⁻¹ (Figure 4.12 type II and III).

Alkylthiols (R-CH₂-SH). Alkanethiols are frequently used to functionalize gold or CdS nanoparticles[82-84], and a recent report suggests that thiols do bind to ZnO[85]. The attempts to bind hexanethiol **7** to the ZnO nanotip, however, had no success (Table 4.1) as the FT-IR-ATR spectra of the samples before and after binding were identical. 3-Mercaptopropionic acid **8**, however, did bind, as shown by a comparison of the FT-IR spectra before and after binding (Figure 4.15). The spectrum of **8**/ZnO nanotip, however, was considerably weak.

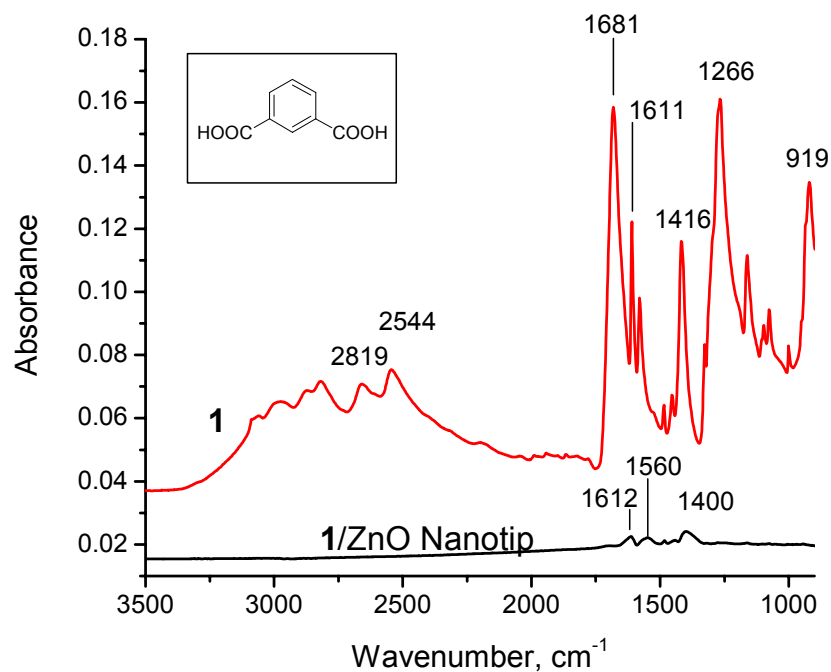


Fig 4.13. ATR spectrum of isophthalic acid **1** free (top, red line) and bound to ZnO nanotips (bottom, black line).[77]

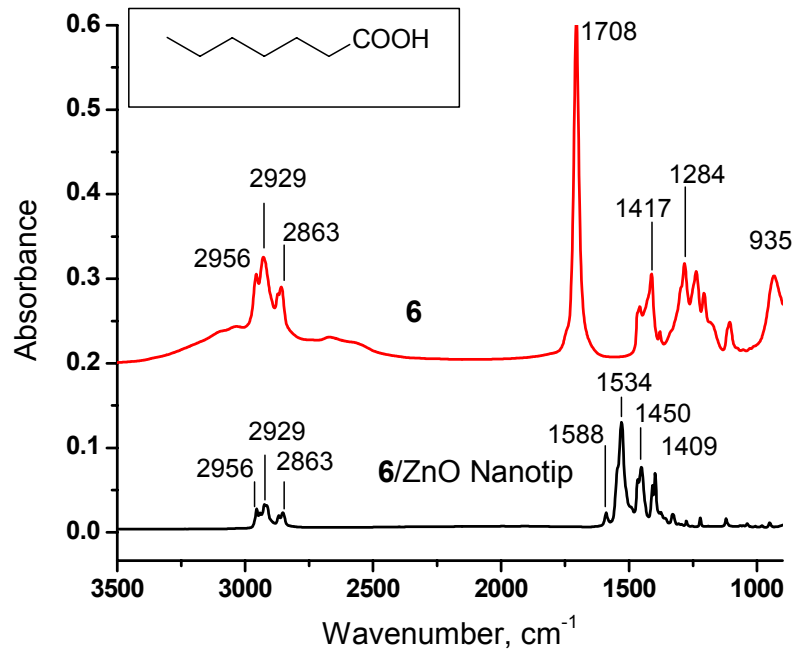


Fig 4.14 ATR spectra of free heptanoic acid **6** (top, red line) and **6** bound to ZnO nanotips (bottom, black line).[77]

Interestingly, the FT-IR-ATR spectrum (2000-1000 cm^{-1} spectral region) of **8**/ZnO nanotip was remarkably similar to that of heptanoic acid **6**/ZnO nanotip and so were the spectral changes observed upon binding: In the spectrum of **8**/ZnO nanotip, the $\nu(\text{C}=\text{O})$ band and the strong C-O bands at $\sim 1250 \text{ cm}^{-1}$ disappeared, while new bands due to the carboxylate stretch were observed in the 1550 cm^{-1} region.

In conclusion, the binding experiments with **6-8** suggest that the binding of 3-mercaptopropionic acid (**8**) to ZnO-N occurs by formation of surface bonds by the COOH group rather than by a bond through the SH group. This indicates that the thiol group in bifunctional **8** is nonbound and could be available for further functionalization of the surface. Although this result appears to be at variance with the only data for thiols on ZnO nanotips available in the literature (the acid binds also through SH)[85], the discrepancy could be due to differences in the ZnO nanotip sample preparation and surface properties. Our results have shown that these factors can greatly influence binding.

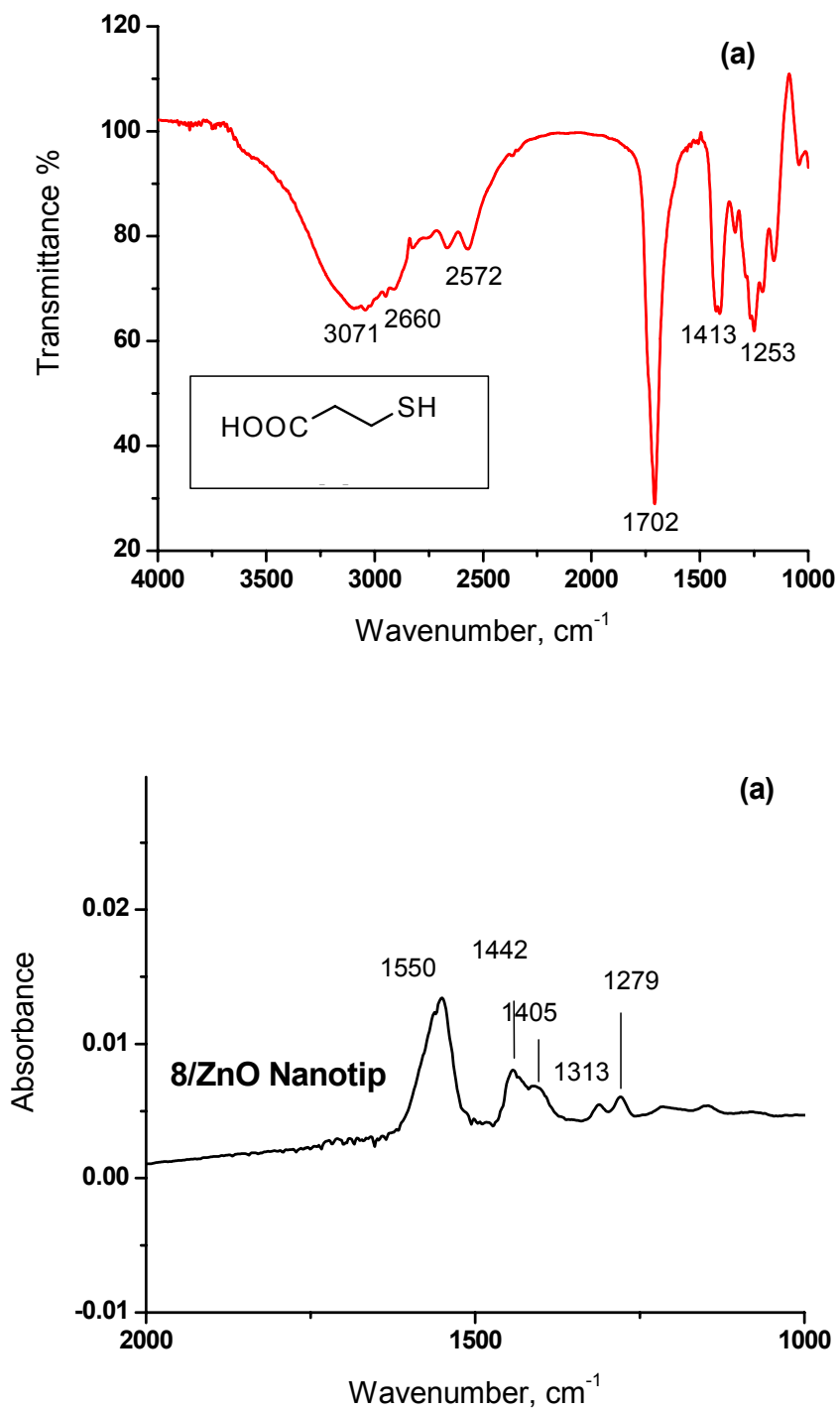


Fig 4.15 (a) IR spectrum of 3-mercaptopropionic acid (8). (b) ATR spectrum of 8 bound to ZnO nanotip showing the carbonyl region.[77]

Phosphonic Acid Group R-P(O)(OH)₂. The phosphonic acid group (R-P(O)(OH)₂) is an anchoring group widely employed for TiO₂ and other metal oxides[86]. The binding modes to metal oxide surfaces have been studied both experimentally and theoretically, and comparisons with the carboxylate group indicate that phosphonic acids bind more strongly to TiO₂ nanoparticles[87]. The study of P(O)(OH)₂ binding was done using phenylphosphonic acid **3**. The attempts to bind **3** to ZnO nanotip from 2-20 mM aqueous solutions, however, were not successful, and the samples were visibly etched and covered by a white, opaque patina. ZnO nanotips are readily etched in acidic conditions (pH ≤ 4)[80, 88] and phenylphosphonic acid **3** (pK_{a1} = 2.2) is a stronger acid than benzoic acid **2** (pK_a = 4.2) and isophthalic acid **1** (pK_{a1} = 3.7). Also, in the case of benzoic acid **2**, no binding to ZnO nanotip was observed using 2 mM solutions, but 25 mM solutions etched the samples, suggesting that higher concentrations of a weak acid can dissolve the samples. In conclusion, the fact that some groups did not bind may be due to an etching process, in which the acidic anchoring group “dissolves” the surface of the nanotips, forming a soluble complex with Zn[88]. The acid-base properties of colloidal ZnO particles have been studied by Bahnemann. It was shown that titration with acid leads to the dissolution of the ZnO colloid already below pH 7.4.

Silanes Si(X)₃, X = Cl, OR. The trichloro- or trimethoxy silane groups (Si(X)₃, X = Cl, OR) anchor to glass, silicon, TiO₂, and indium tin oxide (ITO) and have been used to attach dyes and other molecules to such substrates for a variety of applications[89-91]. The Si-Cl or Si-OR bonds are labile and form Si-OM bonds upon reaction with MO nanoparticles or surfaces. In addition, many bifunctional alkyl silanes having the structure R-(CH₂)_n-SiX₃, where R contains a second functional group, are commercially

available. We selected trimethoxy(2-phenylethyl)silane **4** and trichloro(2-phenylethyl)silane **5**, which carried both an alkyl and a phenyl group, thereby allowing us to detect their binding by inspecting the bands characteristic of the aromatic ring and the CH₂ groups in the FT-IR-ATR spectra. Several attempts to bind **5**, however, resulted in complete peeling off of the nanotips, as no ZnO was detected (UV, FT-IR) on the sapphire or glass slides after immersing the samples in acetonitrile solutions of **5**. Furthermore, etching of the ZnO layer occurred within minutes. We concluded that the solutions of the trichlorosilane were too acidic (pH ~1-0.5). Binding experiments of acetonitrile solutions of the trimethoxysilane **4** to ZnO nanotips were not successful, but it was possible to bind this molecule after acid pretreatment of the more robust MgZnO samples.

Effect of ZnO Morphology on Binding. In addition to ZnO nanotips, we studied the binding of **3**, **7** and **8** to ZnO film samples. Significant binding of **3**, **7** and **8** to the ZnO film samples could not be detected. This result was not unexpected, given the smaller surface area of flat films compared to the nanotips.

Effect of pH and using MgZnO. The treatment of TiO₂ films prepared by sol-gel (hydrothermal) methods with acids or bases prior to binding and the pH of the binding solutions are important factors that influence the binding affinity as well as the type of chemical bonds between a functional group and the surface[86, 92]. For instance, it has been found that the type of chemical bond that the COOH anchoring group forms with the surface depends on the pH treatment of the TiO₂ film before binding. Pretreatment with acids results in ester-type bonds, and pretreatment with bases forms carboxylate-

type bonds[92-95]. Moreover some molecules that did not bind to acid-pretreated films would bind to films treated with base[92, 93].

Since ZnO is readily etched in acidic ($\text{pH} \leq 4$) conditions, this material could not be employed to test binding at low pH. We have developed epitaxial $\text{Mg}_x\text{Zn}_{1-x}\text{O}$ films and nanotips by alloying ZnO with MgO [96, 97] and observed that it is more resistant to acids. $\text{Mg}_x\text{Zn}_{1-x}\text{O}$ nanotips were therefore developed for this work, because they would allow us to employ a wider pH range. The percentage of MgO in alloyed ZnO was varied in the 5-10% range [96, 97]. We observed that MgZnO nanotip samples have binding properties similar to those of the ZnO nanotip samples. For instance, the IR spectra of **8**/ZnO nanotip and **8**/MgZnO nanotip were indistinguishable (Figures 4.16).

The pH pretreatment of MgZnO nanotip samples involved rinsing the slides with deionized water, placing them in an oven at 400 °C for 10 min, followed by cooling and immersion in an acidic or basic aqueous solution for 30 min. Acidic ($3 < \text{pH} \leq 5$) and basic ($8 \leq \text{pH} \leq 11$) aqueous solutions were prepared using H_2SO_4 and NaOH, respectively. These pretreated films were then used in the usual binding procedures.

Preliminary experiments performed with trimethoxy(2-phenylethyl)silane (**4**), a potentially useful linker that we had been unable to bind to ZnO nanotip, suggested that an acidic or basic pretreatment of MgZnO nanotip did influence the binding properties. For instance, **4** did bind to MgZnO nanotip samples that were pretreated with acid (pH 3 and 4) as well as base (pH 9.5), while it did not bind to samples (MgZnO nanotip or ZnO nanotip) that were not pretreated at all. A possible explanation for this behavior is that acid or base pretreatment generates defects on the ZnO nanotip surface, making it more reactive. More work will be done to verify this assumption. Clearly, the increased

resistance to acids of the MgZnO nanotip samples is potentially very useful, as preliminary experiments suggest that acidic linkers that etched the ZnO nanotips may bind to these more sturdy nanotips.

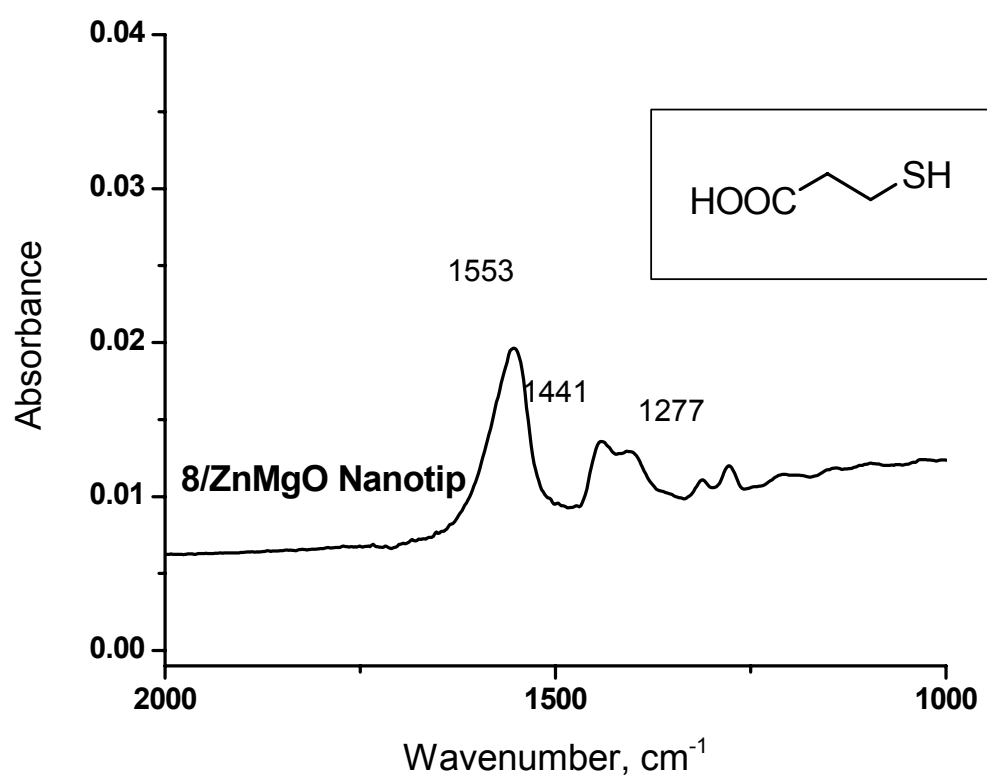


Fig 4.16. ATR spectrum of 8 bound to ZnMgO nanotip. This spectrum is identical that of 8/ZnO nanotip shown in Figure 4.15(b).[77]

4.4. Summary

In this chapter, we have demonstrated the control of the wettability transitions of ZnO nanotips and films grown on various substrates. It is found that the ZnO nanostructured surface greatly enhances the wetting effects in comparison with the epitaxial ZnO film with flat surface. Superhydrophilic ZnO nanotips are achieved by UV illumination, whereas hydrophobic ZnO nanotips are realized after low-temperature oxygen annealing. The unprecedentedly fast transition rates have been demonstrated. These transitions can be reversibly repeated in multiple cycles. The effects of wettability control on the sensing surface will be discussed in Chapter 6.

In order to realize the selective sensing in our biosensor system, we have described here the functionalization of ZnO nanotip with bifunctional linkers and made a comparison between the binding properties of ZnO nanotips with ZnO epitaxial films. The binding experiments indicate that the carboxylic acid group (COOH) is a suitable anchoring group for binding to the ZnO nanotips but that the number and position of the COOH groups, the acidity of the anchoring group, and solution pH also play a role in the binding. The ZnO nanotip provided excellent binding surfaces when compared to ZnO films. The experimental design and results of DNA immobilization on ZnO nanotip-based sensors will be discussed in Chapter 6.

Chapter V. ZnO Nanotip-based SAW Sensors

Discussed in Chapter III, ZnO material can play an important role in the multifunctional sensing applications. Through proper doping, ZnO can be made semiconductive, highly conductive, transparent, piezoelectric, and ferromagnetic. Also, ZnO can be alloyed with CdO and MgO for energy bandgap engineering. With such properties, ZnO has many applications including optoelectronic devices, acoustic devices, spintronics, MEMS and NEMS, and sensors and by integrating its versatile properties. Novel multifunctional sensing devices can be developed. ZnO nanostructures have become one of the most important and useful multifunctional nanostructures. ZnO nanostructures made by MOCVD are grown at relatively low temperatures (300~500 °C), giving ZnO a unique advantage over other wide bandgap semiconductors, such as GaN and SiC nanowires. MOCVD growth can also provide atomically sharp interface control, and possible end-facet morphology control for various device applications by altering the growth conditions, without the presence of a metal catalyst. Catalyst-free growth of ZnO nanotips by MOCVD leads to superior optical properties, as these nanotips exhibit free excitonic emission both at 10K and room temperature [61]. The electrical conductivity of these nanostructures can also be controlled by in-situ doping during growth. The recent progress in nanoscale science and engineering are promising for the fabrication of novel nano-biosensors with faster response and higher sensitivity and selectivity than that of planar sensor configurations, due to their small dimensions combined with dramatically increased contact surface and strong binding with biological and chemical reagents. Such novel sensors can be used to detect gas absorption and biological molecules interactions of DNA-DNA, DNA-RNA, protein-protein, and protein-small molecules. ZnO

nanostructures were used for H₂ [98, 99], NO₂ [99], O₂ [100], NH₃ [101], ozone [102], and ethanol [98] sensors. ZnO nanostructures were integrated with traditional acoustic devices for gas and bio sensing [99, 103-105].

We designed and fabricated the novel ZnO nanotip-LiNbO₃ SAW (N-SAW) biosensor and ZnO nanotip-Quartz QCM (N-QCM) biosensor, which integrate ZnO nanostructures with LiNbO₃ SAW delay lines and quartz crystal microbalance, respectively. The ZnO nanotip array is used for surface modification and immobilizing the bio-receptor, while the SAW device fabricated on 128° Y-cut LiNbO₃ or the quartz crystal microbalance are used as the transducer to detect the mass loading effect resulting from the analyte-receptor reaction. This chapter is focused on the design, modeling, fabrication and test of ZnO N-SAW devices, while the next chapter is mainly discussing the ZnO N-QCM device and the effects of surface modifications for biological sensing.

5.1. Device Design and Fabrication

The novel ZnO N-SAW biosensor integrates ZnO nanostructures with LiNbO₃ SAW delay lines. The ZnO nanotip array is used for immobilizing the bio-receptor, while the SAW device fabricated on 128° Y-cut LiNbO₃ is used as the transducer to detect the mass loading effect resulting from the analyte-receptor reaction. The basic structure, mask design and fabrication process of the device are presented.

The LiNbO₃ SAW device with the ZnO nanotip array is schematically shown in Figure 5.1. The device consists of two SAW channels, a reference and a sensing channel. The test devices are regular SAW delay lines. Two inter-digital transducers (IDTs) are fabricated on a 128° Y-cut LiNbO₃ substrate with a ZnO nanotip array / SiO₂ layer structure deposited on the SAW propagation path. A 150 nm SiO₂ film was first

deposited on the LiNbO₃ by plasma enhanced chemical vapor deposition (PECVD). A mesa pattern (1116 $\mu\text{m} \times 594 \mu\text{m}$) containing the ZnO nanotips on SiO₂ layer was formed using photolithography followed by an etching process. The input and output aluminum IDTs consist of 50 pairs of electrodes with a periodicity of 12 μm , an acoustic aperture of 960 μm and a center-to-center distance of 1200 μm . The IDTs were formed by e-beam evaporation of Al and a lift-off process.

The device parameters are given in Table 5.1. For 128° Y-cut LiNbO₃ substrates, $\lambda = 12\mu\text{m}$ gives a center frequency of 305.6MHz and a 3 dB Bandwidth (BW_{3dB}) of 1.8%.

Figure 5.3 shows the simulated transmission spectra for the SAW delay line fabricated on 128° Y-cut LiNbO₃ and ST cut quartz. The device parameters are based on the data in Table 5.1 and the center frequency is about 305MHz. Due to the high coupling coefficient, the device on 128° Y-cut LiNbO₃ has about 50dB less insertion loss than the same device structure on ST cut quartz. It makes 128° Y-cut LiNbO₃ substrate to be a good option for the sensor templates, since the ZnO nanotip and extra binding layer would involve much more insertion loss due to the mass loading effects and charge changes on the delay path.

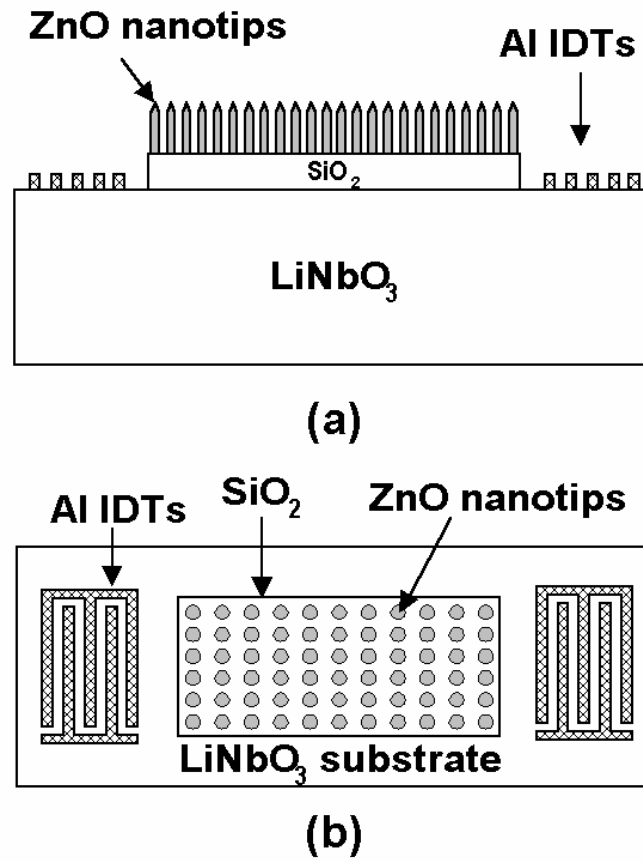
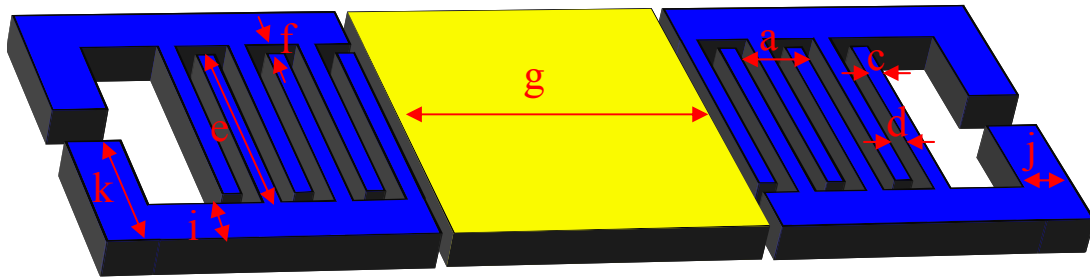


Fig 5.1 Schematic of the ZnO nanotip-based SAW biosensor structures: (a) cross-section, (b) top view.

Table 5.1. Design Parameters of the SAW Sensors

Parameter	Dimensions
a) Wavelength (λ)	12 μm
b) # of electrodes per IDT	100 (50 finger pairs)
c) Electrode width	0.25 λ , 3 μm
d) Electrode spacing	0.25 λ , 3 μm
e) Electrode length	80 λ , 963 μm
f) Electrode end gap	0.25 λ , 3 μm
g) IDT1-IDT2 edge-to-edge spacing	50 λ , 600 μm
h) Mesa size	1116 $\mu\text{m} \times 594 \mu\text{m}$
i) Busbar width	75 μm
j) Bond pad width	75 μm
k) Bond pad length	458 μm

**Fig 5.2 Schematic of the ZnO nanotip-based SAW biosensor structures with design parameters as shown in Table 5.1**

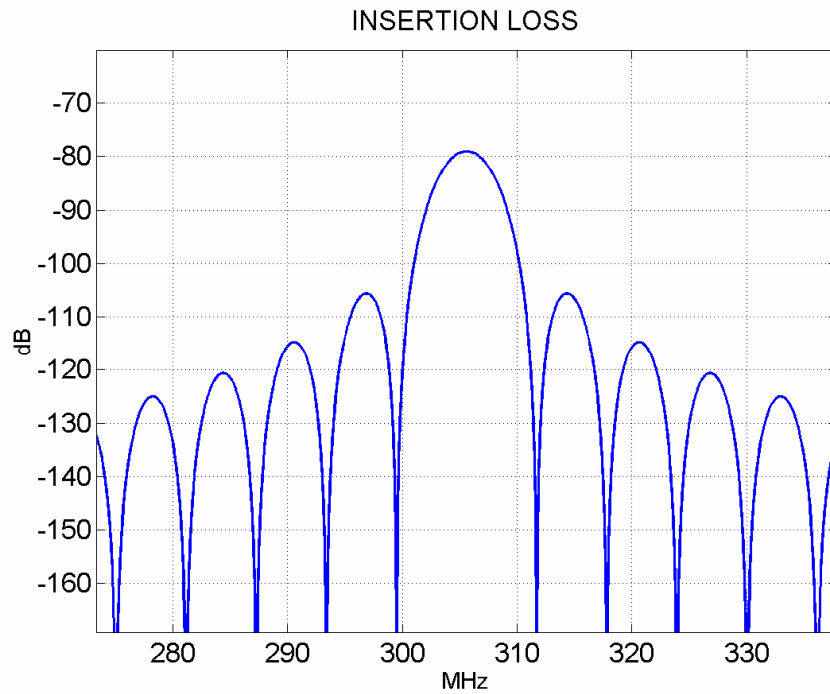
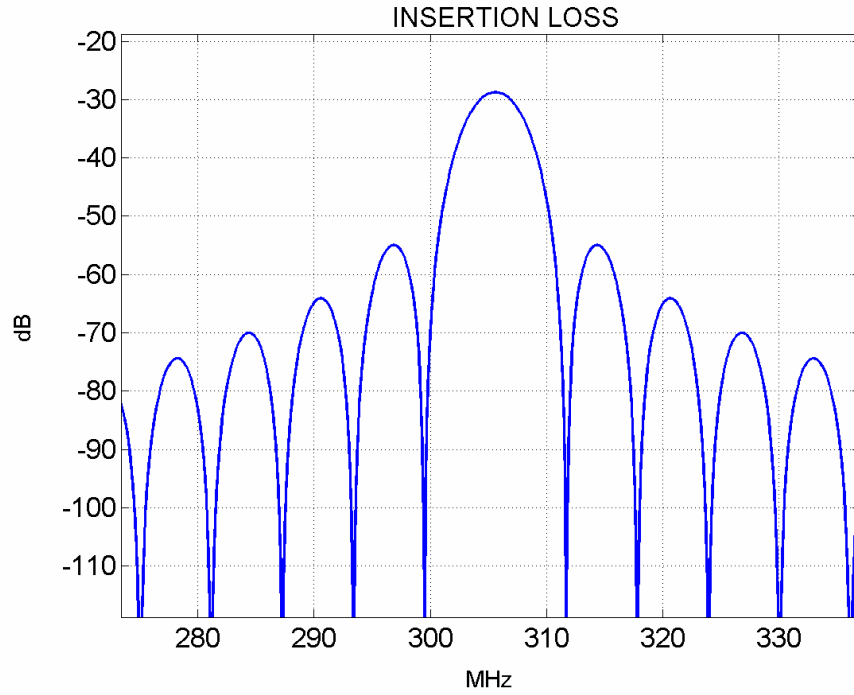


Fig 5.3 The simulated results of transmission spectra for the SAW delay line based on the Design parameters shown in Table 5.1, fabricated on (a) 128° Y-cut LiNbO₃ and (b) ST cut Quartz.

The N-SAW sensor mask set was design using Tanner EDA's L-Edit Pro 8.3 layout design software on a Windows 98 PC. The design was then converted to GDSII format and sent to the mask vendor.

The prototype of the N-SAW sensor mask set has two layers, one for SAW IDT structure, and one for the ZnO nanotip array etching.

The device consists of two SAW channels, a reference and a sensing channel. In the test, the reference channel had no biological component bonding, whereas the sensor channel was bonded with DNA oligonucleotide or protein on the ZnO nanotip array.

The devices are fabricated on 128° Y-cut LiNbO₃ substrates with thickness of 480 μm . The fabrication process mainly involves wafer cleaning, SiO₂ film deposition, ZnO nanotip growth, aluminum metallization, photolithography and etching. After wafer cleaning, a thin layer of SiO₂ film can be deposited on the LiNbO₃ by plasma enhanced chemical vapor deposition (PECVD) or sputtering. The ZnO nanotip arrays with an average height of 500nm-1000nm can be grown on the SiO₂ film by MOCVD. A mesa pattern containing the ZnO nanotips on the SiO₂ layer is formed by using photolithography followed by two etching processes. The ZnO nanotips can be etched by H₂O₂ + Ammonium (1:1) and the SiO₂ film was etched by 7:1 diluted Buffered Oxide Etchant (BOE). The input and output aluminum IDTs consist of 50 pairs of electrodes with a periodicity of 12 μm and an acoustic aperture of 960 μm . The IDTs can be formed by e-beam evaporation of Al and a lift-off process. 150nm aluminum should be evaporated on the LiNbO₃ surface. This thickness corresponds a little less than 2% of the device wavelength, and is necessary for reliable lift-off. The acoustic velocity will decrease under the electrodes due to the shorting of the horizontal electrical field and

mass loading by aluminum. Thicker metal deposition is preferred to ensure a good connection between the bonding pad and the test probes. However, a thicker metal layer will increase the mass loading effect and also increase the difficulty of the lift-off process.

5.2. DNA Oligonucleotide Immobilization and Hybridization

The sensing surfaces, the ZnO nanotip array, are first functionalized by immobilizing DNA oligonucleotide. A schematic representation of the DNA immobilization process is shown in Figure 5.4.

A 1 $\mu\text{g}/\mu\text{l}$ synthesized DNA oligonucleotide (5'-AGAAAATCTTAGTGTC-3') solution was labeled with ^{32}P - γ -dATP using DNA T4 kinase. The unincorporated nucleotides were removed by Micro Bio-Spin® Chromatography Column (Bio-Rad). 13 μl of the labeled DNA solution was applied on the ZnO nanotips, and incubated at room temperature for 1 hour. The surface was then washed with DI water (500 μl at each application, repeated 10 times). The amount of DNA remaining on the ZnO nanotip surface was determined by a survey meter counter and by Cherenkov counting in 1209 Rackbeta Liquid Scintillation Counter (LKB, Pharmacia). The radioactivity of the collected wash solution was measured by a scintillation counter for comparison. Different surfaces, such as LiNbO_3 and ZnO flat film, were treated with the same method for comparison of the immobilization efficiency. A comparative study of immobilization of DNA oligonucleotide on different surfaces was carried out by radioactivity testing. Followed by incubation and wash steps mentioned above, 1 $\mu\text{g}/\mu\text{l}$ DNA oligonucleotide solution was applied over 0.1 cm^2 substrates of LiNbO_3 , (0001) ZnO film, and ZnO nanotip array. The LiNbO_3 substrate and the ZnO film have little immobilization of oligonucleotide (27 ng/cm^2 and 80 ng/cm^2 respectively). In comparison, the

oligonucleotide immobilization on the ZnO nanotip arrays (1.6×10^4 ng/cm²) is approximately 200 times larger than the flat ZnO film surface and approximately 600 times larger than the LiNbO₃ substrate, shown in Figure 5.5. The ZnO nanostructures possess a giant surface area, which provide more binding sites and larger effective sensing area than the planar surface.

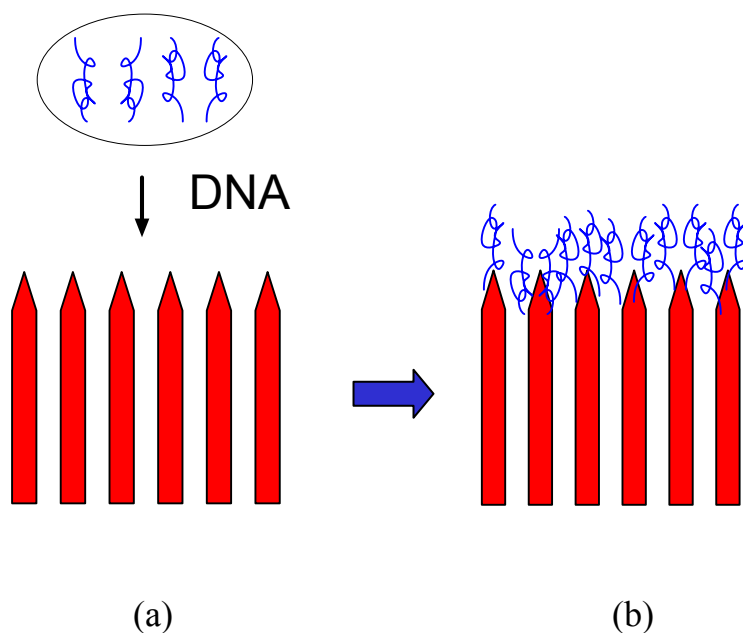


Fig 5.4 Schematic representation of the DNA immobilization process. (a) Before immobilization; (b) After immobilization.

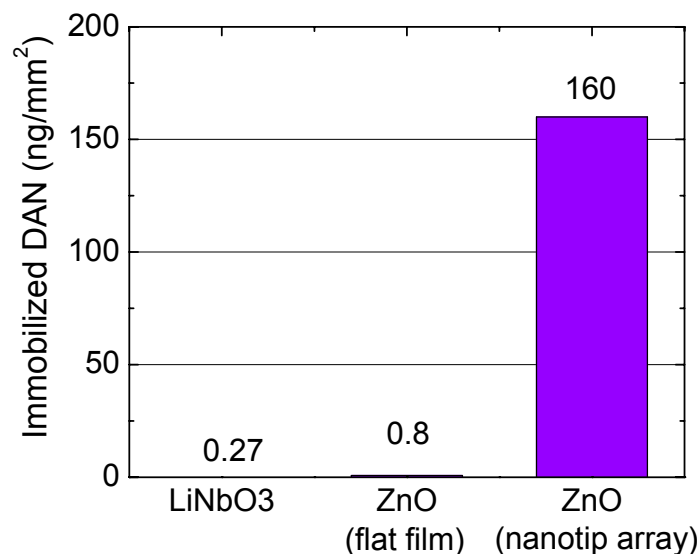


Fig 5.5 Immobilization of DNA oligonucleotide on different surfaces. (1) LiNbO₃; (2) ZnO flat film; (3) ZnO nanotip array. The oligonucleotide immobilization on the ZnO nanotip arrays is approximately 200 times larger than the flat ZnO film surface and approximately 600 times larger than the LiNbO₃ substrate.

DNA Oligonucleotide Hybridization

Avidin, Biotin-DNA 1st strand (5'-AGAAAATCTTAGTGTC-3'), DNA complementary 2nd strand (5'-GACACTAAGATTTTCT-3') and non-complementary 2nd strand APE (5'-TTTTACGATACCAGTCAT-3') are used for hybridization of the DNA oligonucleotide. Figure 5.6 shows the experimental procedure of hybridization. First, labeled DNA (complementary and non-complementary--APE) is prepared as previously described. The ZnO nanotip surface is first immersed in 100 μ l avidin solution (1 μ g/ μ l), and incubated at room temperature for 1 hour. The surface is rinsed by DI water to remove unbound avidin. The same steps are repeated with Biotin-DNA 1st strand solution (1 μ g/ μ l) on the same surface to immobilize the first strand DNA. Then 4 μ l of the

radioactive labeled second strand DNA oligonucleotide is applied on the surface (100 ng/ μ l), and incubated at room temperature for 30 minutes. The surface was washed with DI water. The amount of second strand DNA was determined by a radioactivity test.

For sensor device testing, the same procedure will be repeated with unlabeled DNA oligonucleotide on the sensing area and followed by the acoustic wave signal measurement.

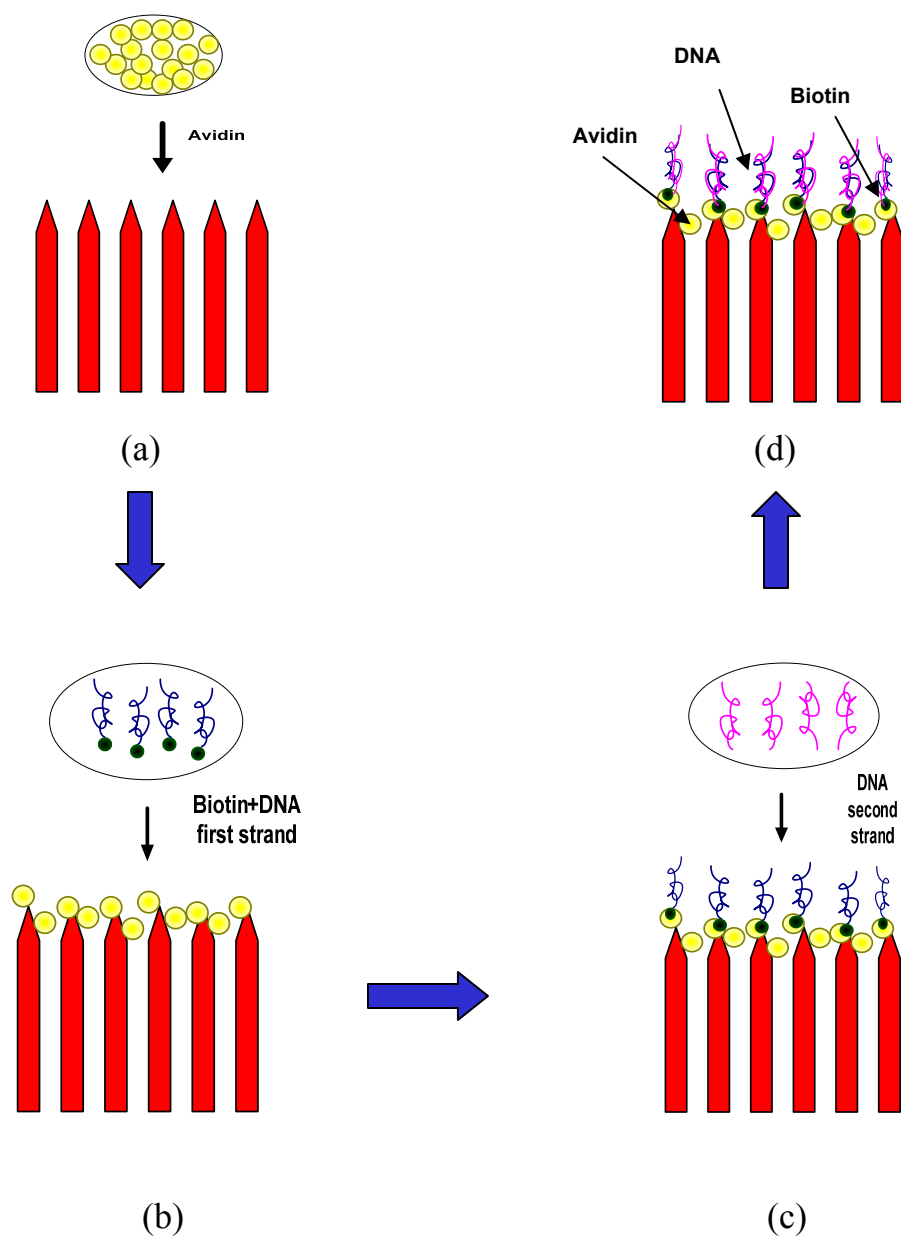


Fig 5.6 Schematic representation of the DNA hybridization process: (a) Applying Avidin (protein immobilization); (b) Applying Biotin-DNA primary strand; (c) Applying DNA complementary secondary strand (or non-complementary secondary strand APE, the control solution); (d) After DNA hybridization.

5.3. Sensors Testing

The SAW responses from reference and sensing channels of the devices are tested using an HP 8573D Network Analyzer (Agilent Technologies, Palo Alto, CA), shown in Figure 5.7. The setup consists of the HP 8573D network analyzer, a Cascade Microtec 9100 probe station, Air Coplanar Probes for on-wafer testing and the samples with the fabricated devices. The Cascade Microtech Air Coplanar Probes had tip-to-tip distance of 650 μm .

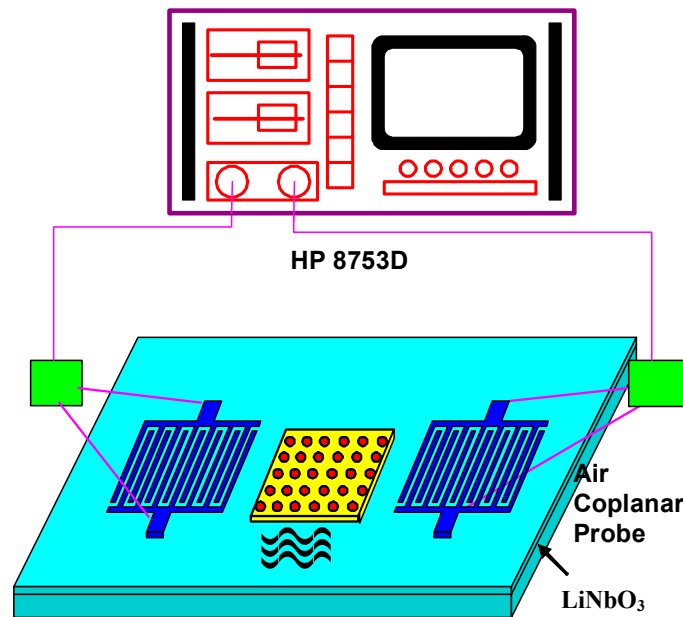


Fig 5.7 The N-SAW Characterization test setup

The frequency spectrum and phase shift of the test devices are used to characterize the sensors. Velocity dispersion data can be extracted from the nulls in the frequency spectrum.

First, the SAW responses of the bare LiNbO₃, LiNbO₃ with a SiO₂ layer, and LiNbO₃ with ZnO nanotip array on the SiO₂ layer were measured to analyze the effect of the SiO₂ layer and ZnO nanotip array. The device responses were also measured after DNA oligonucleotide immobilization. Finally, after DNA hybridization, the device's performance as a sensor was evaluated. In the test, the reference channel had no biological component bonding, whereas the sensor channel was bonded with DNA oligonucleotide on the ZnO nanotips. Phase velocities were obtained from the center frequency of the device frequency response. To determine the device sensitivity experimentally, frequency and phase response measurements were made by loading with different biological components.

Figure 5.8 shows the transmission spectra for the SAW delay line fabricated on different substrates. The SAW responses of the bare LiNbO₃, LiNbO₃ with SiO₂ layer, and LiNbO₃ with ZnO nanotip array on SiO₂ layer were measured. The measured center frequency of the SAW devices is 305.6MHz, with an insertion loss of approximately 16dB prior to SiO₂ and ZnO nanotips deposition. In order to identify the effect of the SiO₂ layer and ZnO nanotips on SAW performance, sample devices were tested after each deposition and patterning step. After the deposition of the 200 nm thick SiO₂ layer, less than 0.1 dB of additional insertion loss was observed. In comparison, the insertion loss increased by 9 dB after the ZnO nanotips deposition. This additional insertion loss is primarily due to the ohmic loss induced by free carriers in the ZnO nanotips.

As-grown ZnO generally shows n-type semiconducting behavior. As both the reference and sensing channels of the prototype sensor contain ZnO nanotips on SiO₂ films, this effect on the SAW response is automatically subtracted by using a differential

mode measurement. This additional loss can be reduced by compensation doping of the ZnO nanotips, using dopants such as Li[106], Ni[107] or Cu[108].

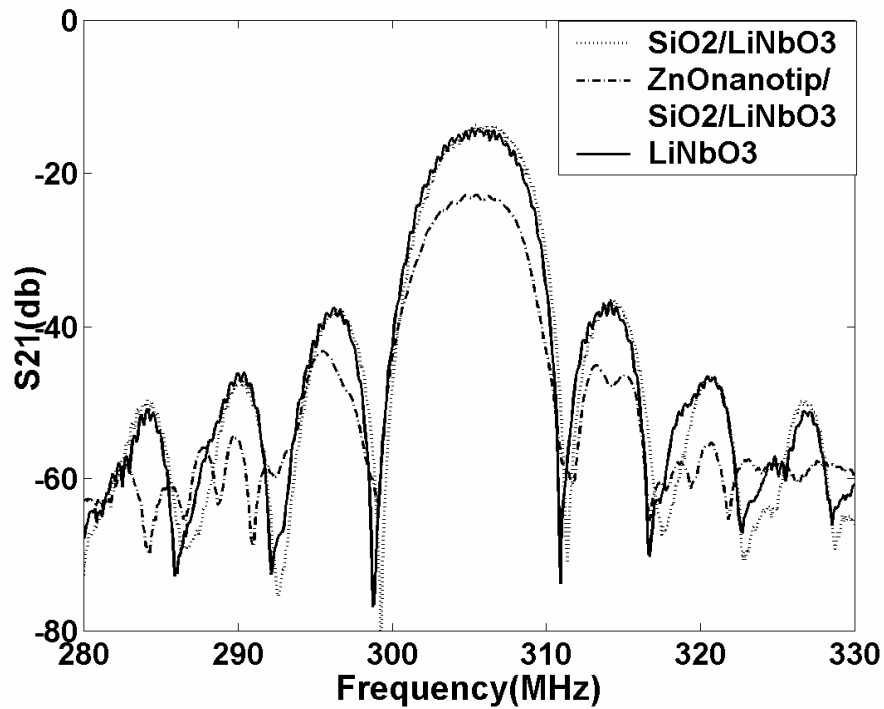


Figure 5.8 S_{21} (transmission) spectra for the SAW sensors fabricated on bare LiNbO_3 , LiNbO_3 with SiO_2 layer, and LiNbO_3 with ZnO nanotip array on SiO_2 layer.

In the DNA oligonucleotide immobilization test, when a 1 $\mu\text{g}/\mu\text{l}$ DNA oligonucleotide solution was applied on the sensor channel, a 191° phase shift (Figure 5.9) and 6.5 dB of additional insertion loss at the center frequency of 327.94 MHz was observed compared with the reference channel. Two prorogations directions of the 128° Y-cut LiNbO_3 substrates were used. In different directions, the group velocities of surface acoustic waves are different, so the center frequency has changed from 305.6 MHz to 327.94 MHz. In order to realize the efficient hybridization of DNA oligonucleotide and to avoid the second strand DNA oligonucleotide directly binding to the nanotips, avidin and biotin were introduced onto the nanotip array surface. After avidin saturated the surface, biotin-DNA (185 del WT) was applied on the reference channel and the two sensor channels. Then the sensor channels were used to sense the non-complementary (APE) and the complementary second strand DNA oligonucleotide. In the radioactive test, $4.32 \text{ ng}/\text{mm}^2$ APE and $7.33 \text{ ng}/\text{mm}^2$ complementary DNA oligonucleotide were detected. In the SAW device test, at the center frequency, a 9° and a 13° phase shift were observed on the non-complementary and the complementary second strand DNA sensor channels, respectively.

To compare the performance of the ZnO nanostructure with smooth surfaces, devices with bare LiNbO_3 and ZnO flat film on LiNbO_3 on the propagation path were also tested. No phase shift or additional insertion loss was observed on those smooth surface devices, as very little DNA oligonucleotides were immobilized.

Mass sensitivity of a SAW sensor in the feedback loop of an oscillator circuit can be calculated by determining the mass on the sensor surface, and the total frequency change caused by this mass accumulation:

$$\text{Mass Sensitivity} = \frac{\Delta f / f_c}{\Delta m / A} \quad (5.1)$$

where m is the total mass on the active surface with area of A , f_c is the center frequency of the SAW device, and Δf is the frequency shift of the oscillator circuit. As the SAW sensors were tested using a network analyzer, we used the phase shift, $\Delta\Phi$, across the device, instead of frequency shift. For $\Delta\Phi < 360^\circ$, Δf is related to $\Delta\Phi$ by the relation:

$$\Delta f = \frac{\Delta\Phi \times V_{SAW}}{360^\circ \times L} \quad (5.2)$$

where L is the center-to-center distance of SAW delay line, and V_{SAW} is the acoustic velocity. Thus, in terms of phase shift, mass sensitivity is derived as:

$$\text{Mass Sensitivity} = \frac{A}{\Delta m} \frac{\Delta\Phi \times V_{SAW}}{360^\circ \times L \times f_c} \quad (5.3)$$

The sensitivity to immobilization is thus $357.1 \text{ cm}^2/\text{g}$, while the sensitivity to the target second strand DNA oligonucleotide is $526.3 \text{ cm}^2/\text{g}$. The sensitivity of the N-SAW sensor is comparable to the latest reported ZnO based SAW biosensors[99].

It should be noted that these preliminary results could be improved by optimizing the SAW sensor design and the hybridization process.

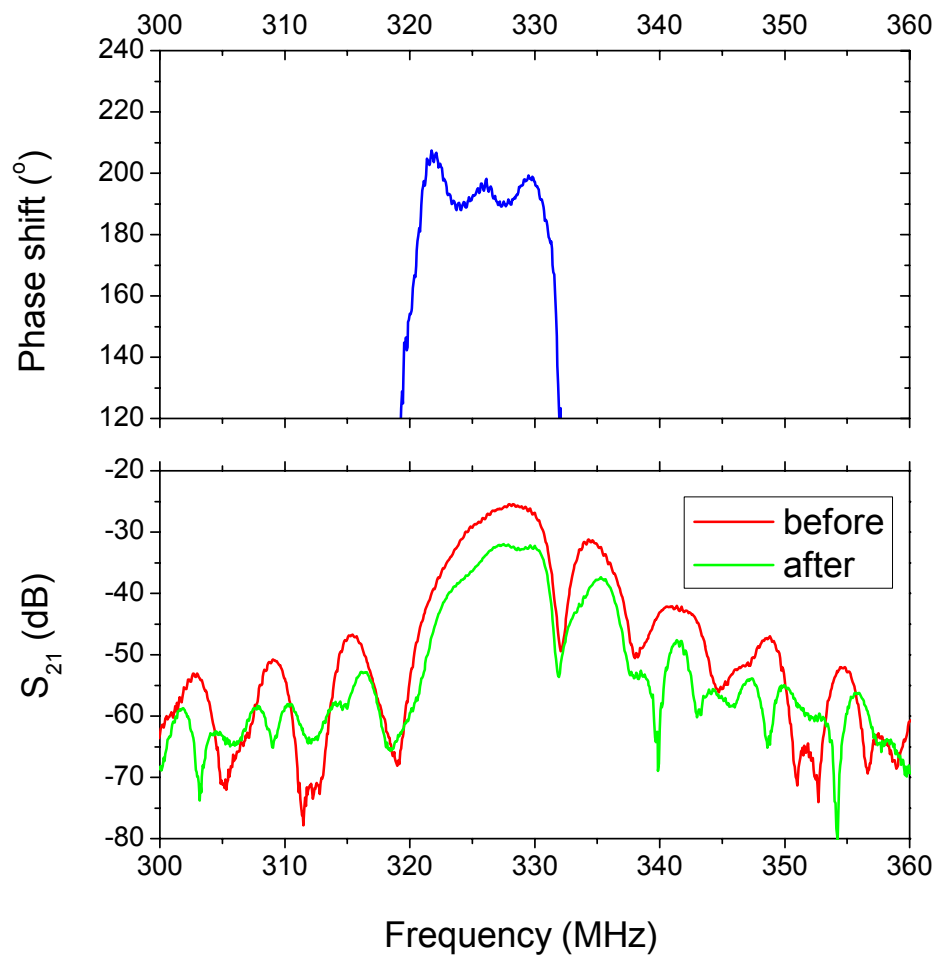


Fig. 5.9 S_{21} (transmission) spectra for the ZnO nanotip SAW sensor, before and after DNA oligonucleotide immobilization. The phase shift at the center frequency of 327.94 MHz is 191°.

We also conduct the protein detection using the same device structure. The dual channel (reference and sensor channels) device was tested using an Agilent 8573D Network Analyzer. The reference channel has no protein bonding and the sensor channel is bonded with 100ng protein on the ZnO nanotip over an area of $6.629 \times 10^{-3} \text{ cm}^2$.

As shown in the Figure 5.10, the sensor device has a shift to lower frequency compared with the reference device. An additional insertion loss of 6.14 dB is observed for the protein bonded sample. However, the insertion loss shift depends on a number of factors, and by itself is not a good sensing mechanism. Instead, the phase shift of the signal is preferred for accurate and repeatable measurements.

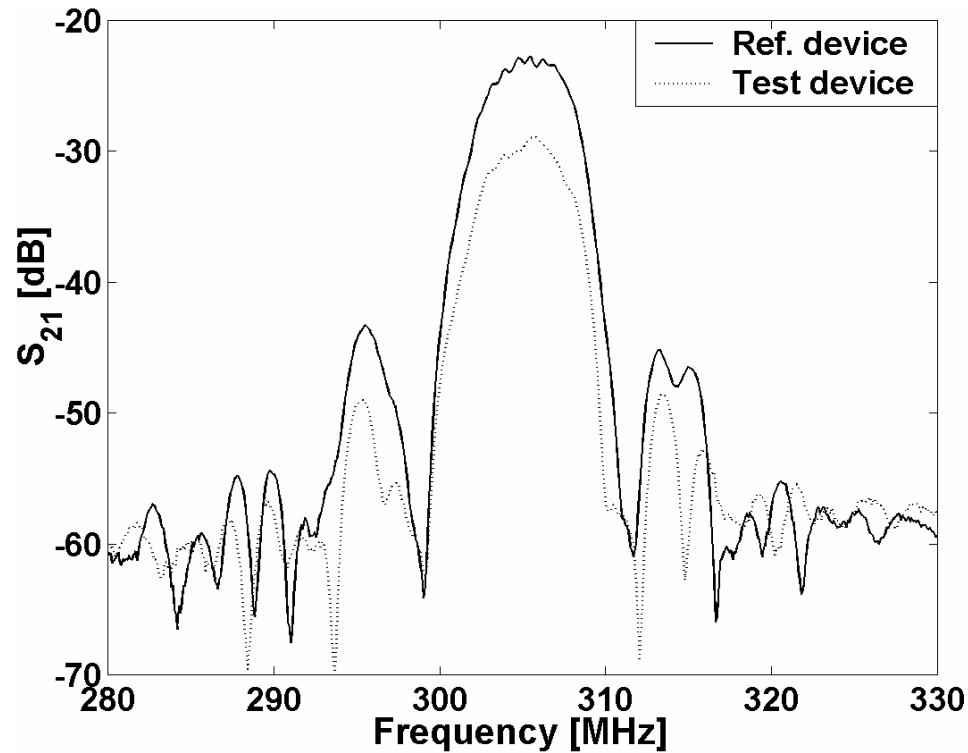


Fig. 5.10 Measured S_{21} (transmission) spectra for the reference and sensor devices for 100ng protein detection

As shown in Figure 5.11, the sensor device has a 47.68° phase shift at the center frequency 305MHz compared with the reference device. The phase shift increases with increasing frequency, due to the different velocity dispersion characteristics of the SAW propagating in the reference and sensor channels. Nominally, the phase shift should be a monotonically increasing function. However, due to such factors as electromagnetic feedthrough and triple transit interference (TTI), the phase response has ripples. The real sensor device will be optimized to minimize the impact of these secondary effects on sensor performance and will have much narrower bandwidths.

Mass sensitivity of the sensor for protein detection can be calculated by equation (5.3). Δf is 0.274MHz and the mass Sensitivity is $59.5 \text{ cm}^2/\text{g}$.

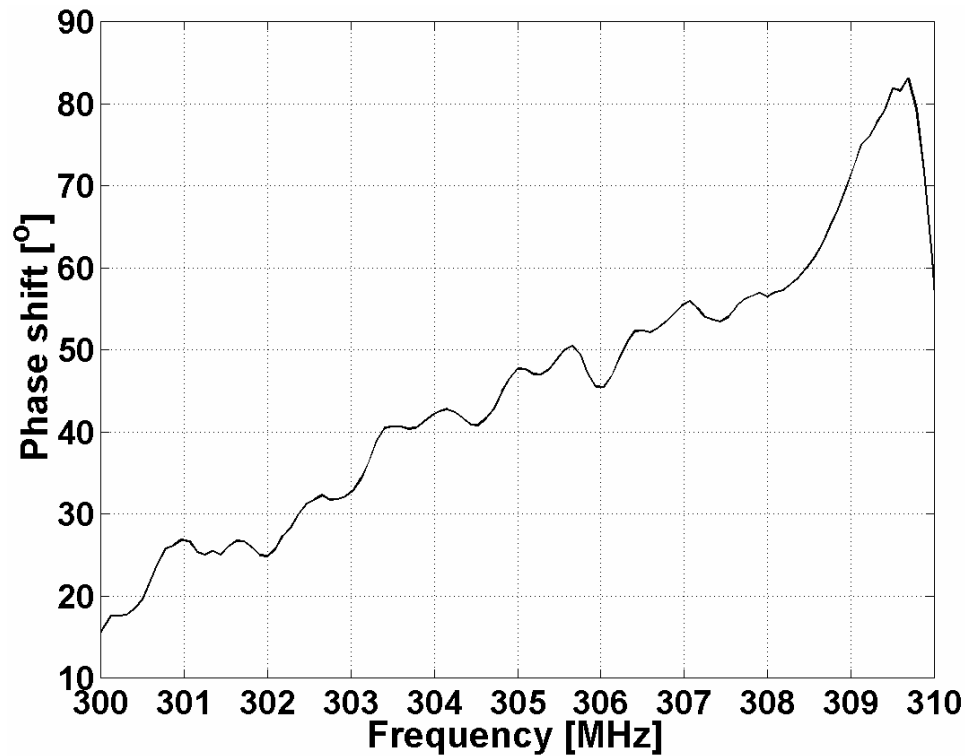


Fig. 5.11 Phase difference between the reference and sensor devices due to 100 ng protein detection.

5.4. Summary

In this chapter, a novel SAW biosensor using a ZnO nanotip array for enhanced DNA immobilization has been demonstrated. This biosensor integrates a ZnO nanotip array with a SAW device fabricated on 128° Y-cut LiNbO₃. The ZnO nanotip array is used for immobilizing the bio-receptor, while the SAW device functions as the transducer to detect the mass loading effect resulting from the analyte-receptor reaction. The ZnO nanotip arrays are shown enhance DNA immobilization by a factor of 200 compared to smooth surface ZnO films. This immobilization enhancement of ZnO nanotips is attributed to the fact that ZnO nanotips have large surface area and lower binding energy compared with planar surface. The sensor is functionalized by immobilizing first strand DNA oligonucleotide on the ZnO nanotip array, after which the device can selectively sense its complementary secondary strand DNA oligonucleotide. This device structure possesses the advantages of both traditional SAW sensors, which are low cost, high sensitivity and ease of use, and ZnO nanostructures, which have bio-compatibility and versatility. This device shows promising potential for portable sensors in biological and biochemical applications.

Chapter VI. ZnO Nanotip-based QCM Sensors

In this chapter we will explore another type of acoustic wave sensor, QCM device, and integrate the traditional QCM technology with the biocompatible ZnO nanotip as a sensing surface. Comparing to ZnO N-SAW, the N-QCM sensor has the following advantages: i) N-QCM is much cheaper, since the sensor template is commercially available; ii) N-QCM has simpler design and fabrication process; iii) N-QCM sensor has a much larger sensing area, which makes the study of wettability effects on sensing possible; iv) N-QCM sensor has a relative low operation frequency, requiring less complicate oscillation circuit for data acquisition and analyzing; v) N-QCM sensor can work in both liquid and gas phase.

6.1. Device Analysis

Quartz crystal microbalance (QCM) is a sensitive thickness monitor used in a variety of technological applications. With a high quality (Q) factor, typically 10,000 to 100,000 at room temperature, it is also a versatile research tool for chemistry, nanotribology, wetting transition, and superfluid transition studies. A QCM device is a piezoelectric AT-cut quartz crystal sandwiched between a pair of metal electrodes. When an AC voltage is applied to the electrodes that are connected to an oscillator, the quartz crystal starts to oscillate at its resonance frequency due to the piezoelectric effect. As a sensor, QCM has been extensively used to monitor the change in mass loading and viscoelastic properties by measuring the shift of its resonant frequency. QCM devices can operate in the range of several MHz to tens of MHz, determined by the thickness of the quartz plank. Acoustic wave transducer technology has been applied for biosensing in recent years as sensitive, accurate, cheap and portable sensors [109, 110]. QCM sensors

in biological applications have provided certain unique advantages over other biosensor technologies, namely, higher sensitivity than electrical and thermal biosensors [49, 50]. In addition, those sensors are more cost-efficient and mobile than optical biosensors [52]. Such QCM biosensors have been used to investigate the adsorption of protein on metals [111], DNA immobilization [112] and human serum albumin [113].

In this chapter, we focus on the superhydrophilic ZnO nanotip-based QCM sensors, and their applications in DNA detection. We have found that ZnO nanostructures can be made into superhydrophilic sensing surface by UV illumination. The wettability change of ZnO nanotips is utilized to improve the up-taking ability from the sample solution so that the QCM sensors use much less volume of solution, while offering higher sensitivity. It is found that the superhydrophilic ZnO nanotips-covered surface together with the significantly increased sensing surface area makes highly sensitive QCM sensors with no sacrifice of the mechanical quality factor or the stability in the resonant frequency.

Before introducing the device fabrication of our ZnO nanotip-based QCM, we first discuss the modeling of our devices.

Upon additional mass adding to the surface of a thin quartz resonator, its resonance frequency decreases. When a QCM is used for mass measurements, a quantitative relationship between the oscillation frequency shift and the added mass must be established. In 1959 Sauerbrey[114, 115] derived the first equation describing the frequency to mass relationship. In his work Sauerbrey made the assumption that for small mass changes, the added mass could be treated in the same manner as an additional mass of quartz resulting in an added thickness.

Use Sauerbrey's model to represent an uncoated oscillating QCM with a mass of M_q and a thickness of l_q . The resonant frequency (f_q) of this QCM is then simply:

$$f_q = \frac{v_q}{\lambda_q} = \frac{v_q}{2l_q} \quad (6.1)$$

where l_q is the wavelength of the propagating acoustic wave, which is twice the thickness of the QCM (l_q). v_q is the speed of the propagating wave ($v_q = l_q f_q$).

In the case of adding mass on the QCM surface, a change in the thickness of the QCM (Δl_q) will occur, which further causes a change in the oscillation frequency of the QCM (Δf_q). An increase in thickness and mass results in a decrease in the frequency in accordance with equations (6.2) and (6.3).

$$\frac{\Delta f_q}{f_q} = -\frac{\Delta l_q}{l_q} \quad (6.2)$$

$$\frac{\Delta f_q}{f_q} = -\frac{\Delta M_q}{M_q} \quad (6.3)$$

Combining equations (6.1) and (6.3),

$$\frac{\Delta f_q}{f_q} = -\left(\frac{2f_q}{\rho_q v_q A}\right) \Delta M_q \quad (6.4)$$

$$\Delta f_q = -2.26 \times 10^{-6} f_q^2 \frac{\Delta M_q}{A} \quad (6.5)$$

In equations (6.4) and (6.5) A is the area of the quartz crystal in cm^2 , ρ_q is the density of quartz (2.648 g cm^{-3}) and v_q is the speed of the propagating acoustic wave ($3.336 \times 10^5 \text{ cm s}^{-1}$). In his work Sauerbrey reported experimental mass measurements

with a 14 MHz AT-cut QCM to be accurate within 2% of values obtained using equation (6.5) for mass loadings up to $20\mu\text{g cm}^{-2}$, which ensure the accuracy of this model.

To apply the model, one needs to understand the electrical equivalent circuit of the QCM as well as the nature of interaction between the acoustical energy and matter. A quartz resonator as an electroacoustical device can be described mechanically in terms of its mass, its ability to yield elastically (shear modulus) and resistance. The resonator can also be presented as a network of lumped electrical parameters consisting of an inductor, a capacitor and a resistor (the Butterworth-Van Dyke equivalent circuit)[116].

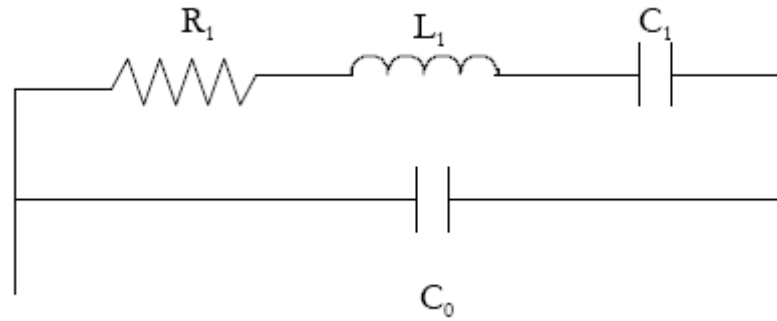


Fig. 6.1 Equivalent circuit of a quartz crystal microbalance.

In Figure 6.1, the inductor L_1 represents the inertial component (the oscillating mass), the capacitance C_1 represents the energy stored during oscillation due to the elasticity, and the resistance R_1 represents the energy dissipation due to internal friction and mechanical and acoustical losses to the mount and the surroundings. The static capacitance of the quartz and its electrodes, C_0 , is parallel to the series or the motional branch. In the series branch a fully charged capacitor C_1 immediately starts to discharge, resulting in current through the inductor L_1 . Since the inductor resistance changes in the

current by self-induction, the current continues until capacitor C_1 is fully charged with the opposite polarity. Once the charging current drops to zero, the capacitor will discharge again. If $R=0$, the repetition of this process results in electrical oscillation infinitely. If $R>0$, the oscillation will be damped with decaying amplitude until disappears completely. In the mechanical model describing the displacement of the surface of the quartz crystal in a shear mode, when the capacitor (C_1) is fully charged the potential energy and the shear displacement are at a maximum, while the kinetic energy is zero. The potential energy is completely converted to kinetic energy when the shear displacement of the quartz surface is zero. The displacement again approaches its maximum value as all the kinetic energy reverts to the potential energy. The relationship between the electrical and the mechanical models is best seen in the their equations of motion (6.6 and 6.7)[117].

$$F = m \frac{d^2 x}{dt^2} + r \frac{dx}{dt} + \frac{1}{c_m} x, \quad (6.6)$$

$$V = L_1 \frac{d^2 q}{dt^2} + R_1 \frac{dq}{dt} + \frac{1}{c_1} q, \quad (6.7)$$

where F is the force, V is the voltage and K ($K=F/V$) is the electromechanical coupling coefficient, m is the mass, r is a dissipation factor, c_m is elasticity, x is the displacement, and q is the charge. $V=IZ$ is the vector sum of the individual voltages, where Z denotes the total impedance of the circuit, X_L and X_C are the inductive and capacitive reactances, respectively.

$$Z = \sqrt{R^2 + (X_L - X_C)^2}, \quad (6.8)$$

where $X_L=\omega L$, $X_C=1/(\omega C)$

At the series resonance the impedance (Z) reaches a minimum and the inductive and

capacitive reactances become equal. $\omega_0 = \frac{1}{\sqrt{LC}}, X_L = X_C$

The admittance ($Y=1/Z$) and the admittance phase angle measured at different frequencies for a 10MHz AT-cut QCM with gold electrodes are shown in Figure 6.2 and Figure 6.3, respectively. When the phase angle approaches zero at the series resonant frequency ($f_r = 9.99088\text{MHz}$), the admittance has the maximum magnitude. The phase angle approaches zero for the second time at the parallel resonant frequency (anti-resonant frequency, $f_a = 10.017\text{MHz}$), which corresponds to the minimum admittance. At low frequencies the capacitive reactance dominates and the circuit behaves as a pure capacitor. The admittance phase angle θ is close to 90° indicating that the voltage leads the current. As the frequency approaches the resonant region, the inductive reactance becomes more pronounced. At resonance the contributions from the capacitive and the inductive reactance cancel one another, so that the phase angle becomes zero ($\theta=0^\circ$) and the impedance reaches a minimum. The admittance, on the other hand, is at its maximum. At this point the circuit behaves as a pure resistor. As the frequency increases, the admittance phase angle decreases until the circuit becomes totally inductive in nature (admittance phase angle $\theta = -90^\circ$). Further increasing of frequency also leads to resonate when the parallel inductive and capacitive reactances cancel. At parallel resonance the admittance phase angle passes through zero again and for higher frequencies goes back to 90° .

The admittance can also be plotted by its imaginary (susceptance) and real (conductance) components as shown in Figure 6.4.

The correlation between the susceptance (B) and the conductance (G) is

$$\left(G - \frac{1}{2R}\right)^2 + (B - \omega C_0)^2 = \left(\frac{1}{2R}\right)^2. \quad (6.9)$$

According to equation (6.9), the B-G curve is a circle, whose radius equals the reciprocal of the resistance of the QCM at resonance (shown in Figure 6.5).

The electrical or acoustical impedance of an added mass layer to the QCM needs to be incorporated in the equivalent circuit of the QCM, where the modified circuit is shown in Figure 6.6 as the Butterworth-Van Dyke model. Here, L_2 is the added mass, R_2 is the resistive viscosity component and C_2 is the elasticity (shear modulus) of the added mass.

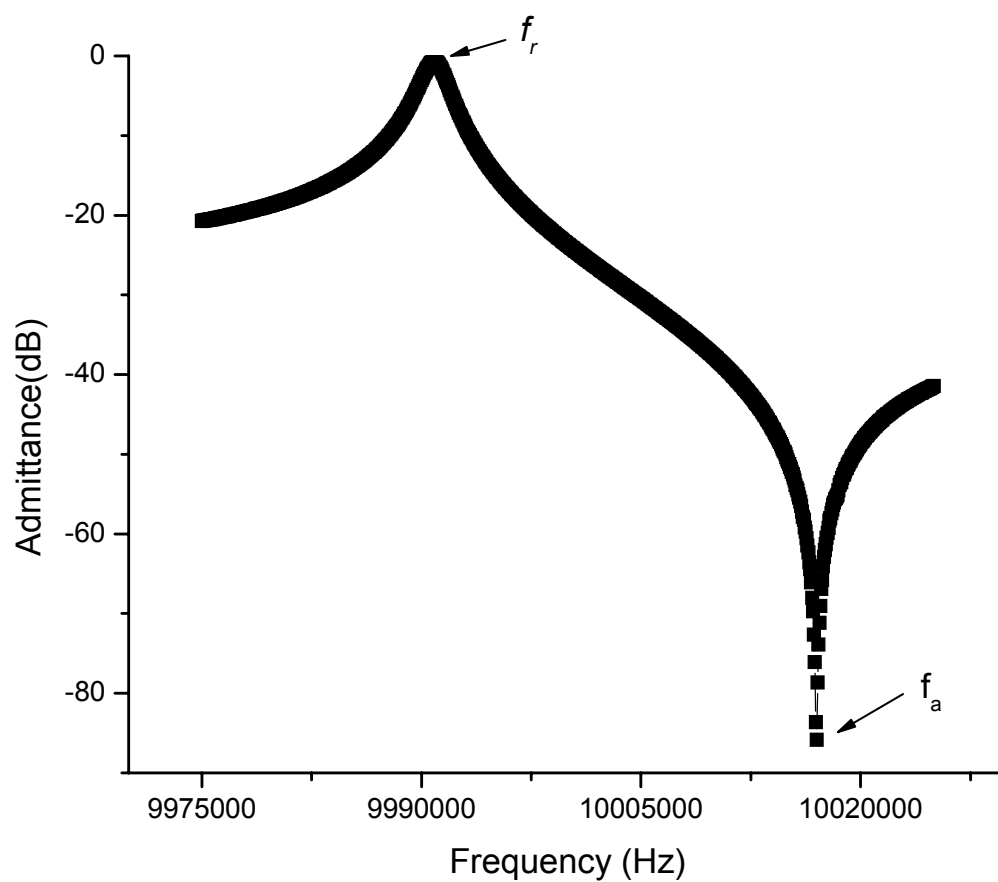


Fig. 6.2 Admittance magnitude of a 10MHz gold QCM measured by network analyzer.

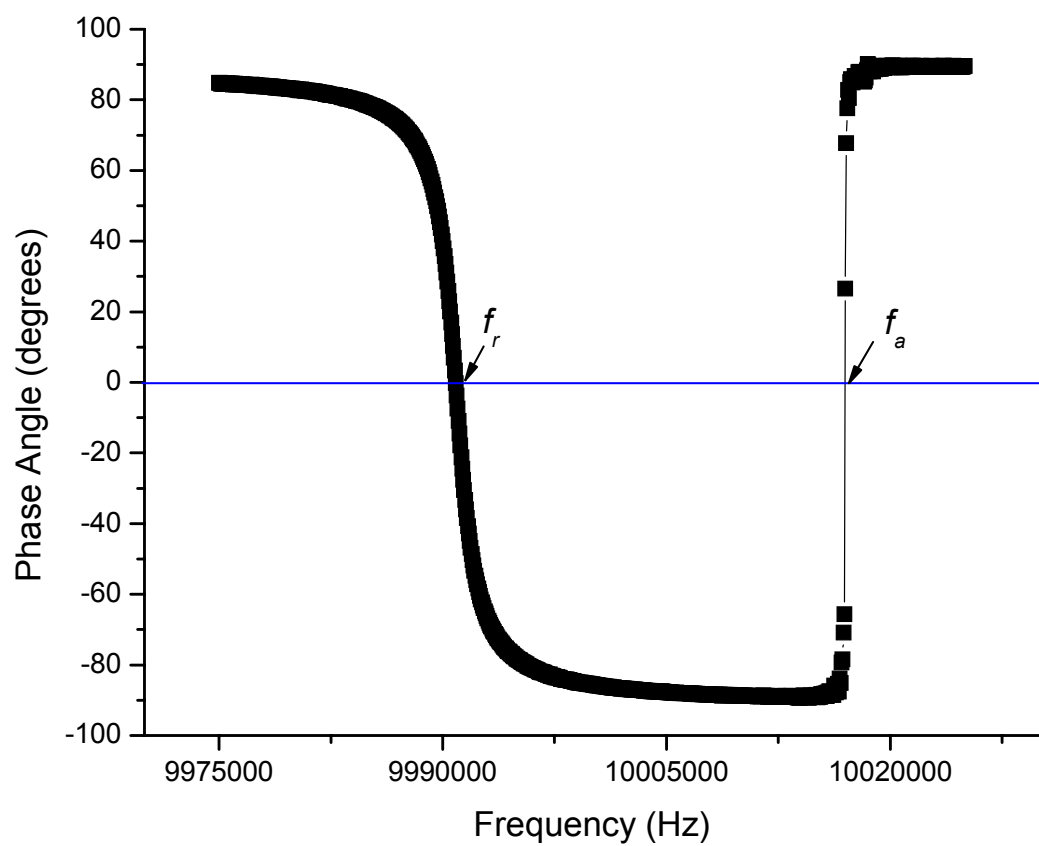


Fig. 6.3 Admittance phase angle of a 10MHz gold QCM measured by network analyzer.

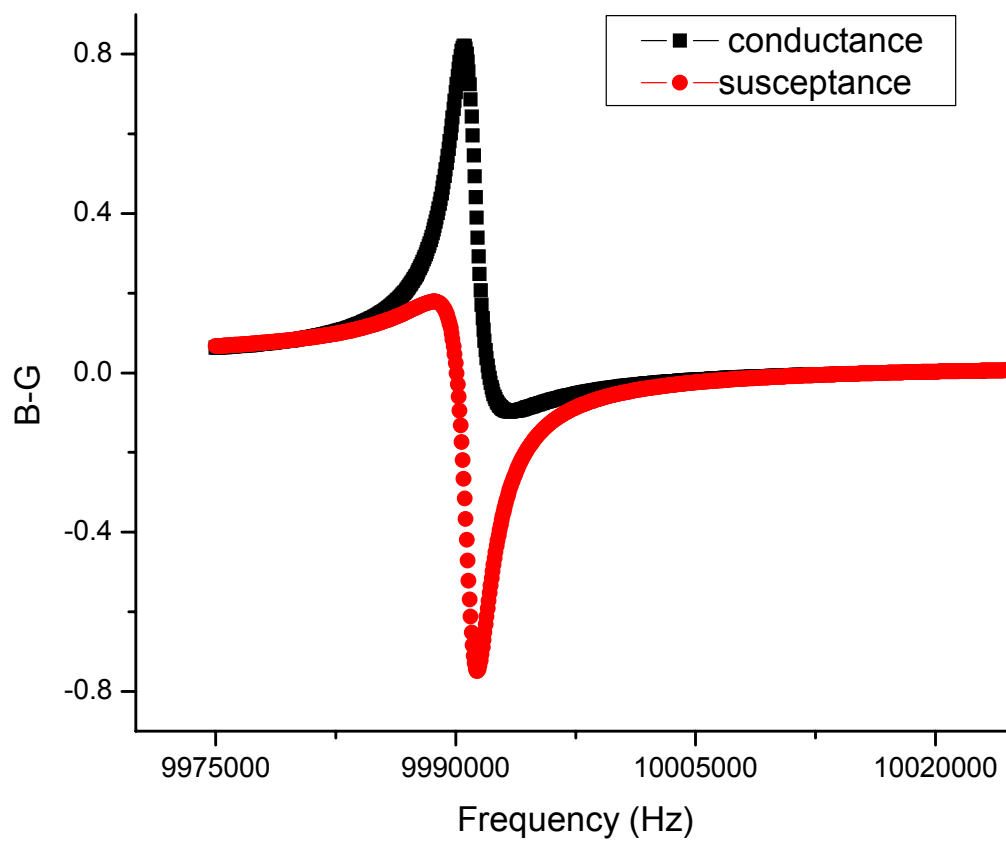


Fig. 6.4 Susceptance and conductance of a 10MHz gold QCM measured by network analyzer.

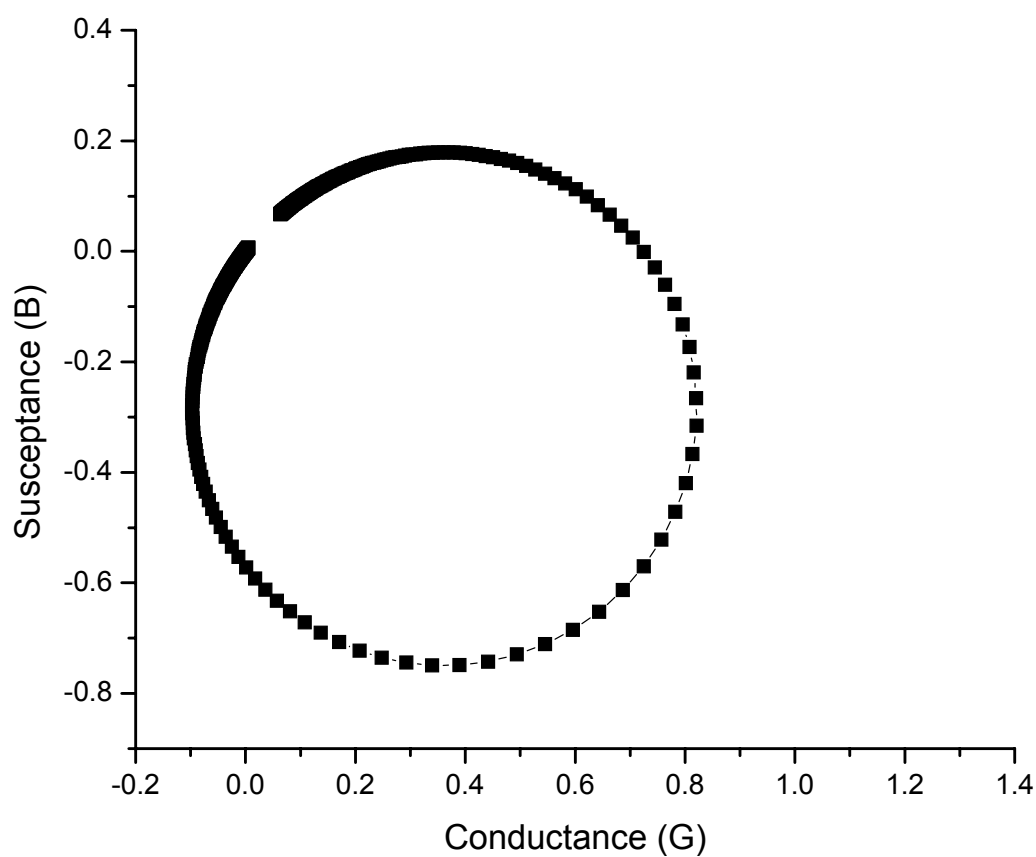


Fig. 6.5 B-G curve for a 10MHz gold QCM measured by network analyzer.

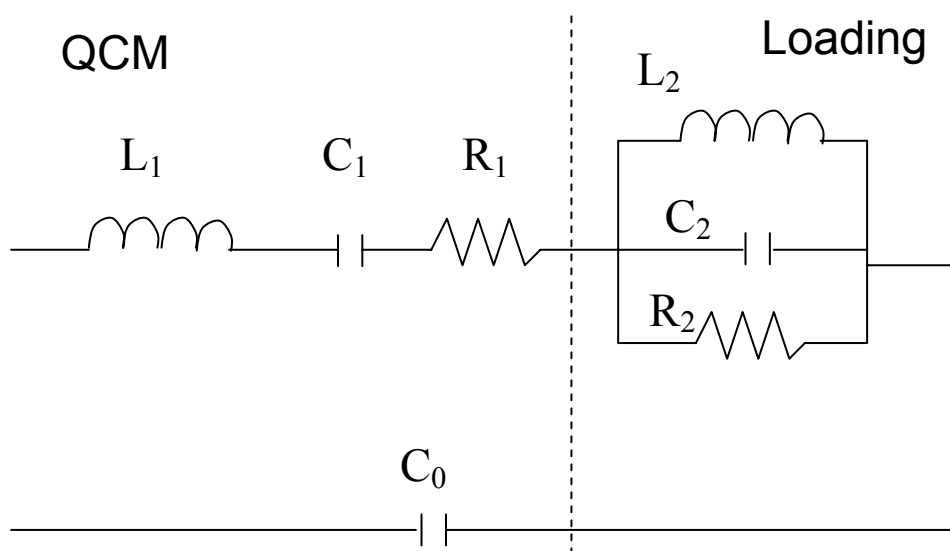


Fig. 6.6 Equivalent circuit of a mass loaded QCM.

We developed the novel ZnO N-QCM biosensor integrating ZnO nanostructures with quartz crystal microbalance. Figure 6.9 shows the schematic structure of ZnO N-QCM, with a 100nm gold layer as electrode and about 500 nm ZnO nanotips directly grown on the sensing area through a shadow mask with a diameter of 0.51 cm. The quartz substrates have a diameter of 1.37 cm and the sensing area is 0.2047 cm². The resonator frequency is about 10 MHz

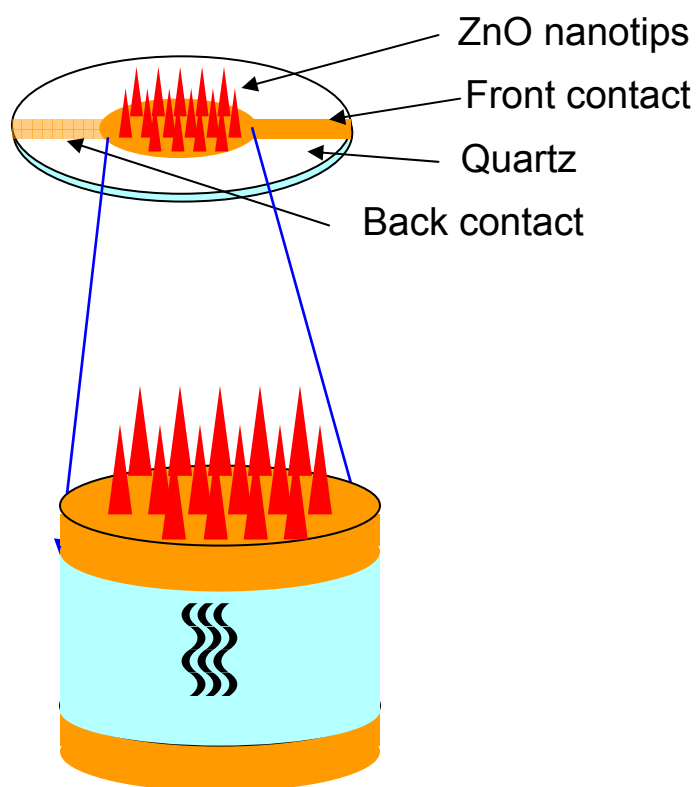


Fig 6.7 The schematic structure of a ZnO nanotips-based QCM

Figure 6.8 and Figure 6.9 show the admittance ($Y=1/Z$) spectra and the admittance phase angle measured at different frequencies for a 10MHz AT-cut ZnO nanotip-based QCM (N-QCM) and gold QCM, respectively. At the series resonance frequency (the series motional arm) the admittance reaches its maximum value. The minimum in the admittance spectrum signifies the parallel resonant frequency due to the static capacitor in parallel to the motional arm. For the uncoated QCM the admittance maximum value occurs at exactly 10MHz. This spectrum shifts down in frequency as the result of ZnO nanotip mass loading and surface charging effects. For ZnO N-QCM, when the phase angle approaches zero at the series resonant frequency ($f_r = 9.945\text{MHz}$), the admittance has the maximum magnitude. The phase angle approaches zero for the second time at the parallel resonant frequency ($f_a = 9.96588\text{MHz}$), which corresponds to the minimum admittance. Far from resonance the capacitive component of the N-QCM equivalent circuit dominates. The current and voltage are out of phase by 90 degrees. The phase angle passes through the origin at the resonant frequency, when the current and voltage are in phase with each other. Immediately after the series resonant frequency the inductive component takes over, until the phase angle becomes -90 degrees. It then passes through the origin once again at the parallel resonant frequency and returns to +90 degrees for all other frequencies. Due to the 500 nm ZnO nanotip layer, the oscillation is more damped by the ZnO nanotip and so is the admittance magnitude.

The admittance can also be plotted by its imaginary (susceptance) and real (conductance) components as shown in Figure 6.10.

For ZnO nanotip layer, the electrical admittance and the phase angle spectra for the thin films resemble that of an ideal mass. Under these conditions the oscillatory

behavior of the QCM/film composite is dominated by the QCM. If the acoustical impedance of the film is considered in establishing the frequency to mass relationship, their contributions will be negligible and the same results will be obtained as would be using Sauerbrey's relationship. Nanotips with thickness values of $0.5\mu\text{m}$ can be declared as "acoustically thin". Figure 6.11 confirms that the B-G curve is still a circle which is correct according to equation (6.9).

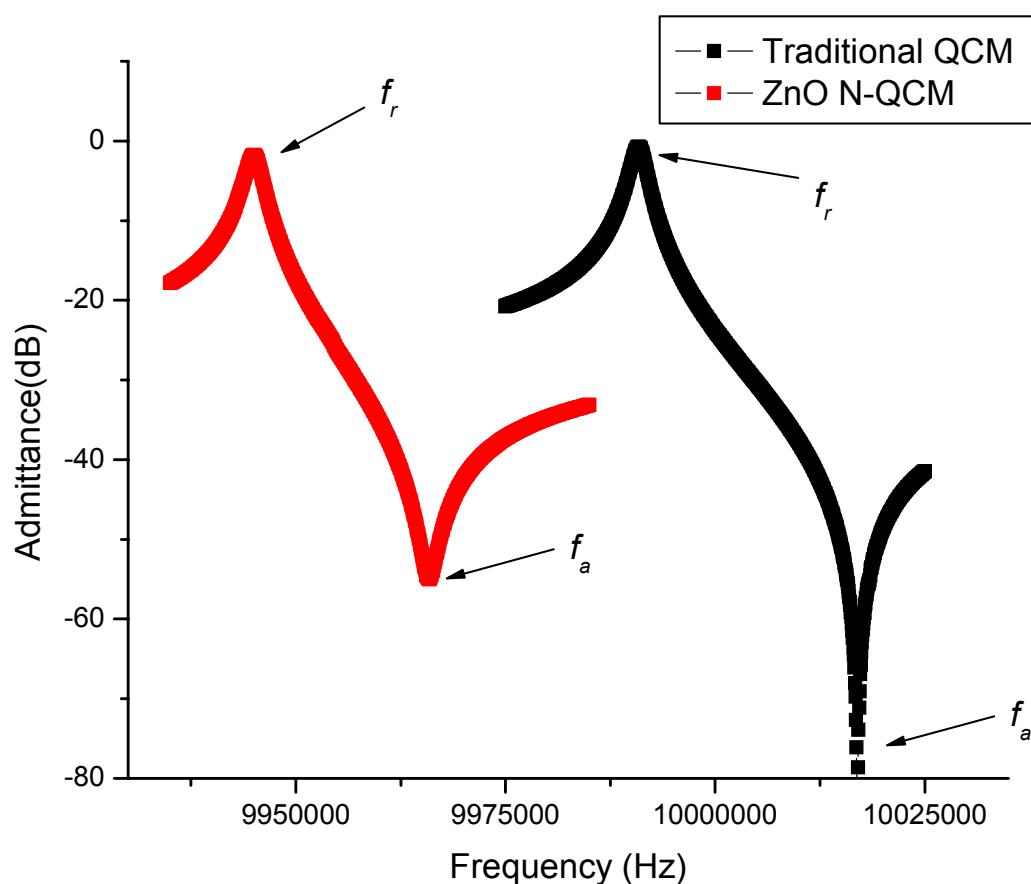


Fig. 6.8 Comparison of the admittance magnitude of a 10MHz gold QCM and ZnO N-QCM measured by network analyzer.

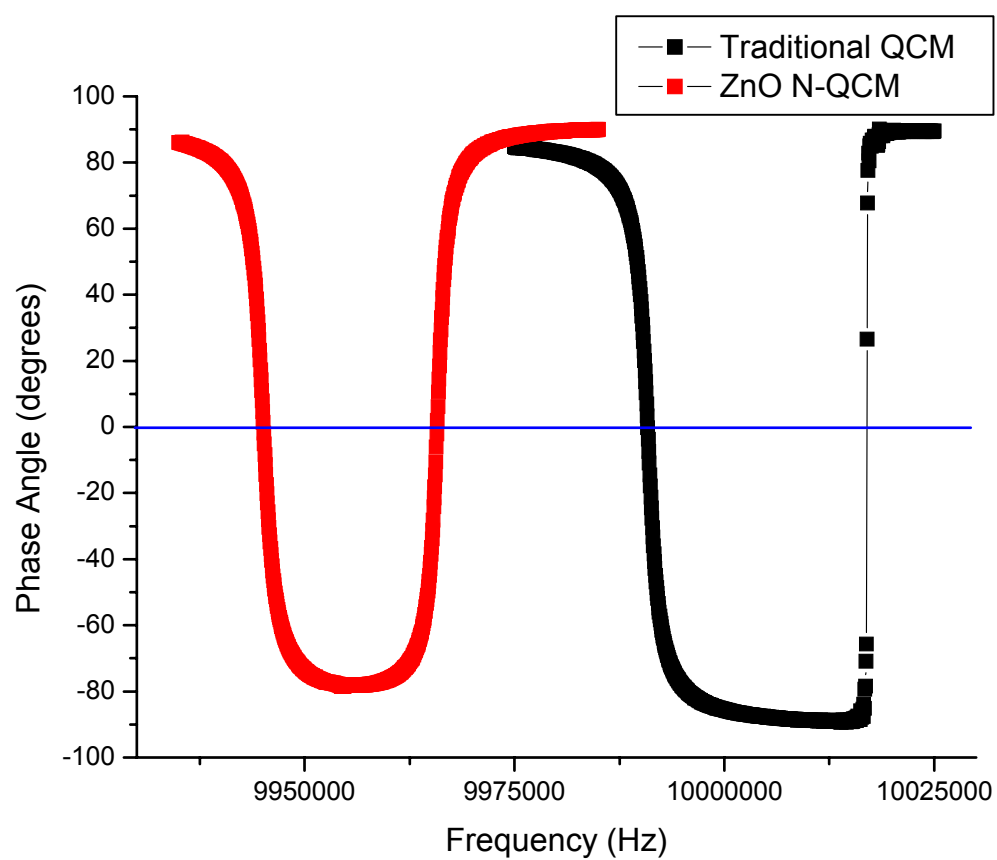


Fig. 6.9 Comparison of admittance phase angles of a 10MHz gold QCM and ZnO N-QCM measured by network analyzer.

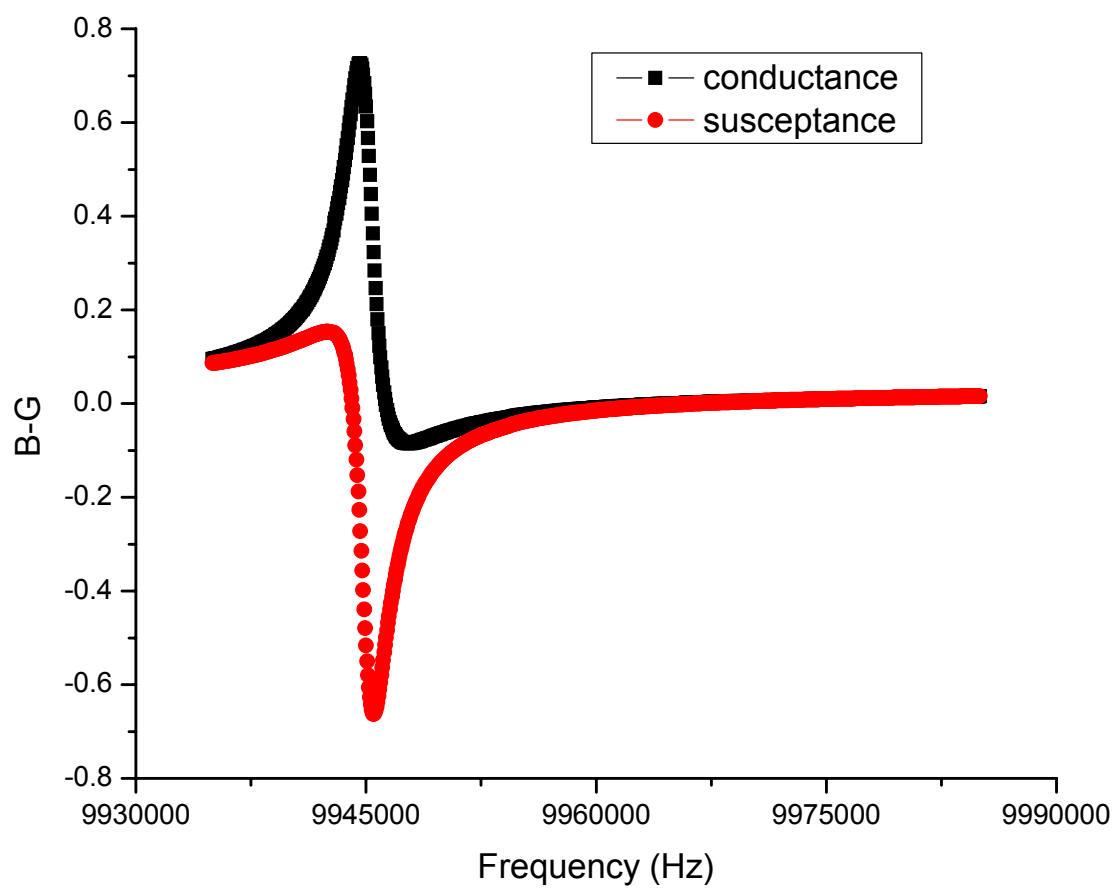


Fig. 6.10 Susceptance and conductance of a 10MHz ZnO nanotip-based quartz crystal microbalance measured by network analyzer.

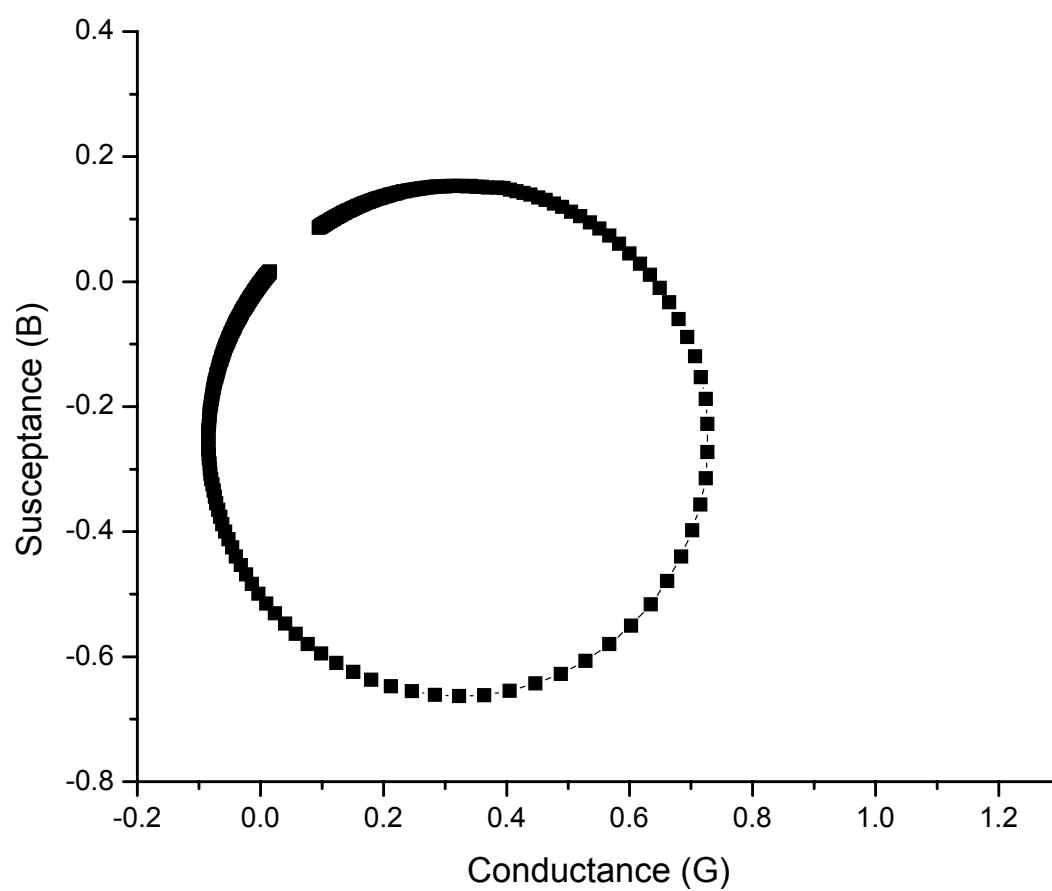


Fig. 6.11 B-G curve for a 10MHz ZnO nanotip-based quartz crystal microbalance measured by network analyzer.

6.2. Selective DNA Oligonucleotide Immobilization

We have previously demonstrated the feasibility study of the functionalization of ZnO nanotips in chapter 4.3. It has been shown that the best anchoring group in the case of ZnO nanotips is COOH. Binding studies of 3-mercaptopropionic acid to ZnO nanotips have demonstrated that binding occurs through COOH-group but not SH-group. In this section, we used the following scheme and experimental procedures to realize selective DNA immobilization on ZnO N-QCM (Figure 6.12). We choose 16-mercaptohexadecanoic acid to modify ZnO nanotips, since COOH group has been shown as the best anchoring group in chapter 4.3 and this acid has a relative long molecule for better selective binding for several-step molecule binding. After the formation of sulfhydryl surface, we introduce the pyridyl group onto the sulfhydryl surface to protect the active sulfhydryl layer. Finally the thiol-modified DNA reacts with the disulfide surface to realize a selective DNA immobilization.

Materials. 16-Mercaptohexadecanoic acid, 90% (MHDA, Aldrich); Triethanolamine hydrochloride, 99% (TEA-HCl, Aldrich); ReductacrylTM (DTT-resin, Calbiochem); AldrithiolTM-2, 98% (2,2'-dipyridyl disulfide, Aldrich); DIUF water (Fisher); Ethyl alcohol, 200 proof-absolute, Anhydrous, ACS/USP grade (Pharmco); *N,N*-dimethylformamide (DMF, Fisher); 1xTE buffer, pH 7.5 (IDTE, IDT Inc), and 1-butanol (Aldrich) were used as received. The 16 bases 5'-thio-modified DNA 5'-/5ThioMC6-D/GTGTAGCCTCAAGTG-3' (SH-ssDNA) and complementary 5'-dye(fluorescein)-modified 5'-/56-FAM/CACTTGAGGCTAACAC-3' (ssDNA-FI) DNAs were purchased from Integrated DNA Technologies, Inc. ZnO nanotips grown on c-sapphire (c-Al₂O₃) substrate by MOCVD technique were used in present studies.

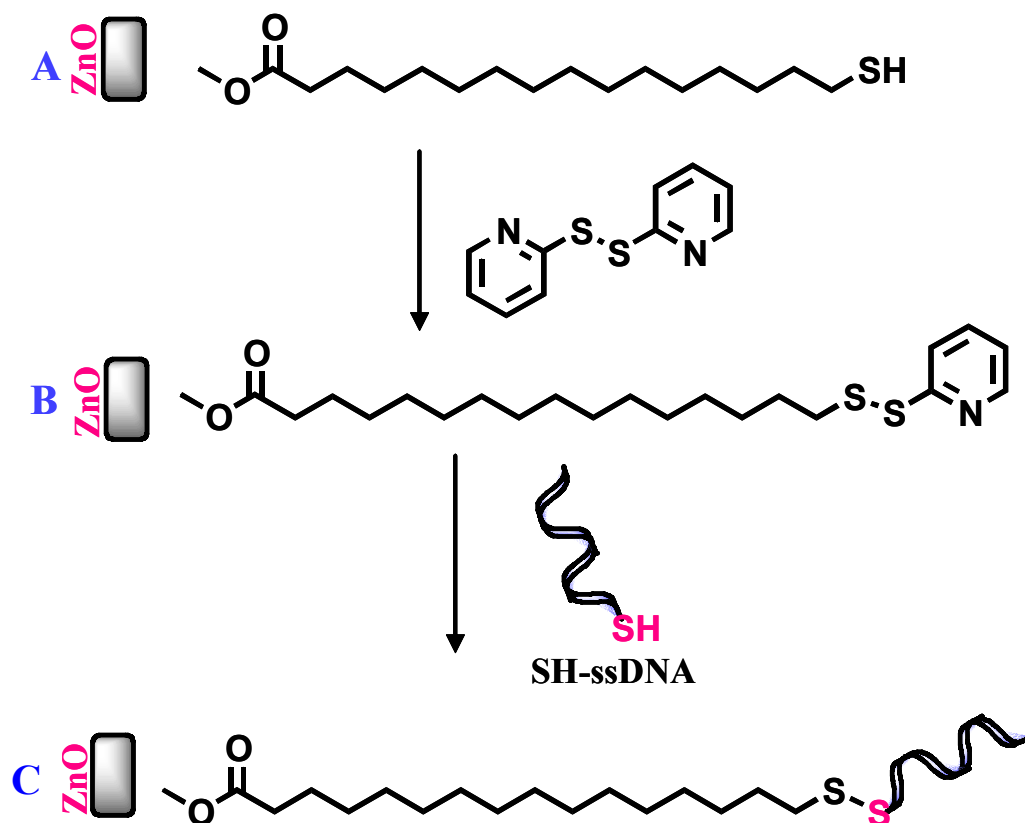


Fig 6.12 Schematic presentation of the ZnO nanotips surface modification: (A) MHDA modified surface (the formation of sulfhydryl surface); (B) an activated sulfhydryl surface with pyridyl groups; (C) an exchange reaction between disulfide surface and sulfhydryl modified DNA (SH-ssDNA).

Modification of ZnO nanotips surface. ZnO surface functionalization was performed in two ways: **(a)** in solution and **(b)** by spotting on the ZnO surface. In the case of spotting technique, more concentrated binding solutions were used (Step A and B), and 50-100 μL of binding solution was applied on 10 mm \times 10 mm surface. ZnO nanotips surface was washed with DIUF water and clean with nitrogen flow before testing.

Formation of sulfhydryl surface (A). **(a)** Each ZnO nanotips sample was immersed in 5 mM of MHDA (in ethanol) solution overnight (12-15 h) or **(b)** 10 mM MHDA in (1-butanol) solution was applied on ZnO surface for 4-6 hours, in the sealed chamber. The sample was then rinsed thoroughly and immersed into pure solvent for 15 minutes to remove physisorbed molecules.

Introduction of pyridyl group onto sulfhydryl surface (B). **(a)** The thiol surface was immersed into a 10 mM 2,2'-dipyridyl disulfide in a 1:1 mixture of 0.1 M TEA buffer solution (pH 8.0):DMF for 2 h at RT. TEA buffer was prepared by dissolving 1.86 g TEA-HCl in 80 mL water (pH 8 was adjusted with 1 M NaOH and volume was adjusted to 100 mL with water). **(b)** 20 mM 2,2'-dipyridyl disulfide in a 1:1 mixture of 0.1 M TEA buffer solution (pH 8.0):DMF was applied for 2 h at RT.

The reaction of thiol-modified DNA with the disulfide surface (C). Reduced SH-ssDNA was used immediately. **(a)** The disulfide surface was immersed into 25 μM (or 10 μM) SH-ssDNA in TE buffer for 3 h at RT. **(b)** 25 μM (or 120 μM) SH-ssDNA in TE buffer was applied for 3 h at RT in the sealed chamber.

After each reaction step the samples were thoroughly rinsed with a solvent (ethanol, DMF or buffer) and dried under nitrogen flow.

An alternative ZnO nanotips surface modification route was proposed (Figure 6.13). The compound **3** is bound to the surface through COOH group leaving N-succinimide group on the surface (step A) which can easily react with NH₂-modified ssDNA (step B).

Modification of ZnO nanotips surface. ZnO nanotips samples (~10 mm × 10 mm) were used to modify ZnO surface before using it as a biosensor.

Formation of N-CPDS-surface (A). ZnO nanotips samples were immersed in 10 mM of N-CPDS (in THF) solution overnight (12-15 h). The sample was then rinsed thoroughly with pure solvent to remove physisorbed molecules.

Reaction of amino-modified DNA with NHS-ester (B). 25 μM NH₂-ssDNA in HEPES buffer (pH ~8) (DMF-40%) was applied on the obtained ZnO samples after Step A, for 4 h at RT.

After each reaction step the samples were thoroughly rinsed with a solvent (THF, DIUF water) and dried under nitrogen flow.

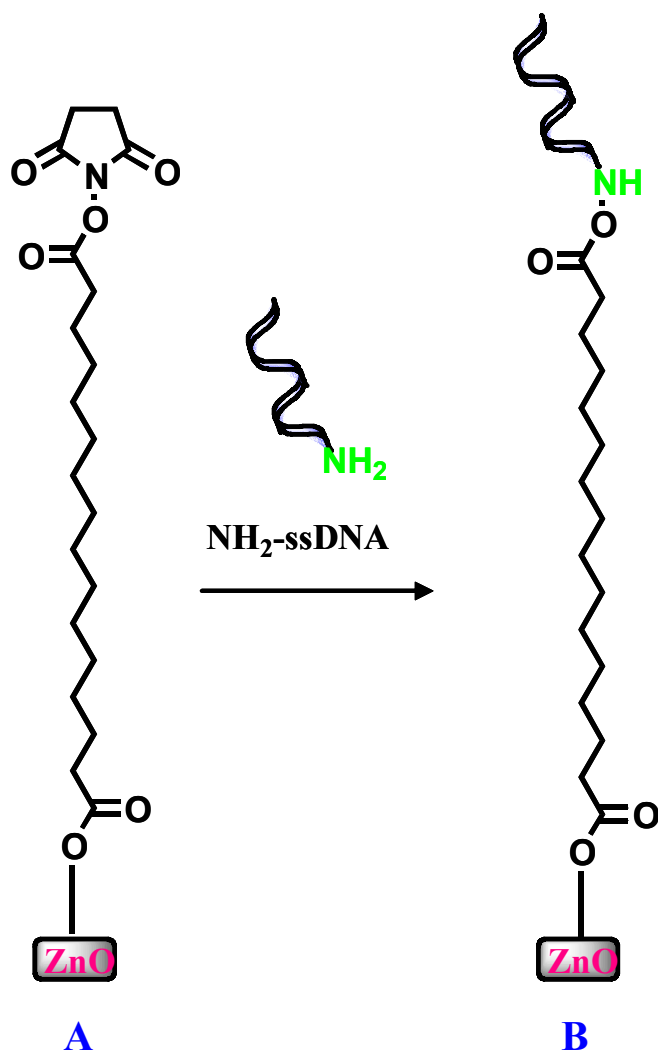


Fig 6.13 Schematic presentation of the ZnO nanotips surface modification. (A) Formation of N-CPDS-surface; (B) reaction of amino-modified DNA with NHS-ester.

6.3. Sensor Testing

The characterization of the QCM sensors is also conducted using an HP 8573D Network Analyzer (Agilent Technologies, Palo Alto, CA), as shown in Figure 6.14. The forward transmission parameter S_{21} of the QCM sensors is measured at each harmonics (1st, 3rd, 5th and 7th), then the collected data is analyzed using MATLAB and Origin. All the measurements are performed at room temperature.

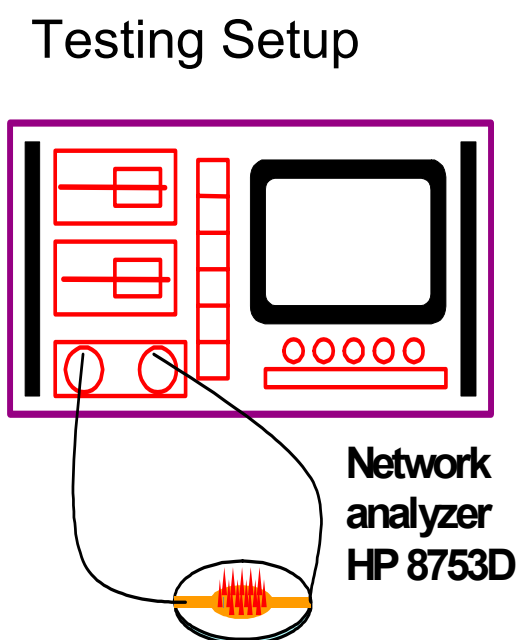


Fig 6.14 The N-QCM device characterization test setup.

Contact Angles

The contact angles of three types of QCM sensors were measured in the method described in Chapter 4. As shown in Table 6.1, the contact angle (CA) of gold sensing surface of a traditional QCM is 85° , while the CA of the hydrophobic ZnO nanotips is

128°; the volume of DI water used to fully cover the 0.2047 cm² sensing area is 16 µl for the gold film and 20 µl for the hydrophobic nanotips.

After shining with broad band ultra-violet light, the CA of hydrophobic ZnO nanotips decreased to around 0° and became superhydrophilic. This change resulted in a dramatic decrease of liquid consumption on the sensing area. Only 0.5µl water was need for the hydrophilic nanotips, which is less than 1/30 of the amount required for a traditional QCM sensor.

Table 6.1. Liquid Consumption on the 0.2047 cm² Sensing Area of QCM Sensors with Different Wetting Properties

	Traditional QCM	Nanotip-based QCM (hydrophobic)	Nanotip-based QCM (hydrophilic)
Contact Angle	85°	128°	~0°
Liquid Consumption	16 µ l	20 µ l	0.5 µ l

Frequency Responses

Performance of the three types of QCM sensors were then compared by measuring the resonant frequency shift in idle condition, DI water and DNA solution testing. The base frequency of the QCM is around 9.99546 MHz.

The forward transmission S₂₁ spectra of ZnO nanotip-based QCM sensors with different wetting properties are compared to the traditional QCM sensor at 1st, 3rd, 5th, 7th

harmonics (Figure 6.15). The frequency shifts between traditional sensor and nanotip-based sensor is $\Delta f_1 = 62.5$ kHz for the 1st harmonics, $\Delta f_3 = 186$ kHz for the 3rd harmonics, $\Delta f_5 = 309$ kHz for the 5th harmonics, and $\Delta f_7 = 428$ kHz for the 7th harmonics. The higher the resonant order, the larger the frequency shifts.

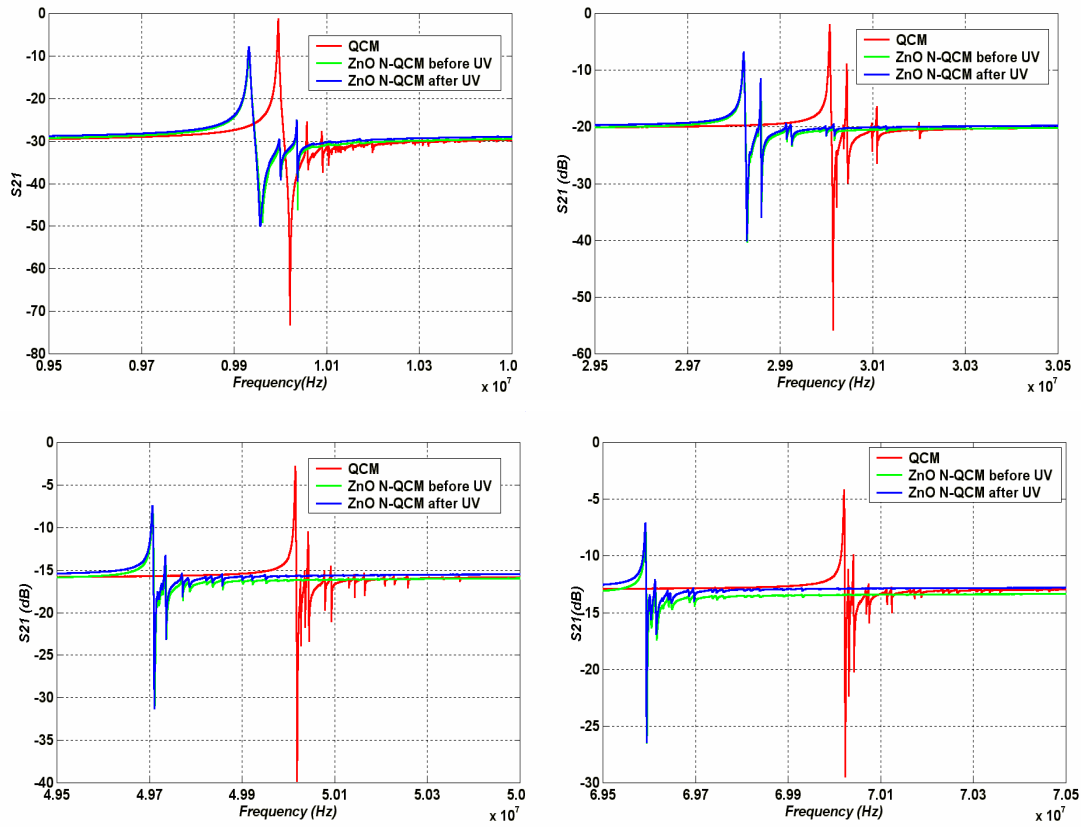


Fig. 6.15 Forward transmission parameter (S_{21}) of the ZnO nanotip-based QCM devices compared to traditional QCM device at the 1st, 3rd, 5th, 7th harmonics.

Table 6.2 lists the resonant frequency shifts using the three QCM sensors when loading DI water. For each sensor, we are only comparing the frequency responses before and after liquid loading or DNA immobilizations. In other words, only the frequency

shifts of ZnO nanotip based QCM due to the additional mass loading has been tested and compared. The mass loading of ZnO nanotips have been excluded by resetting the reference point. A fixed volume of 1 μl water is used for all sensors. For all of the four harmonics, both nanotip-base QCM sensors have increased frequency shifts over the traditional sensor. And the hydrophilic sensor has even larger shifts than the hydrophobic one. In comparison, the frequency shifts of the hydrophobic and hydrophilic nanotip-based sensors increase with the harmonics order. The shift for the 7th harmonic is 25 times larger than the shift for the 1st harmonic in the hydrophobic nanotip-sensor; while that ratio is 6.6 in the hydrophilic nanotip-sensor. The frequency shift for the 1st harmonic in the hydrophilic nanotip-sensor is ten times larger than the shift in the traditional sensor, while this difference increases to 41 times for the 7th harmonics. The frequency shift testing confirms that the superhydrophilic nanotip-based QCM sensors are more sensitive than the traditional sensor and the hydrophobic nanotip-based QCM sensors, especially at higher order harmonics.

Table 6.2. Frequency Shift of Different Harmonics between the Tradition, Hydrophobic and Hydrophilic ZnO QCM Sensors.

Harmonics	Traditional QCM	Nanotip-based QCM (hydrophobic)	Nanotip-based QCM (hydrophilic)
1 st	0.6 kHz	0.7 kHz	6.2 kHz
3 rd	1 kHz	3 kHz	19 kHz
5 th	1 kHz	9 kHz	32 kHz
7 th	1 kHz	19 kHz	41 kHz

DNA Immobilization

As an example for real biological applications, we used those QCM sensors to test DNA solution. The QCM sensors were functionalized by directly immobilizing the DNA oligonucleotide on the active sensing surface (See chapter 5, Figure 5.4). When 2 μl of DNA oligonucleotide solution (5'-AGAAAATCTTAGTGTC-3') at the concentration of 20 ng/ μl was applied to the sensing area of superhydrophilic ZnO nanotip-based QCM sensor, 0.3 kHz frequency shift was detected. While on traditional QCM, no observable frequency shift was detected after subtracting the DI water effects. The sensitivity of the nanotip sensor, is calculated to be 153.6 cm^2/g using equation (6.22) based on Sauerbrey's model, which is 10 times larger than the theoretic data of the traditional QCM.

$$S = \frac{\Delta f / f_c}{\Delta m / A} \quad (6.22)$$

Selective DNA Immobilization by Surface Modifications

Beyond the direct immobilization, selective DNA immobilization has been realized on ZnO N-QCM with surface modifications. The experimental procedure was explained in last section 6.2.

We compared the ZnO N-QCM hydrophobic sensing surface with superhydrophilic surface. In the first 3-step approach to modify the surface (Figure 6.12), the superhydrophilic ZnO nanotip sensing surface has been successfully sulfhydryled and functionalized with pyridyl group (see Figure 6.16). At 1st harmonic of N-QCM, 3.65 kHz frequency shift and 14.7 dB insertion loss were induced due to the formation of sulfhydryl surface. Another 16.05 kHz frequency shift and additional 3.94dB insertion loss due to the Introduction of pyridyl group onto sulfhydryl surface. However, the selective immobilization of SH-ssDNA was not able to be calibrated due to the extra mass loss of the buffer solution. In the system of hydrophobic ZnO sensing surface, there are no obvious frequency and insertion loss changes during the 3-step functionalization (Figure 6.17).

To reduce the buffer effect during the functionalization, we used the alternative 2-step approach to selectively immobilize DNA (shown in Figure 6.13). In this case, selective DNA immobilization has been successfully realized through the reaction of amino-modified DNA with NHS-ester. Figure 6.18 shows the forward transmission frequency responses of ZnO N-QCM devices in the 2-step functionalization at 1st harmonic peak. The N-QCM started with a hydrophobic surface and then changed into superhydrophilic surface using UV illumination to get a better surface modification. This transition resulted in a 0.667 kHz frequency shift and about 1.5 dB additional insertion

loss in transmission spectra, mainly due to the surface charging change on ZnO nanotips after the UV illumination. The N-CPDS surface has been formed on ZnO nanotips and confirmed by a dramatically frequency response spectrum changes. About 16 kHz frequency shift and a 19.5 dB additional insertion loss were observed on N-QCM, which corresponds to around 1066 ng functionalization molecules based on the sensitivity we demonstrated before. The frequency spectra also confirmed the successful selective DNA immobilization. In the first harmonic peak of the N-QCM, 10.47 kHz frequency shifts results from around 1396 ng amino-modified DNA with selective binding on the ZnO nanotip sensing surface.

6.4. Summary

This chapter demonstrated ZnO N-QCM sensors by selectively growing ZnO single crystalline nanotips on the top gold electrode of QCM devices using MOCVD. We achieved superhydrophilic ZnO nanotips with UV shining on the sensing surface. The novel QCM sensors with ZnO nanotips as the sensing elements were fabricated for testing DNA oligonucleotide (5'-AGAAAATCTTAGTGTC-3') solution. The QCM sensor with superhydrophilic nanotips showed 10 times, 20 times, 30 times, and 40 times increases of response frequency for the 1st, 3rd, 5th, and 7th harmonics over those of the traditional QCM for the same amount of liquid loading. The sensitivity of the nanotip-based QCM is 153.6 cm²/g, which is 10 times larger than the traditional QCM. In addition, the liquid consumption of the superhydrophilic nanotip-based QCM is only 3% of the traditional QCM. The functionalization of ZnO nanotips have been demonstrated, which makes the selective biological sensing possible on the ZnO N-QCM. Our results

show that QCM sensors using ZnO nanotips have significantly improved the sensitivity, and are especially suitable for precious biological sample testing.

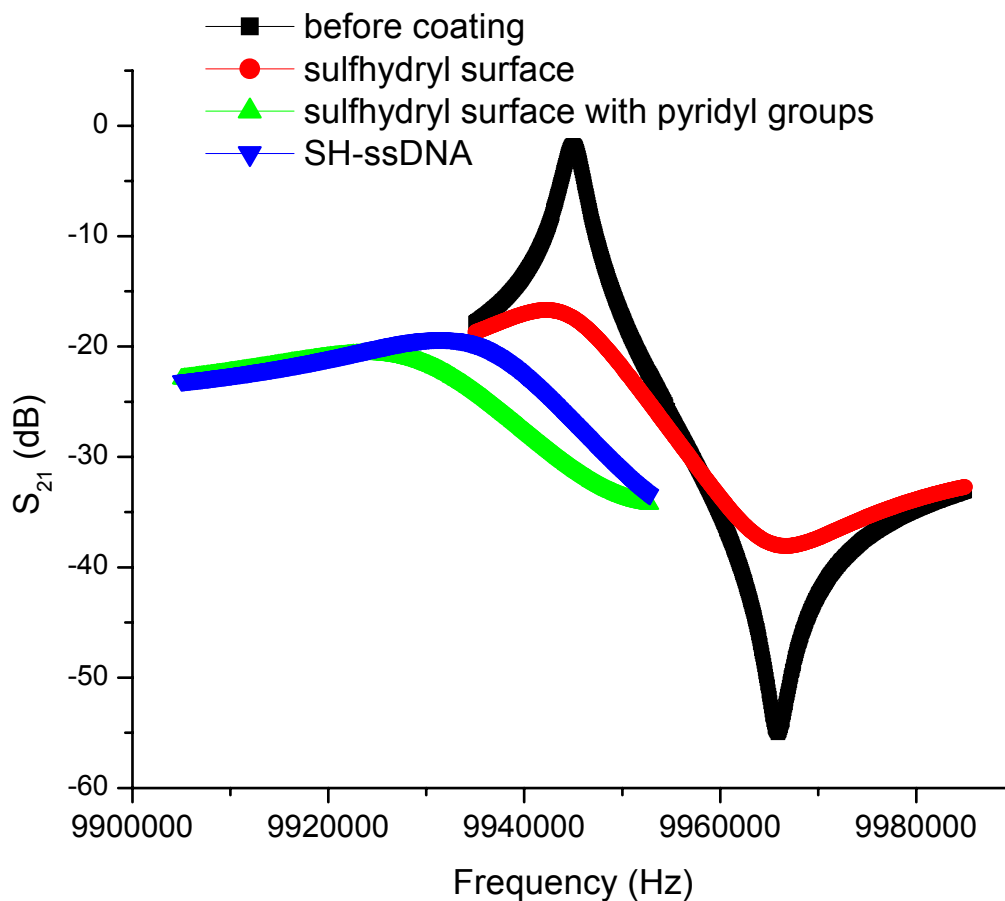


Fig. 6.16 Forward transmission parameter (S_{21}) of the superhydrophilic ZnO nanotip-based QCM devices in 3-step functionalization.

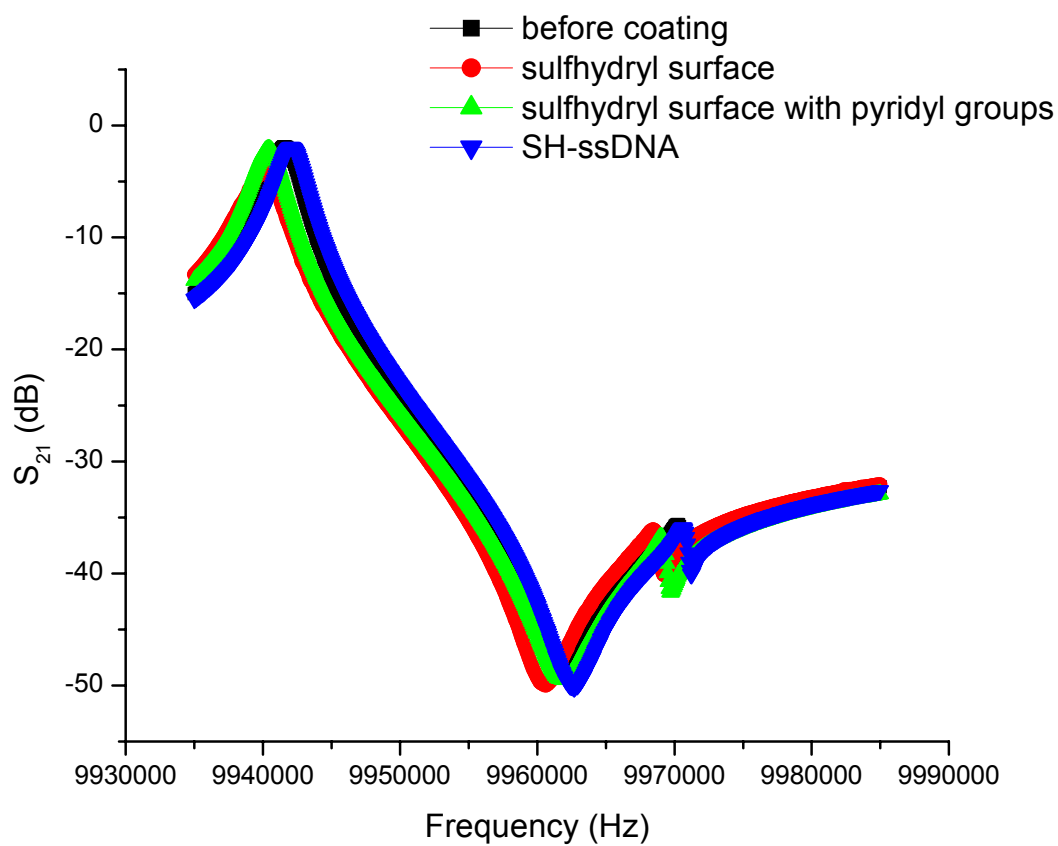


Fig. 6.17 Forward transmission parameter (S_{21}) of the hydrophobic ZnO nanotip-based QCM devices in 3-step functionalization.

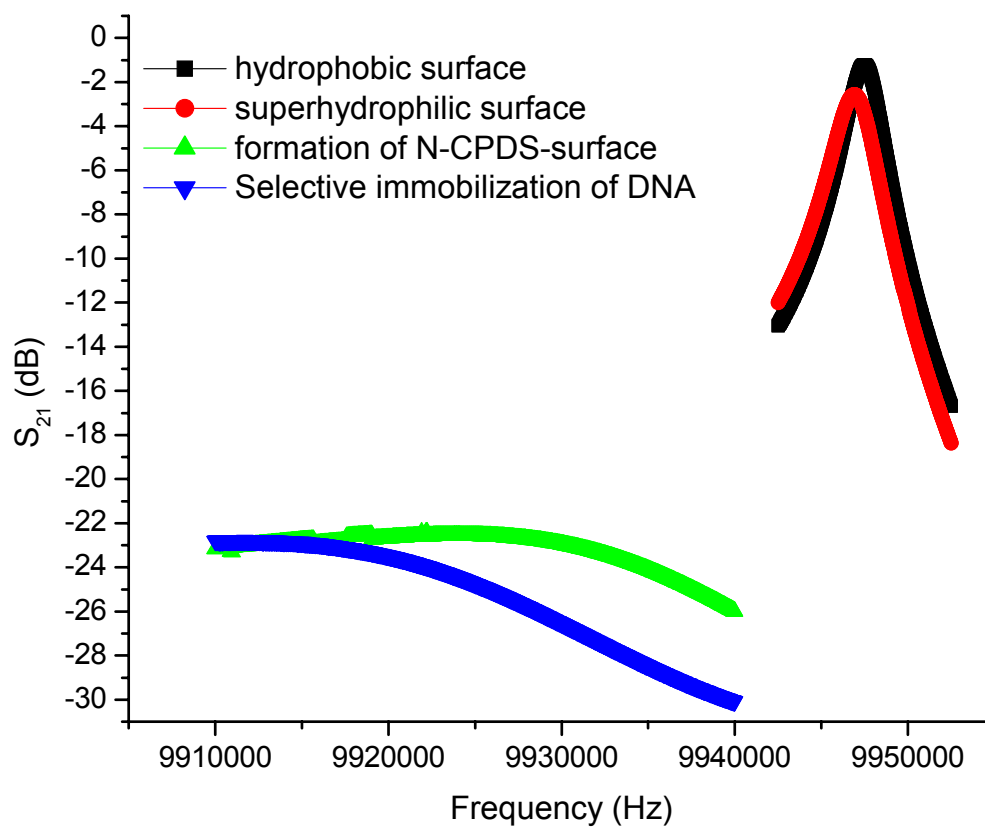


Fig. 6.18 Forward transmission parameter (S_{21}) of the ZnO nanotip-based QCM devices in 2-step functionalization at 1st harmonic.

Chapter VII Conclusion and Future Work

7.1. Conclusion

Recent progress in nanoscale science and technology has led to the development of novel nanosensors which have faster response and higher sensitivity than the conventional planar sensor configurations.

In this work, we have demonstrated two types of acoustic wave sensors based on ZnO nanostructures. One is the ZnO nanotip-based surface acoustic wave (SAW) sensor and the other is ZnO nanotip-based quartz crystal microbalance (QCM) sensor.

Using the MOCVD technique, high quality ZnO nanotips were grown on various substrates, such as Si, quartz, glass, gold and c-sapphire. The single crystal quality of nanotip was confirmed using X-ray diffraction and scanning electron microscopy. The uniform ZnO nanotip array aligns with their c-axis perpendicular to the substrate surface. The photoluminescence spectrum of the ZnO nanotips shows strong near bandedge transition with insignificant deep level emission, confirming their good optical property.

We have demonstrated the control of the wettability transitions of ZnO nanotips and films grown on various substrates. It is found that the ZnO nanostructured surface greatly enhances the wetting effects in comparison with the epitaxial ZnO film with flat surface due to the roughness effects. The unprecedentedly fast transition rates between superhydrophilic and hydrophobic status have been demonstrated. Those wetting property controls are very important for the sensitivity and liquid consumption of our sensors.

In order to realize the selective sensing in our biosensor system, we have demonstrated that ZnO nanotips can be functionalized with bifunctional linkers and made

a comparison between the binding properties of ZnO nanotips with ZnO epitaxial films. The binding experiments indicate that the carboxylic acid group (COOH) is a suitable anchoring group for binding to the ZnO nanotips but that the number and position of the COOH groups, the acidity of the anchoring group, and solution pH also play a role in the binding. The bound samples were stable as no changes in the IR, UV, and fluorescence spectra were observed in 1 year old samples. The potentially useful, but flexible, bifunctional linker is 3-mercaptopropionic acid since it did bind by the COOH group, leaving the SH group available for selective sensing in the biological applications. The ZnO nanotip provided excellent binding surfaces when compared to ZnO films. This opens the possibility to develop ZnO nanotips functionalized with a variety of redox-active molecules or biomolecules, eventually leading to a new ZnO nanotip-based integrated, multimode multifunctional sensor technology, which combines different sensing mechanisms (acoustic, electrical, optical, biological, etc.) to achieve higher accuracy and sensitivity and has a broad impact in biological and environmental applications.

A novel SAW biosensor using a ZnO nanotip array for enhanced DNA immobilization has been demonstrated. This biosensor integrates a ZnO nanotip array with a SAW device fabricated on 128° Y-cut LiNbO₃. The ZnO nanotip array is used for immobilizing the bio-receptor, while the SAW device functions as the transducer to detect the mass loading effect resulting from the analyte-receptor reaction. The ZnO nanotip arrays are shown enhance DNA immobilization by a factor of 200 compared to smooth surface ZnO films. This immobilization enhancement of ZnO nanotips is attributed to the fact that ZnO nanotips have large surface area and lower binding energy

compared with planar surface. The sensor is functionalized by immobilizing first strand DNA oligonucleotide on the ZnO nanotip array, after which the device can selectively sense its complementary secondary strand DNA oligonucleotide. This device structure possesses the advantages of both traditional SAW sensors, which are low cost, high sensitivity and ease of use, and ZnO nanostructures, which have bio-compatibility and versatility. This device shows promising potential for portable sensors in biological and biochemical applications.

In the ZnO N-QCM sensor, the uniform ZnO nanotip arrays were selectively grown on the top of a gold electrode of the QCM by MOCVD. The ZnO nanotip coated QCM sensor shows a 10-time larger frequency shift than that of regular QCM sensors, when measuring the same DNA oligonucleotide (5'-AGAAAATCTTAGTGTC-3') solution. In addition, the hydrophilic behaviors of the nanotip array significantly reduce the required liquid volume for effective detection. 0.5 μ l solution fully covers the QCM sensor area (0.2047 cm²), while a minimum of 16 μ l liquid is required to cover a flat surface of the conventional QCM. ZnO nanotips show superhydrophilicity with a contact angle of $\sim 0^\circ$ under UV illumination. It is found that the superhydrophilic ZnO nanotips-covered surface together with the significantly increased sensing surface area makes highly sensitive QCM sensors with no sacrifice of the mechanical quality factor or the stability in the resonant frequency. The superhydrophilic sensor surface significantly boosts the solution taking up ability; therefore, enhances the sensitivity of the QCM sensor. The functionalization of ZnO nanotips have been demonstrated, which makes the selective biological sensing possible on the ZnO N-QCM. Our results show that QCM

sensors using ZnO nanotips have significantly improved the sensitivity, and are especially suitable for precious biological sample testing.

7.2. Suggestions for Future Work

Even with extensive research effort on ZnO based sensors in recent years, this field is still in the early stage of development. In order to understand the origin of the observed biological sensing ability of ZnO nanostructures to provide guideline for future biosensor device applications, further work is necessary except the tasks accomplished in this work.

The following work is recommended for the future research and development related to ZnO and MgZnO nanotips based on the present progress:

1. Current N-SAW sensor is based on general SAW modes which consider only the acoustic propagation in the layered planar structures. The complexity of our device is increased by the fact that the acoustic propagation will penetrate into the top ZnO nanotip layer. The nanotip layer will have different effect on the acoustic wave such as nanoscale grain boundary, and scattering. Those effects will influence the device performance such as operation frequency and insertion loss. A comprehensive model needs to take all the major factors into account. Sensitivity can be increased by optimizing the SAW sensor design and the hybridization process. A narrower bandwidth SAW delay line is suggested.
2. Based on the special properties of ZnO nanostructures, this N-SAW and N-QCM sensors can be developed to be a multifunctional biosensor. It can integrate different sensing methods, such as SAW, BAW, optical, electrical conductivity and fluorescence, into a single device.

3. The ZnO nanotips provide excellent binding surfaces when compared to ZnO films, but the fact that the nanotips are etched at low pH ($\text{pH} \leq 4$) limits their use. Our experiments suggest that linkers with acidic functional groups “dissolve” the ZnO nanotips. Increased resistance to acids was obtained by alloying ZnO with MgO (5-10%). MgZnO nanotips are a novel material that exhibited increased stability toward acidic linkers, while staying identical to the ZnO-N in other respects. Alloyed films could therefore be employed with a larger variety of binding groups and at wider pH ranges. This opens the possibility to develop MgZnO nanotips functionalized with a variety of biomolecules, eventually leading to a new MgZnO-based integrated multimode multifunctional sensor technology, which combines different sensing mechanisms (acoustic, electrical, optical, biological, etc.) to achieve higher accuracy and sensitivity and has a broad impact in biological and environmental applications.
4. The wettability of ZnO nanotips can be reversibly controlled by UV illumination and oxygen annealing. Further study would be done to expedite the transition rate even more. Hence the instant wettability control can be realized for the applications in the microfluidic handling techniques. For example, it can be used as a liquid-based optical switch, where droplet can be manipulated by optical illuminations. Those smart surface based microfluidic system will be integrated in a sensor-on-chip system in the future.
5. A variety of very important practical applications could be explored in the ZnO N-SAW and N-QCM biosensors. With further study of surface functionalization and modifications, those sensor templates can be widely used in health care

(medical and genetic diagnostics), environmental monitoring (control of pollution and detection of hazardous chemicals), food analysis (detection of ingredients, contamination etc.) and detection of biological warfare agents.

Reference

- [1] O. Ambacher, M. Eickhoff, G. Steinhoff, M. Hermann, L. Gorgens, and V. Werss, "Electronics and sensors based on pyroelectric AlGa_N/Ga_N heterostructures," *Proc ECS*, vol.214, pp.27, 2002.
- [2] R. Mehandru, B. Luo, B. S. Kang, J. Kim, F. Ren, S. J. Pearton, C. C. Fan, G. T. Chen, and J. I. Chyi, "AlGa_N/Ga_N HEMT based liquid sensors," *Solid State Electronics* vol.48, pp.351, 2004.
- [3] S. J. Pearton, B. S. Kang, S. Kim, F. Ren, B. P. Gila, C. R. Abernathy, J. Lin, and S. N. G. Chu, "Ga_N-based diodes and transistors for chemical, gas, biological and pressure sensing," *Journal of Physics: Condensed Matter*, vol.16, pp.R961, 2004.
- [4] J. Schalwig, G. Muller, M. Eickhoff, O. Ambacher, and M. Stutzmann, "Gas sensitive Ga_N/AlGa_N-heterostructures," *Sensors and Actuators B*, vol.87, pp.425, 2002.
- [5] G. Steinhoff, M. Hermann, W. J. Schaff, L. F. Eastmann, M. Stutzmann, and M. Eickhoff, "pH response of Ga_N surfaces and its application for pH-sensitive field-effect transistors," *Applied Physics Letters*, vol.83, pp.177, 2003.
- [6] W. P. Kang and C. K. Kim, "Catalyst-adsorptive oxide-semiconductor gas sensors," *Sensors and Actuators B* vol.14, pp.682, 1993.
- [7] D. C. Look, J. W. Hemsky, and J. R. Sizelove, "Residual Native Shallow Donor in ZnO," *Physical Review Letters*, vol.82, pp.2552, 1999.
- [8] B. G. Miller, T. W. Traut, and R. V. Wolfenden, "A Role for Zinc in OMP Decarboxylase, an Unusually Proficient Enzyme," *Journal of the American Chemical Society*, vol.120, pp.2666, 1998.
- [9] S. M. Sze, *Semiconductor Sensors*. New York: Wiley-Interscience, 1994.
- [10] R. M. White, "A sensor classification scheme," *IEEE Transaction on Ultrasonics, Ferroelectrics and Frequency Control*, vol.34, pp.124, 1987.
- [11] R. Axel, "The molecular logic of smell," *Scientific American*, vol.273, pp.154, 1995.
- [12] A. Keller and L. B. Vosshall, "Human olfactory psychophysics," *Current Biology*, vol.14, pp.R875, 2004.
- [13] C. D. Natalea, A. Macagnanoa, G. Repolea, G. Saggioa, A. D'Amicoa, R. Paolesseb, and T. Boschi, "The exploitation of metalloporphyrins as chemically interactive material in chemical sensors," *Materials Science and Engineering:C*, vol.5, pp.209, 1998.
- [14] D. R. Walt, "Fiber optic imaging sensors," *Accounts of Chemical Research*, vol.31, pp.261, 1998.
- [15] G. Vishnoi, M. Morisawa, and S. Muto, "A New Plastic Optical Fiber Sensor for Oxygen Based on Fluorescence Enhancement," *Optical Review*, vol.5, pp.13, 1998.
- [16] O. S. Wolfbeis, "Fiber-optic chemical sensors and biosensors," *Analytical Chemistry*, vol.76, pp.3269, 2004.
- [17] J. Xu, Q. Pan, Y. Shun, and Z. Tian, "Grain size control and gas sensing properties of ZnO gas sensor," *Sensors and Actuators B*, vol.66, pp.277, 2000.
- [18] H. L. Tuller, "Electronic and Mechanical Properties of Materials," MIT, boston 2001.

- [19] L.-Y. Chen, G. W. Hunter, P. G. Neudeck, D. Knight, C. C. Liu, and Q. H. Wu, "SIC based gas sensors," NASA Technical Memorandum 113125, 1996.
- [20] A. Arbab, A. Spetz, I. Lundstrom, F. J. G. Monreal, and B. J. G. Gaudo, "Gas sensors for high-temperature operation based on metal oxide silicon carbide (MOSiC) devices," Eurosensors Conference, vol.15, pp.19, San Sebastian, Spain, 1992.
- [21] M. S. Freund and N. S. Lewis, "A chemically diverse conducting polymer-based electronic nose," Proceedings of the National Academy of Sciences, vol.92, pp.2652, 1995.
- [22] H. P. Lang, M. K. Baller, F. M. Battiston, J. Fritz, R. Berger, J.-P. Ramseyer, P. Fornaro, E. Meyer, H.-J. Guntherodt, J. Brugger, U. Drechsler, H. Rothuizen, M. Despont, P. Vettiger, C. Gerber, and J. K. Gimzewski, "The nanomechanical NOSE," IEEE International MEMS '99 Twelfth IEEE International Conference on Micro Electro Mechanical Systems, pp.9, Orlando, FL 1999.
- [23] T. A. Dickinson, J. White, J. S. Kauer, and D. R. Walt, "A chemical-detecting system based on a cross-reactive optical sensor array," *Nature*, vol.382, pp.697, 1996.
- [24] N. A. Rakow and K. S. Suslick., "A colorimetric sensor array for odor visualization," *Nature*, vol.406, pp.710, 2000.
- [25] C. H. Contag. Stanford University.
- [26] K. Shah and R. Weissleder, "Molecular optical imaging: applications leading to the development of present day therapeutics," *NeuroRx*, vol.2, pp.215, 2005.
- [27] A. Ballato, "Piezoelectricity: History and New Thrusts," Proceeding of Ultrasonics Symposium, vol.1, pp.575, 1996.
- [28] D. Morgan, *Surface-Wave Devices for Signal Processing*. Amsterdam: Elsevier, 1991.
- [29] J. G. Gualtieri, J. A. Kosinski, and A. Ballato, "Piezoelectric materials for SAW applications," Proceedings IEEE 1992 Ultrasonics Symposium, 1992.
- [30] T. Shiosaki, "Growth and applications of piezoelectric and ferroelectric thin films," Proceedings IEEE 1990 Ultrasonics Symposium, pp.537, 1990.
- [31] H. Wohltjen, D. Ballantine, R. White, S. Martin, A. Ricco, E. Zellers, and G. Frye, *Acoustic Wave Sensors—Theory, Design, and Physico-Chemical Applications*. New York: Academic, 1997.
- [32] M. Schweyer, J. Hilton, J. Munson, and J. Andle, "A novel monolithic piezoelectric sensor," Proceedings of Ultrasonic Symposium, vol.1, pp.371, 1997.
- [33] S. J. Martin, G. C. Frye, J. J. Spates, and M. A. Butler, "Gas sensing with acoustic devices," Proceedings of Ultrasonic Symposium, vol.1, pp.423, 1996.
- [34] M. Sweyer, J. Andle, D. McAllister, L. French, and J. Vetelino, "An acoustic plate mode sensor for aqueous mercury," Proceedings of Ultrasonic Symposium, vol.1, pp.355, 1996.
- [35] L. Raleigh, Proc. R. Soc. Lond. A, Math Phys. Sci., vol.17, pp.4, 1885.
- [36] H. Wohltjen, "Surface acoustic wave microsensors," Proceedings of 4th International Solid-State Sensors and Actuators Conference, pp.471, 1987.
- [37] J. Grate, S. Martin, and R. White, "Acoustic wave microsensors," *Anal. Chem.*, vol.65, pp.940, 1993.

- [38] W. Bowers, R. Chuan, and T. Duong, "A 200 MHz surface acoustic wave resonator mass microbalance," *Rev. Sci. Instrum.*, vol.62, pp.1624, 1991.
- [39] K. A. Vetelino, P. R. Story, R. D. Mileham, and D. W. Galipeau, "Improved Dew Point Measurements Based on a SAW Sensor," *Sensors and Actuators, B*, vol.35, pp.91, 1996.
- [40] J. Cheeke, N. Tashtoush, and N. Eddy, "Surface Acoustic Wave Humidity Sensor Based on the Changes in the Viscoelastic Properties of a Polymer Film," *Proc. Ultrasonics Symposium*, vol.1, pp.449, 1996.
- [41] E. Radeva and I. Avramov, "Humidity Sensing Properties of Plasma Polymer Coated Surface Transverse Wave Resonators," *Proc. Ultrasonics Symposium*, vol.1, pp.509, 1998.
- [42] L. Reindl, C. C. W. Ruppel, A. Kirmayr, N. Stockhausen, and M. A. Hilhorst, "Passive Radio Requestable SAW Water Content Sensor," *Proc Ultrasonics Symposium*, vol.1, pp.461, 1999.
- [43] M. Vellekoop and B. Jakoby, "A Love-Wave Ice Detector," *Proc Ultrasonics Symposium*, vol.1, pp.453, 1999.
- [44] H. Wohltjen and R. Dessy, "Surface Acoustic Wave Probe for Chemical Analysis I. Introduction and Instrument Design," *Analytical Chemistry*, vol.51, pp.1458, 1979.
- [45] T. Nakamoto, K. Nakamura, and T. Moriizumi, "Study of Oscillator-Circuit Behavior for QCM Gas Sensor," *Proc Ultrasonics Symposium*, vol.1, pp.351, 1996.
- [46] E. Staples, "Electronic Nose Simulation of Olfactory Response Containing 500 Orthogonal Sensors in 10 Seconds," *Proc Ultrasonics Symposium*, vol.1, pp.417, 1999.
- [47] G. Kovacs and M. Vellekoop, "Theoretical comparison of sensitivities of acoustic shear wave modes for biochemical sensing in liquids," *Applied Physics Letters*, vol.61, pp.639, 1992.
- [48] E. Gizeli, M. Liley, C. Lowe, and H. Vogel, "Antibody binding to a functionalized supported lipid layer: A direct acoustic immunosensor," *Anal. Chem.*, vol.69, pp.4808, 1997.
- [49] A. Q. Contractor, T. N. Sureshkumar, R. Narayanan, S. Sukeerthi, R. Lal, and R. S. Srinivasa, "Conducting polymer-based biosensors," *Electrochimica Acta*, vol.39, pp.1321, 1994.
- [50] L. Ghindilis, P. Atanasov, M. Willkins, and E. Willkins, "Immunosensors: electrochemical sensing and other engineering approaches," *Biosensors & Bioelectronics*, vol.13, pp.113, 1998.
- [51] M. Minunni, M. Mascini, G. Guilbault, and B. Hock, "The quartz-crystal microbalance as biosensor - a status-report on its future," *Analytical Letters*, vol.28, pp.749, 1995.
- [52] A. Neef, R. Schafer, C. Beimfohr, and P. Kampfer, "Fluorescence based rRNA sensor systems for detection of whole cells of *Saccharomonospora* spp. and *Thermoactinomyces* spp.," *Biosensors & Bioelectronics*, vol.18, pp.565, 2003.
- [53] V. I. Anisimkin, M. Penza, A. Valentini, F. Quaranta, and L. Vasanelli, "Detection of combustible gases by means of a ZnO-on-Si surface acoustic wave (SAW) delay line," *Sensors and Actuators B*, vol.23, pp.197, 1995.

- [54] S. J. Martin, K.S.Schweizer, S. S. Schwartz, and R. L. Gunshor, "Vapor sensing by means of a ZnO-on-Si surface acoustic wave resonator," *Proc. IEEE Ultrasonics Symposium*, vol.1, pp.207, 1984.
- [55] Y. Cui, Q. Wei, H. Park, and C. M. Lieber, "Nanowire nanosensors for highly sensitive and selective detection of biological and chemical species," *Science*, vol.293, pp.1289, 2001.
- [56] Y. Cui and C. M. Lieber, "Functional nanoscale electronic devices assembled using silicon nanowire building blocks," *Science*, vol.291, pp.851, 2001.
- [57] M. Haupt, A. Ladenburger, R. Sauer, K. Thonke, R. Glass, W. Roos, J. P. Spatz, H. Rauscher, S. Riethmülle, and M. Moller, "Ultraviolet-emitting ZnO nanowhiskers prepared by a vapor transport process on prestructured surfaces with self-assembled polymers," *J. Appl. Phys.*, vol.93, pp.6252, 2003.
- [58] S. Muthukumar, H.Sheng, J. Zhong, Z. Zhang, N. W. Emanetoglu, and Y. Lu, "Selective MOCVD growth of ZnO nanotips," *IEEE Transactions on Nanotechnology*, vol.2, pp.50, 2003.
- [59] W. I. Park, D. H. Kim, S.-W. Jung, and G.-C. Yi, "Metalorganic vapor-phase epitaxial growth of vertically well-aligned ZnO nanorods," *Appl. Phys. Lett*, vol.80, pp.4232, 2002.
- [60] W. I. Park, Y. H. Jun, S. W. Jung, and G.-C. Yi, "Excitonic emissions observed in ZnO single crystal nanorods," *Appl. Phys. Lett*, vol.82, pp.964, 2003.
- [61] J. Zhong, S.Muthukumar, Y. Chen, Y. Lu, H. M. Ng, W. Jiang, and E. L. Garfunkel, "Ga-doped ZnO single-crystal nanotips grown on fused silica by metalorganic chemical vapor deposition," *Applied Physics Letters*, vol.83, pp.3401, 2003.
- [62] J. J. Wu and S. C. Liu, "Low-Temperature Growth of Well-Aligned ZnO Nanorods by Chemical Vapor Deposition," *Advanced Materials*, vol.14, pp.215, 2002.
- [63] Y. C. Kong, D. P. Yu, B. Zhang, and S. Q. Feng, "Ultraviolet-emitting ZnO nanowires synthesized by a physical vapor deposition approach," *Appl. Phys. Lett*, vol.78, pp.407, 2001.
- [64] Y. K. Tseng, I. N. Lin, K. S. Liu, T. S. Lin, and I. C. Chen, "Low-temperature growth of ZnO nanowires," *Journal of Materials Research*, vol.18, pp.714, 2003.
- [65] J. J. Wu and S. C. Liu, "Catalyst-Free Growth and Characterization of ZnO Nanorods," *Journal of Physical Chemistry B*, vol.106, pp.9546, 2002.
- [66] A. Wei, X. W. Sun, J. X. Wang, Y. Lei, X. P. Cai, C. M. Li, Z. L. Dong, and W. Huang, "Enzymatic glucose biosensor based on ZnO nanorod array grown by hydrothermal decomposition," *Appl. Phys. Lett.*, vol.89, pp.123902, 2006.
- [67] F. Zhang, X. Wang, S. Ai, Z. Sun, Q. Wan, Z. Zhu, Y. Xian, L. Jin, and K. Yamamoto, "Immobilization of uricase on ZnO nanorods for a reagentless uric acid biosensor," *Analytica Chimica Acta*, vol.519, pp.155, 2004.
- [68] A. Dorfman, N. Kumar, and J.-i. Hahm, "Highly Sensitive Biomolecular Fluorescence Detection Using Nanoscale ZnO Platforms," *Langmuir*, vol.22, pp.4890, 2006.
- [69] A. Zangwill, *Physics at Surfaces*: Cambridge University Press, 1988.
- [70] R. N. Wenzel, "Resistance of solid surfaces to wetting by water," *Industrial and Engeneering Chemistry*, vol.28, pp.988, 1936.

- [71] X. Feng, L. Feng, M. Jin, J. Zhai, L. Jiang, and D. Zhu, "Reversible Super-hydrophobicity to Super-hydrophilicity Transition of Aligned ZnO Nanorod Films," *Journal of American Chemical Society*, vol.126, pp.62, 2004.
- [72] Y. Li, W. Cai, G. Duan, B. Cao, F. Sun, and F. Lu, "Superhydrophobicity of 2D ZnO ordered pore arrays formed by solution-dipping template method," *Journal of Colloid and Interface Science*, vol.287, pp.634, 2005.
- [73] R. D. Sun, A. Nakajima, A. Fujishima, T. Watanabe, and K. Hashimoto, "Photoinduced Surface Wettability Conversion of ZnO and TiO₂ Thin Films," *J. Phys. Chem. B*, vol.105, pp.1984, 2001.
- [74] R. Wang, K. Hashimoto, A. Fujishima, M. Chikuni, E. Kojima, A. Kitamura, M. Shimohigoshi, and T. Watanabe, "Light-induced amphiphilic surfaces," *Nature*, vol.388, pp.431, 1997.
- [75] R. Wang, N. Sakai, A. Fujishima, T. Watanabe, and K. Hashimoto, "Studies of Surface Wettability Conversion on TiO₂ Single-Crystal Surfaces," *J. Phys. Chem. B*, vol.103, pp.2188, 1999.
- [76] E. Galoppini, "Linkers for anchoring sensitizers to semiconductor nanoparticles," *Coord. Chem. Rev.*, vol.248, pp.1283, 2004.
- [77] O. Taratula, E. Galoppini, D. Wang, D. Chu, Z. Zhang, H. Chen, G. Saraf, and Y. Lu, "Binding Studies of Molecular Linkers to ZnO and MgZnO Nanotip Films," *J. Phys. Chem. B*, vol.110, pp.6506, 2006.
- [78] R. Argazzi, C. A. Bignozzi, T. A. Heimer, F. N. Castellano, and G. J. Meyer, "Enhanced Spectral Sensitivity from Ruthenium(II) Polypyridyl Based Photovoltaic Devices," *Inorg. Chem.*, vol.33, pp.5741, 1994.
- [79] A. H.-L. Goff, S. Joiret, and P. Falaras, "Raman Resonance Effect in a Monolayer of Polypyridyl Ruthenium(II) Complex Adsorbed on Nanocrystalline TiO₂ via Phosphonated Terpyridyl Ligands," *J. Phys. Chem. B*, vol.103, pp.9569, 1999.
- [80] K. Keis, C. Bauer, G. Boschloo, A. Hagfeldt, K. Westermark, H. Rensmo, and H. Siegbahn, "PES Studies of Ru(dcbpyH₂)₂(NCS)₂ Adsorption on Nanostructured ZnO for Solar Cell Applications," *J. Photochem. Photobiol. A*, vol.148, pp.57, 2002.
- [81] D. P. Strommen, P. K. Mallick, G. D. Danzer, R. S. Lumpkin, and J. R. Kincaid, "Normal-coordinate analyses of the ground and 3MLCT excited states of tris(bipyridine)ruthenium(II)," *J. Phys. Chem. B*, vol.94, pp.1357, 1990.
- [82] M.-C. Daniel and D. Astruc, "Gold Nanoparticles: Assembly, Supramolecular Chemistry, Quantum-Size-Related Properties, and Applications toward Biology, Catalysis, and Nanotechnology," *Chem. Rev.*, pp.293, 2004.
- [83] C. Le'vy-Cle'ment, R. Tena-Zaera, M. A. Ryan, A. Katty, and G. Hodes, "CdSe-sensitized p-CuSCN/Nanowire n-ZnO heterojunctions," *Adv. Mater.*, vol.17, pp.1512, 2005.
- [84] T. Tshuruoka, K. Akamatsu, and H. Nawafune, "Synthesis, Surface Modification, and Multilayer Construction of Mixed-Monolayer-Protected CdS Nanoparticles," *Langmuir* vol.20, pp.11169, 2004.
- [85] K. Ogata, T. Hama, K. Hama, K. Koike, S. Sasa, M. Inoue, and M. Yano, "Characterization of alkanethiol/ZnO structures by x-ray photoelectron spectroscopy," *Appl. Surf. Sci.*, vol.241, pp.146, 2005.

- [86] I. Gillaizeau-Gauthier, F. Odobel, M. Alebbi, R. Argazzi, E. Costa, A. C. Bignozzi, P. Qu, and G. J. Meyer, "Phosphonate-Based Bipyridine Dyes for Stable Photovoltaic Devices," *Inorg. Chem.*, vol.40, pp.6073, 2001.
- [87] M. Nilsing, S. Lunell, P. Persson, and L. Ojamae, "Phosphonic acid adsorption at the TiO₂ anatase (101) surface investigated by periodic hybrid HF-DFT computations," *Surf. Sci.*, vol.582, pp.49, 2005.
- [88] K. Keis, J. Lindgren, S. E. Lindquist, and A. Hagfeldt, "Studies of the Adsorption Process of Ru Complexes in Nanoporous ZnO Electrodes," *Langmuir*, vol.16, pp.4688, 2000.
- [89] R. Helmy and Y. A. Fadeev, "Self-Assembled Monolayers Supported on TiO₂: Comparison of C₁₈H₃₇SiX₃ (X = H, Cl, OCH₃), C₁₈H₃₇Si(CH₃)₂Cl, and C₁₈H₃₇PO(OH)₂," *Langmuir* vol.18, pp.8924, 2002.
- [90] D. Li, A. M. Ratner, and J. T. Marks, "Chromophoric self-assembled multilayers. Organic superlattice approaches to thin-film nonlinear optical materials," *J. Am. Chem. Soc.*, vol.112, pp.7389, 1990.
- [91] J. Lin, A. J. Siddiqui, and M. R. Ottenbrite, "Surface modification of inorganic oxide particles with silane coupling agent and organic dyes," *Polym. Adv. Technol.*, vol.12, pp.285, 2001.
- [92] D. Wang, R. Mendelsohn, E. Galoppini, P. G. Hoertz, R. A. Carlisle, and M. G. J., "Excited State Electron Transfer from Ru(II) Polypyridyl Complexes Anchored to Nanocrystalline TiO₂ through Rigid-Rod Linkers," *J. Phys. Chem. B*, vol.108, pp.16642, 2004.
- [93] P. G. Hoertz, R. A. Carlisle, M. G. J., D. Wang, P. Piotrowiak, and E. Galoppini, "Organic Rigid-Rod Linkers for Coupling Chromophores to Metal Oxide Nanoparticles," *Nano Lett.*, vol.3, pp.325, 2003.
- [94] M. Lamberto, C. Pagba, P. Piotrowiak, and E. Galoppini, "Synthesis of novel rigid-rod and tripodal azulene chromophores," *Tetrahedron Lett.*, vol.46, pp.4895, 2005.
- [95] D. Wang, J. M. Schlegel, and E. Galoppini, "Synthesis of rigid-rod linkers to anchor chromophores to semiconductor nanoparticles," *Tetrahedron*, vol.58, pp.6027, 2002.
- [96] S. Muthukumar, Y. Chen, J. Zhong, F. Cosandey, Y. Lu, and T. Siegrist, "Metalorganic chemical vapor deposition and characterizations of epitaxial Mg_xZn_{1-x}O (0 ≤ x ≤ 0.33) films on r-sapphire substrates," *J. Cryst. Growth*, vol.261, pp.316, 2004.
- [97] S. Muthukumar, J. Zhong, Y. Chen, Y. Lu, and T. Siegrist, "Growth and structural analysis of metalorganic chemical vapor deposited (112-0) Mg_xZn_{1-x}O (0 < x < 0.33) films on (011-2) R-plane Al₂O₃ substrates," *Appl. Phys. Lett.*, vol.82, pp.742, 2003.
- [98] C. S. Rout, S. H. Krishna, S. R. C. Vivekchand, A. Govindaraj, and C. N. R. Rao, "Hydrogen and ethanol sensors based on ZnO nanorods, nanowires and nanotubes," *Chemical Physics Letters*, vol.418, pp.586, 2006.
- [99] A. Z. Sadek, W. Wlodarski, K. Kalantar-zadeh, D. A. Powell, W. L. Hughes, B. A. Buchine, and Z. L. Wang, "H₂ and NO₂ Gas Sensors with ZnO Nanobelt Layer on 36° LiTaO₃ and 64° LiNbO₃ SAW Transducers," *Sensors*, 2005 IEEE pp.1343, 2005.

- [100] M.-C. Jeong, B.-Y. Oh, O.-H. Nam, T. Kim, and J.-M. Myoung, "Three-dimensional ZnO hybrid nanostructures for oxygen sensing application," *Nanotechnology*, vol.17, pp.526, 2006.
- [101] H. Tang, M. Yan, H. Zhang, S. Li, X. Ma, M. Wang, D. Yang, and v. : Chemical, issue 2, pp. 910, 2006, "A selective NH₃ gas sensor based on Fe₂O₃-ZnO nanocomposites at room temperature " *Sensors and Actuators B*, vol.114, pp.910, 2006.
- [102] B. S. Kang, Y. W. Heo, L. C. Tien, D. P. Norton, F. Ren, B. P. Gila, and S. J. Pearton, "Hydrogen and ozone gas sensing using multiple ZnO nanorods," *Appl. Phys. A: Materials Science & Processing*, vol.80, pp.1029, 2005.
- [103] X. Wang, J. Zhang, and Z. Zhu, "Ammonia sensing characteristics of ZnO nanowires studied by quartz crystal microbalance," *Applied Surface Science*, vol.252, pp.2404, 2006.
- [104] Y. Zhang, K. Yu, S. Quyang, L. Luo, H. Hu, Q. Zhang, and Z. Zhu, "Detection of humidity based on quartz crystal microbalance coated with ZnO nanostructure films," *Physica B*, vol.368, pp.94, 2005.
- [105] Z. Zhang, N. W. Emanetoglu, G. Saraf, Y. Chen, P. Wu, J. Zhong, Y. Lu, J. Chen, O. Mirochnitchenko, and M. Inouye, "DNA Immobilization and SAW Response in ZnO Nanotips Grown on LiNbO₃ Substrates," *IEEE Transaction on Ultrasonics, Ferroelectronics and Frequency Control*, vol.53, pp.768, 2006.
- [106] N. W. Emanetoglu, G. Patounakis, S. Liang, C. Gorla, R. H. Wittstruck, and Y. Lu, "Analysis of SAW properties of epitaxial ZnO films grown on R-Al₂O₃ substrates," vol.48, pp.1389, 2001.
- [107] H. Ieki, H. Tanaka, J. Koike, and T. Nishikawa, "Microwave low insertion loss SAW filter by using ZnO/sapphire substrate with Ni dopant," *IEEE MTT-S Dig.*, pp.409, 1996.
- [108] J. S. Lee, H. J. Lee, S. H. Seo, and J. S. Park, "Characterization of undoped and Cu-doped ZnO films for surface acoustic wave applications,," *Thin Solid Films*, vol.398-399, pp.641, 2001.
- [109] D. S. Ballantine, R. M. White, S. J. Martin, A. J. Ricco, E. T. Zellers, G. C. Frye, and Wohltjen, *Acoustic Wave Sensors*. New York: Academic, 1997.
- [110] R. M. Lec and P. A. Lewin, "Acoustic wave biosensors," *Proceedings of the 20th Annual IEEE Engineering in Medicine and Biology Society*, vol.20, pp.2785, 1998.
- [111] J. Homola, S. S. Yee, and G. Gauglitz, "Surface plasmon resonance sensors: review," *Sensors and Actuators B*, vol.54, pp.3, 1999.
- [112] X. C. Zhou, L. Q. Huang, and S. F. Y. Li, "Microgravimetric DNA sensor based on quartz crystal microbalance: comparison of oligonucleotide immobilization methods and the application in genetic diagnosis," *Biosensors & Bioelectronics*, vol.16, pp.85, 2001.
- [113] M. Muratsugu, F. Ohta, Y. Miya, T. Hosokawa, S. Kurosawa, N. Kamo, and H. Ikeda, "Quartz crystal microbalance for the detection of microgram quantities of human serum albumin: relationship between the frequency change and the mass of protein adsorbed," *Analytical Chemistry*, vol.65, pp.2933, 1993.
- [114] G. Z. Sauerbrey, *Phys. Verhandl.* , pp.193, 1957.

- [115] G. Z. Sauerbrey, "The use of oscillators for weighing thin layers and for microweighing.," *Z. Phys.* , vol.155, pp.206, 1959.
- [116] D. A. Buttry and M. D. Ward, "Measurement of interfacial processes at electrode surfaces with electrochemical quartz crystal microbalance," *Chem. Rev.* , vol.92, pp.1355, 1992.
- [117] H. Muramatsu, E. Tamiya, and I. Karube, "Computation of equivalent circuit parameters of quartz crystals in contact with liquids and study of liquid properties," *Anal. Chem.* , vol.60, pp.2142, 1988.

Curriculum Vitae

Zheng Zhang

Education

- | | |
|--------------|---|
| June 2001 | B.S. in Information Science and Electronic Engineering,
Zhejiang University, Hangzhou, Zhejiang, P. R. China |
| May 2004 | Master of Science in Electrical and Computer Engineering
Rutgers University, New Brunswick, New Jersey |
| January 2008 | Doctor of Philosophy in Electrical and Computer Engineering
Rutgers University, New Brunswick, New Jersey |

Publications:

Refereed Journals

1. “Fast and Reversible Wettability Transitions of ZnO Nanostructures”, Z. Zhang, H. Chen, J. Zhong, Y. Lu, *J. Electr. Mater.*, vol. 36, n.8, pp895-899, Aug. 2007.
2. “DNA Immobilization and SAW Response in ZnO Nanotips Grown on LiNbO₃ Substrates”, Z. Zhang, N. W. Emanetoglu, G. Saraf, Y. Chen, P. Wu, J. Zhong and Y. Lu, J. Chen, O. Mirochnitchenko, M. Inouye, *IEEE Trans. on Ultrasonics, ferroelectrics and frequency control*, vol 53, n4, p786-792, Apr. 2006
3. “Binding Studies of Molecular Linkers to ZnO and MgZnO Nanotip Films”, Olena Taratula, Elena Galoppini, Dong Wang, Dorothy Chu, Zheng Zhang, Hanhong Chen, Gaurav Saraf, and Yicheng Lu, *J. Phys. Chem. B*, vol. 110 n. 13, pp. 6506-6515, Apr. 2006
4. “Selective MOCVD Growth of ZnO”, S. Muthukumar, H. Sheng, J. Zhong, Z. Zhang, N. W. Emanetoglu, Y. Lu, *IEEE Trans. Nanotech*, Vol. 2, n. 1, pp. 50-54, 2003.

Patent Award:

“Multifunctional Biosensor Based on ZnO-based Nanostructures”, Y. Lu, Z. Zhang, H. Sheng, N.W. Emanetoglu, M. Inouye, O. Mirochnitchenko, U.S. Patent No. 6,914,279 (July 5, 2005)

Patent Applications:

“Functionalization of ZnO nanotips”, E. Galoppini, Y. Lu, O. Taratula, Z. Zhang (March 29, 2006)

“Sensor Technology Based on Integration of ZnO Nanostructures with QCM and TFBAR Devices”, Y. Lu, Y. Chen, Z. Zhang (Nov 4, 2005)